In-Situ Transmission Electron Microscopy Investigations of Manganese Oxide and Gadolinium Oxide

Author:
Roos M. de Boer

Supervisors:
Dr. Rafael G. Mendes
Dr. ir. Marijn A. van Huis

For the master's degree in
Nanomaterials Science & Experimental Physics

January 31, 2023

Soft Condensed Matter and Biophysics
Debye Institute for Nanomaterials Science

Utrecht University

Abstract

Nanomaterials have been widely studied owing to their interesting properties and potential applications. In this thesis, two novel nanomaterials were studied using *in-situ* transmission electron microscopy (TEM): (1) MnO nanostructures and (2) Gd_2O_3 nanofoam. *In-situ* TEM is used because it enables heating inside the microscope, which allows for real-time viewing of the heating induced changes to the material. The aim of the first part of this thesis was to observe the predicted heating induced square to trigonal lattice transformation in MnO nanosheets. Manganese oxide nanostructures were synthesized using a salt-templating method. Depending on the precursor, this resulted in the formation of either nanoparticles or nanosheets, both of which were heated inside the TEM. The MnO nanoparticles were embedded in amorphous carbon and spontaneously oxidized to Mn_3O_4 under ambient conditions depending on the thickness of the carbon layer. When heated, the nanoparticles reduced back to MnO, indicating a reversible transformation between MnO and Mn_3O_4. The synthesized MnO nanosheets transformed from a square lattice to a trigonal lattice at room temperature as soon as the salt template was removed, thereby confirming the predicted lattice transformation. In addition to manganese oxide nanostructures, gadolinium oxide was synthesized via gel combustion, resulting in highly porous and crystalline nanofoams. The aim of this project was to characterize the porosity and study the formation of the material during combustion synthesis. The material was characterized by physisorption, indicating a large specific surface area of 67 m^2/g, and a 3D model of the structure made using electron tomography visualized the interconnected pore structure of the bulk synthesized Gd_2O_3. The Gd gel was applied to heating chips and heated *in-situ* and *ex-situ* to further analyze the synthesis mechanism. The pore structure was highly dependent on the experimental conditions, indicating that the structure could be tuned by varying the temperature and atmosphere during synthesis. Porous Gd_2O_3 can be used to treat contaminated water and in (photo)catalysis applications, and gel-combustion synthesis is a low-cost and energy-efficient method to synthesize large amounts of this highly porous Gd_2O_3.

Keywords: *In-Situ* TEM, Nanoparticles, Nanosheets, Nanofoams, Metal Oxides

Contents

1. Introduction

Throughout history, the discovery of new materials has often led to revolutions. This becomes obvious from the naming of certain eras in history after the material that was most used at that time, such as the stone-, bronze-, and iron ages. More recent advances in materials science include the discovery of the properties of semiconductors and the start of exploring materials at the nanoscale, which led to the huge technological advancement at the end of the 20th century. It started at the turn of the 20th century, when a group of now well-known scientists began to observe and explain quantum phenomena. In short, these physicists have discovered that materials behave differently from classical physics at sufficiently small scales. It was discovered that small particles, such as electrons, behave as both particles and waves, and their properties are probabilistic rather than deterministic in nature. Nanoscale materials (i.e., with a size in the range of 10^{-9} m in at least one of its dimensions) also exhibit quantum phenomena, which makes these nanomaterials have different properties from their bulk counterparts. For example, while bulk metals have a distinct metallic color, metal nanoparticles exhibit a wide range of colors, depending on their size. Other differences can be found in, for instance, the physiological properties, conductivity, and size of the electronic bandgap. As indicated in the color example of nanomaterials, many of these properties are size-dependent and therefore tunable, meaning that materials can be designed specifically for their properties. This opens up a whole new world of applications, and we are already seeing the benefits. What used to be science fiction is now becoming reality.

1.1. Transition Metal Oxide Nanosheets

One type of nanomaterial is a nanosheet, which is a 2D material with only one of its dimensions at the nanoscale. The most known nanosheet is probably graphene, which was first isolated from its bulk counterpart (graphite) in 2004 by Novoselov and Geim [1], for which they received the Nobel Prize in physics in 2010. The discovery of graphene has led to the search for more nanosheets, and since then, many more nanosheets and 2D materials have been discovered.[2–4] In general, nanosheets are subdivided into two categories, depending on their thickness. There are monolayers, which are nanosheets consisting of only one layer, and thin films, which are nanosheets consisting of multiple layers.

A specific type of nanosheet that will be the focus of this thesis is the transition metal oxide (TMO) nanosheet. Transition metals are of interest due to their unique electronic configurations. Because transition metals have electrons in the d-orbitals, which can have many possible arrangements, TMOs can have multiple possible phases depending on the oxidation state of the metal. A well-known example is titanium oxide, which can be generally found as TiO, Ti_2O_3, and TiO_2. Multiple stoichiometries can exist within these phases. For instance, bulk TiO_2 can be found in rutile, anatase, and brookite phases.[5] TMO nanosheets also have different stoichiometries and can be transformed from one to the other by heating. This was investigated using density functional theory (DFT) and ab initio molecular dynamics (AIMD) for five early transition metals by van Gog *et al.*[6] It was predicted that nine phases may be realized as free-standing nanosheets, namely: *sq*-TiO, *sq*-VO, *sq*-MnO, *h*-Sc_2O_3, *h*-V_2O_3, *h*-Mn_2O_3, *t*-VO, *t*-CrO, and *t*-MnO, where *sq* stands for square, *h* for hexagonal and *t* for trigonal. Moreover, van Gog *et al.* found that heating the *sq*-MnO nanosheets from 300 to 700 K resulted in a transformation to the trigonal configuration.

MnO is particularly interesting among the aforementioned materials. According to the DFT calculations by van Gog *et al.*[6], MnO is the only nanosheet for which the hexagonal and trigonal phases are lower in energy than the square phase. Moreover, MnO has already been predicted to be stable as a free-standing hexagonal nanosheet when sufficiently thin[7] which has recently been experimentally verified.[8] In combination with its magnetic configuration, this graphene-like structured MnO could have interesting spin states. It is predicted that very likely either an anomalous spin Hall effect (ASHE) or a quantum anomalous spin Hall effect (QASHE) exists in graphene-like MnO monolayers.[9] It is even

suggested that there might be exotic spin states such as a spin liquid in monolayer MnO.[7] When experimentally verified, MnO nanosheets could have important applications in spintronics. In general, the hexagonal configuration of atoms in nanosheets results in interesting quantum phenomena. The hopping of electrons in a hexagonal lattice can often be described by a dispersion identical to that of a massless particle described by the Dirac equation, meaning that this lattice is a good candidate for high-energy physics and superconductivity research.[10] Therefore, materials with hexagonal lattices are especially sought, and it would be spectacular to find a whole class of TMOs that can exist in this form. In addition to the interesting fundamental physics that might be explored in MnO, it has been established that MnO can be used as an efficient anode material for lithium-ion batteries.[11–14] Science is only at the beginning of discovering the possibilities of nanosheets, and surely many other potential applications are yet to be found.

Generally, the synthesis of 2D materials is challenging. Approaches are either top-down, where nanosheets are exfoliated from bulk materials with a layered structure, or bottom-up, where nanosheets are grown on a substrate. To synthesize a specific 2D material, it is required that either the bulk counterpart of the material has a layered structure or that there exists a suitable substrate or directing agent onto which the material can grow. Since MnO is a non-layered material, the bottom-up strategy has to be used. Xiao *et al.*[15] successfully synthesized *sq*-MnO nanosheets using a salt template. In short, the KCl lattice can be used as a template for the growth of MnO because there is only a 0.11% lattice mismatch between the KCl (001) and the rotated MnO (001) planes. By using a very small ratio of Mn-precursor:salt, the synthesis can be directed towards growing only thin films of MnO on the salt lattice. Washing away the salt then results in freestanding nanosheets. Using this method, various TMO nanosheets, including *sq*-MnO, can be experimentally realized and further investigated. Moreover, Zhang *et al.*[8] managed to obtain several types of hexagonal nanosheets, including *h*-MnO, by the controlled oxidation of metals. The oxidized layers at the surface are weakly bound through van der Waals forces and can therefore be easily transferred by stamping the oxidized surface on a substrate.

1.2. Lanthanide Oxide Nanocrystals

Other types of nanomaterials are nanocrystals and nanoparticles, which are materials that are at the nanoscale in all three dimensions. The main added value of nanomaterials in the majority of their applications is their large specific surface area. This is beneficial for catalytic processes, adsorption of pollutants during water purification, as well as other fields of implementation. Therefore, increasing the specific surface area is an obvious pathway for increasing the efficiency of the materials used in these processes and technologies. Thus, less material is required, making particular technologies more cost-effective and sustainable. An effective way of increasing the surface area of a material is to make its structure porous. Some materials naturally contain such pores, such as zeolites. More often, these pores are introduced by some form of templating. A unique method that can be used to fabricate porous materials without the use of a template is combustion synthesis.[16] In gel combustion synthesis, a gel consisting of a metal compound, often a metal nitrate, and a fuel, often glycine or urea, is formed. This gel is heated and will ignite at relatively low temperatures. A highly exothermic reaction takes place, causing the temperature of the material to increase considerably. Since a lot of gases are created and released during the reaction, the resulting metal oxide material can be classified as a nanofoam. [16, 17]

Gadolinium is a chemical element that belongs to the group of lanthanides that have partially filled 4f shells, giving them characteristic electronic and luminescence properties. Gadolinium is unique in its magnetic properties; it has a very large spin magnetic moment and can be magnetized at room temperature. For this reason, gadolinium works very well as a contrast agent for magnetic resonance imaging (MRI) [18]. It is also known to have a large thermal neutron capture cross-section, which has been exploited in various applications [19, 20]. The most stable oxidized form of gadolinium is gadolinium(III) oxide (Gd_2O_3). At room temperature, Gd_2O_3 has a cubic crystal structure with space group $la\bar{3}$. Above

1200 °C, the monoclinic structure (space group C2/m) is the most stable, and a hexagonal phase (space group $P\bar{4}m2$) exists at temperatures above 2100 °C [21]. Nanoscale Gd_2O_3 can be applied in, among others, sensing applications [22, 23], in catalysis for the improvement of sulfur cathode materials for lithium-ion batteries [24, 25], and in the treatment of contaminated water [26–28]. Various methods are available for fabricating nanoscale Gd_2O_3, including solid-state [29], sol-gel [30, 31], hydrothermal [32, 33], and gel combustion syntheses [29, 34]. The focus of this work is on the gel-combustion synthesis of Gd_2O_3.

For the gel-combustion synthesis of Gd_2O_3, gadolinium nitrate hexahydrate ($Gd(NO_3)_3{\cdot}6H_2O$) can be used as the metal precursor and glycine (NH_2CH_2COOH) as the fuel. This results in a porous crystalline Gd_2O_3 structure [34] which can be achieved without the use of a template, thereby simplifying the production of Gd_2O_3 for various applications such as water treatment and catalysis, which require large-surface-area materials. Moreover, gel combustion synthesis requires lower temperatures than direct calcination methods, making it a more energy-efficient synthesis route. Therefore, investigation of the combustion synthesis of porous gadolinium oxide is of great scientific and industrial interest.

In this thesis, the investigation of the gel-combustion synthesis of Gd_2O_3 nanofoams in two main steps is described. First, the product from the large-scale combustion synthesis was characterized by physisorption and electron tomography to determine the size distribution and nature of the pores. Physisorption is the scientific standard for measuring the surface area of porous materials. Using electron tomography, a 3D model of the material was reconstructed, allowing inspection of the inner pore structure. Second, *in-situ* heating TEM experiments were conducted on the gel. With the *in-situ* setup, the sample can be heated inside the microscope, allowing for real-time imaging during the synthesis. We provide a high-resolution 3D characterization of the morphological aspects of Gd_2O_3 nanofoam synthesized via combustion synthesis, while the *in-situ* TEM investigations show further possibilities of this method to tune the porosity.

1.3. Aims and outline

As is apparent from the previous sections, this thesis consists of two projects. The first project focuses on a transition metal oxide nanosheet, and it aims at observing the structural transformations during the heating of MnO nanosheets, as hypothesized by van Gog *et al.*[6] The nanosheets will first need to be synthesized, for which the method by Xiao *et al.*[15] will be employed. The second project focuses on a porous lanthanide nanocrystal. The aim is to characterize the pore structure of this gadolinium oxide nanofoam, and to study its formation during the combustion process using *in-situ* TEM.

The outline of this thesis is as follows. First, the relevant theory is described in Section 2, which includes the experimental techniques and underlying physical principles. The methods and results for the manganese oxides are discussed in Section 3, and the methods and results for the gadolinium oxides in Section 4. Finally, a summary and an outlook are provided in Section 5.

2. General Theory

In this section, the general theory relevant to the thesis is described, which mainly includes the measurement techniques used. The theory relevant to the individual methods and experiments is presented in later chapters.

2.1. Transmission Electron Microscopy

Electron microscopy (EM) is one of the most commonly used techniques for imaging materials at the nanoscale. An electron microscope is similar to an optical microscope except that, as the name implies, electrons are used for imaging. Because electrons have a mass, their wavelength is much smaller than that of photons, meaning that a higher resolution can be achieved. Whereas state-of-the-art optical microscopes can reach resolutions of tens of nanometers,[35] which is already a major accomplishment, a good electron microscope can have Ångström (10^{-10} m) resolution. This enables electron microscopes to image individual atoms, which makes it a very suitable method for characterizing nanomaterials. Transmission electron microscopy (TEM) is a specific type of electron microscopy in which electrons are transmitted through the sample to create an image. The first TEM was developed by Max Knoll and Ernst Ruska in 1931.[36] Its development was of such significance that in less than a decade (in 1939) the first commercial TEM was released on the market. Almost a century later, TEMs are still indispensable tools in both materials and biological sciences. In this section, the principles of TEM are explained. Unless mentioned otherwise, the information in this section is derived from two electron microscopy textbooks[37, 38] and the reader is referred to these textbooks for a more detailed discussion of the subject.

2.1.1. Underlying Principles

Since the discovery of quantum mechanics, we know that fundamental particles also behave as waves. The wavelength (λ) of a particle is dependent on its momentum p and Planck's constant h in the following way:

$$\lambda = \frac{h}{p}. \tag{2.1}$$

Electrons in the TEM are accelerated by a potential difference and thus this equation is usually given in terms of the accelerating voltage E. The relativistic wavelength of the electron can be expressed as:

$$\lambda = \frac{h}{\sqrt{2m_0 E e}\sqrt{1 + \frac{eE}{2m_0 c^2}}}, \tag{2.2}$$

where m_0 is the rest mass of the electron, e the electron charge, and c the speed of light. An accelerating voltage of 200 kV results in an electron wavelength of 2.51 pm. However, the wavelength of the electron does not immediately tell you the resolution that can be achieved. As in an optical microscope, the resolution is determined by the Rayleigh criterion, also called the diffraction limit. The Rayleigh criterion states that the smallest distance that can be resolved is given by:

$$d = \frac{0.61\lambda}{n \sin\theta}, \tag{2.3}$$

where λ is the electron wavelength, n is the refractive index of the imaging medium (mostly vacuum), and θ is the semi-angle of the lens, which depends on its diameter and focal length. For microscopes operating under an accelerating voltage of 200 kV, the maximum resolution that can be obtained is 1.0 Å, assuming the imaging medium is vacuum (n=1) and the semi-angle is 15 mrad. However, the diffraction limit gives the maximum theoretical resolution. Due to practical limitations, the actual resolution of a TEM is usually a little lower.

Another important principle that is used in TEM is Bragg scattering. Electrons are scattered when interacting with the sample, and these scattered electrons contain information about the crystal structure of the sample, such as the distance between atomic planes in the material.

According to Bragg's law, the interference between electron waves can be expressed by:

$$2d \sin\theta = \lambda, \tag{2.4}$$

where d is the spacing between atomic-planes, θ the angle of the incoming wave, and λ the wavelength of the electron. This relation can easily be verified geometrically by looking at figure 2.1.

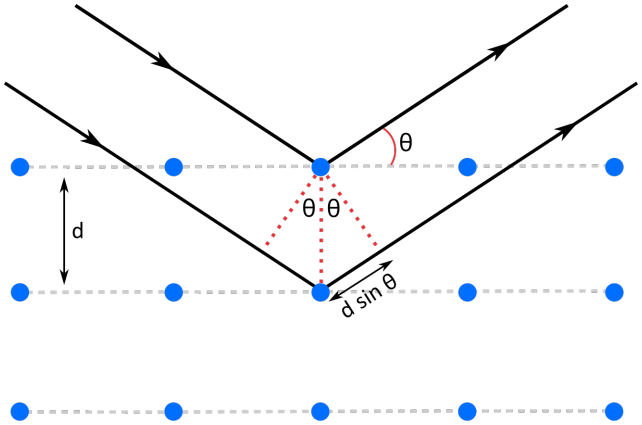

Figure 2.1: Diagram showing Bragg scattering of a lattice with atomic-plane spacing d.

A conventional way to describe atomic planes is by using Miller indices h, k, and l. The distance between planes in a cubic lattice labeled by (hkl), for instance, can be described by:

$$d_{hkl} = \frac{a}{\sqrt{h^2 + k^2 + l^2}}, \tag{2.5}$$

where a is the lattice parameter of the material. Note that Miller indices can also be used to indicate directions or lattice vectors, which are labeled with [hkl] [1].

In X-ray scattering experiments, one usually varies θ to obtain the electron intensity as a function of θ. For a perfectly crystalline material, distinct peaks are observed at certain values of θ. Using Bragg's law, the distance between different atomic planes can then be determined. Because the interatomic spacing is material- and morphology-dependent, these diffraction experiments are often used for material characterization. It is also possible to create diffraction patterns using TEM. When the sample is crystalline, spots or rings of high intensity can be observed, from which the lattice spacing can be determined. By comparing the intensity and determined lattice spacing with those of X-ray spectra, the correct material and morphology can be identified from TEM diffraction. Another way to identify materials is to take the fast Fourier transform (FFT) of a high-resolution image. The Fourier transform is a function that transforms the image to the frequency domain. Any periodicities present in the image, such as a periodic lattice, are represented by discrete points in the frequency domain. The resulting image shows the reciprocal lattice of the material, which is similar to the diffraction pattern. The distance between the points in the FFT, which is measured in reciprocal length (usually nm^{-1}), reflects the lattice parameters of the material. The points and rings in the diffraction patterns and FFTs each represent a plane, and are therefore usually indexed with the Miller notation mentioned above.

[1] There are more Miller notations representing different information: (h,k,l) represents a point, $\langle hkl \rangle$ represents a family of directions, and $\{hkl\}$ represents a family of planes.

2.1.2. Working Principle

A photograph of the interior of a high-end TEM and a schematic overview of the basic components are shown in figure 2.2. In older TEMs, the column could be seen from the outside. Nowadays it is typically hidden in a box. A modern TEM contains many more components than those shown in the schematic, such as stigmators, deflector coils, and multiple condensor, intermediate, and projector lens systems.

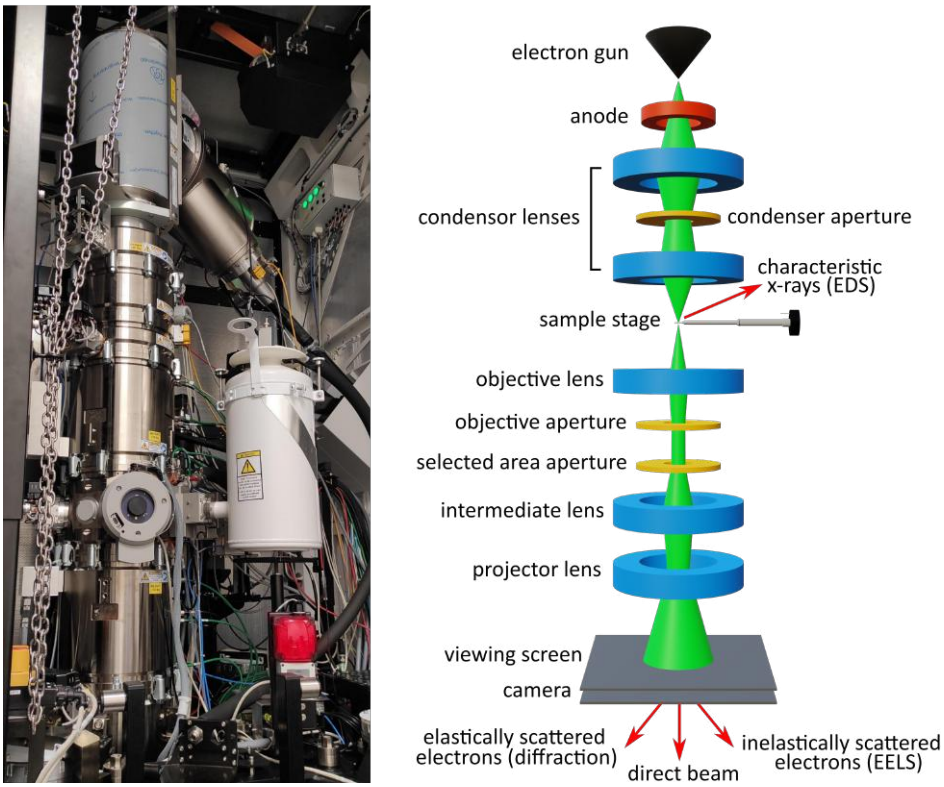

Figure 2.2: Photograph of the TEM column inside the high-end double-aberration corrected TFS Spectra 300 microscope (left) and a schematic of the components inside a basic TEM column (right).

Imaging using TEM is only possible by the generation and acceleration of electrons, which occurs in the upper part of the microscope using an electron gun. There are several types of electron guns, which can be divided into two classes: thermionic guns and field-emission guns. To emit electrons from a material, the work function of the material should be overcome. In a thermionic electron gun, heat is applied to a metal filament to overcome the work function and cause the emission of electrons. The current density that can be reached is described by Richardson's law:

$$J = AT^2 \exp(-\Phi/kT), \tag{2.6}$$

where A is Richardson's constant, T is the temperature of the material, Φ is the work function, and k is Boltzmann's constant. In the first generation of TEMs, a tungsten wire is often used, which needs to be heated to temperatures where the tungsten itself slowly evaporates, leading to a short lifetime. Another disadvantage of using high temperatures is that this causes the electrons to have a spread in energies, causing chromatic aberrations in the TEM. Later, LaB_6 was used for the filament because it has a lower work function and thus allows for the use of lower temperatures. This causes the lifetime of a LaB_6 filament to be approximately ten times longer than that of a tungsten filament and also results in a higher energy coherence.

Another type of electron gun, the field emission gun (FEG), uses a potential gradient instead of temperature to overcome the work function of the material. By applying a potential to a sharp tungsten

tip, electrons can overcome the work function and tunnel out of the tungsten. Because the electron beam generated by an FEG is more coherent (resulting in less chromatic aberration) and has a longer lifetime owing to the low temperature, the FEG is usually the preferred choice of electron source for most high-end TEMs. When electrons are emitted, they are focused into a beam and accelerated by the positive potential of the anode.

A TEM has several electromagnetic lenses to focus the beam, and apertures to restrict the beam. Electromagnetic lenses are analogous to optical lenses that are used in a light microscope but use magnetic fields to deflect the charged electrons. Apertures are metallic discs with holes through which the beam may pass. Before passing through the sample, the electron beam is focused by the lenses of the condenser system and restricted by the condenser aperture. The sample itself is mounted in the sample holder that is inserted into the TEM. The sample holder is connected to a mechanical arm that allows for the precise translation and rotation of the sample.

After passing the sample, the beam travels through the intermediate and projector lenses before falling onto the viewing screen where the image is recorded. In first-generation TEMs, a fluorescent screen is used for direct real-time viewing, which is retracted when the image is recorded by the camera. Nowadays, digital cameras commonly enable real-time viewing of samples.

To avoid electrons colliding with gas molecules in air, the TEM is always operated under high vacuum ($<10^{-7}$ mbar), which is achieved with multiple pumps. There is a pre-vacuum pump whose purpose is to reduce the pressure from atmospheric pressure to reasonably low pressure, but not yet high vacuum. An additional high-vacuum pump is required to get the vacuum to high vacuum. This pump can be either a diffusion pump, which uses a jet of vapor to lure gas atoms into the pump, or a turbo pump, which uses propellers. Often an ion-getter pump is used as well, which traps gases in a chamber by ionizing and implanting the molecules into a metallic plate.

There are two main imaging modes in TEM: the bright-field (BF) and dark-field (DF) modes, which are determined by the objective aperture. In the BF mode, the direct beam passes through the objective aperture and is transmitted through the sample. Areas with low electron transmittance are dark, and areas with high electron transmittance are bright in the image. In the DF mode, however, the objective aperture is adjusted such that only the diffracted electron beam passes. Areas with high electron diffraction will be bright, and areas with low electron diffraction will be dark in the image. There is also a diffraction mode in which electron diffraction patterns of the sample can be obtained. This is achieved by removing the objective aperture and adjusting the electromagnetic lenses such that the back focal plane falls onto the viewing screen. Often, a beamstop is inserted in diffraction mode to block the high intensity of the direct beam to see the diffraction spots better as well as to avoid overexposing the camera to the direct electron beam. In addition, a selected area aperture can be inserted to perform selected area electron diffraction (SAED), which enables taking a diffraction pattern of only a certain area of the sample.

High-resolution transmission electron microscopy (HRTEM) is also possible, and is also known as lattice fringe or phase-contrast imaging. This technique uses a large objective aperture to select both the direct and diffracted beams. The phase of an electron wave may change when it interacts with a sample. The difference in the phase between the direct and diffracted beams gives rise to interference with the same periodicity as the crystal lattice. As a result, the lattice of a material can be imaged using HRTEM, which makes it useful for structural identification. However, it should be noted that the lattice that is reproduced from the electron beam interference does not necessarily correspond to exact atomic positions in the actual lattice of the material.

2.1.3. Samples

Not all samples can be imaged using a TEM. The main requirement for TEM imaging is that the sample must be thin (<100 nm). Because TEM relies on the transmission of electrons through a sample, it

is required that the sample is transmissive (electron transparent), which can be achieved by using thin samples. When the sample is not sufficiently thin, electrons can interact multiple times with the sample before being detected. Electrons that interact multiple times no longer contain the correct information anymore. This can for instance be seen in the diffraction pattern, where diffuse rings are present when a (crystalline) sample is too thick. Another requirement is that the sample should be stable under electron irradiation. This limits the possibilities for organic samples. One solution for this is the use of cryo-EM, where the sample is flash-frozen before imaging. Materials that are most suited for TEM imaging are "hard" materials such as metals, semiconductors, and ceramics.

Another challenge in TEM is the necessity of specific sample preparation methods to apply the sample on a TEM grid prior to the imaging session. If the sample is a dispersion of particles in a liquid, it will be dried when applied to the TEM grid. This could cause drying effects such as particle aggregation. Images taken from such a sample cannot be directly compared to the wet sample. Observing aggregation on the TEM grid does not mean that the particles are also aggregated in their dispersion. The particles that are imaged are also a small fraction of the particles that are present in the bulk and might not be fully representative. Therefore, it is important to image different parts of the sample and collect statistically relevant data as well as to compare TEM observations with other techniques.

Finally, the sample should be conductive due to the use of electrons. If the sample is not conducting electrons, they accumulate in the sample (charging), resulting in poor quality images.

2.1.4. Electron beam - Sample Interactions

Under ideal circumstances, the electrons in the electron microscope would not affect the material under investigation. However, in practice, the circumstances are never ideal, and some effects should be considered.

The fundamental working principle of an electron microscope is that the accelerated electrons (primary electron beam) interact with the specimen and are scattered. Most electrons scatter elastically, meaning that their energies are conserved. However, electrons can also scatter inelastically, where some of their energy is lost to the sample. This energy can be converted into thermal energy, which causes the sample to heat under electron beam irradiation. The energy resulting from inelastic scattering can also ionize the material and cause the breaking of chemical bonds, thereby changing or destroying the sample.

Another electron beam effect is the displacement of atoms. When a high-energy electron hits an atom in the sample, there is a chance that it is knocked out of the lattice by a large momentum transfer, creating a defect. This type of damage is called knock-on damage, and often occurs in metals.

Finally, the conditions under which an electron microscope operates can also influence the nature of the sample being investigated. Electron microscopes operate under high vacuum to prevent electrons from interacting with anything other than the sample. For normal imaging of samples, this is not much of a problem. However, when performing *in-situ* TEM, such as heating, the changes in the sample are much more influenced by the vacuum. For instance, vacuum is a reducing medium, whereas air is not. Therefore, when the reduction of a sample is observed when heating *in-situ*, it is very well possible that this reduction does not occur at the same temperature in air. Moreover, there is a magnetic field inside the electron microscope caused by the use of charged particles and electromagnetic lenses, as shown in Fig. 2.3. The objective lens alone induces a magnetic field up to 2-3 T under normal conditions [39]. In some cases, this can favor certain lattice configurations, and should therefore be considered, especially when working with magnetic materials.

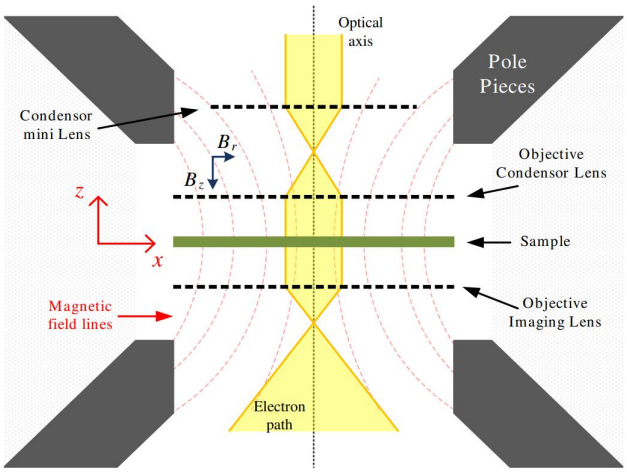

Figure 2.3: Magnetic field induced by the objective lens in a conventional TEM. Obtained from ref. [39].

2.1.5. Additional Techniques

In addition to the regular TEM described above, some modifications and additions can be made to make it even more powerful.

One of the modifications that can be made to a TEM is to incorporate the principle of a scanning electron microscope (SEM) to create a scanning transmission electron microscope (STEM). In STEM mode, the electron beam probes the sample in raster mode. The information of each point in the raster is then combined to form the final image. Because the sample is scanned pixel-by-pixel, the image takes a longer time to build up than in regular TEM mode. A particularly useful attribute of STEM imaging is its ability to perform high-angle annular dark-field (HAADF) imaging. This technique uses high-angle incoherent scattered electrons to form an image for which the contrast is determined by the atomic number. This technique is therefore also sometimes referred to as Z-contrast imaging (conventional TEM imaging uses phase contrast). Depending on the size of the electron probe, the resolution of HAADF images can be as high as that of HRTEM images. However, unlike HRTEM, the atomic positions can be directly identified owing to the use of incoherent electrons. A disadvantage of STEM is that the sample is more sensitive to contamination and more prone to damage due to the use of a condensed electron beam and the relatively long scanning time.

There are also some spectroscopic techniques that can be incorporated into TEM devices. Techniques that are often incorporated include energy-dispersive X-ray spectroscopy (EDS) and electron energy-loss spectroscopy (EELS). Using EDS, the concentrations of different elements in the sample can be determined by analyzing the X-rays emitted when the electron beam is focused on the sample. This is called EDS quantification. In combination with STEM, it is also possible to do EDS mapping, which gives an indication of where the elements are located in the sample. However, it should be noted that EDS analysis is not very precise and should be regarded as an estimation of the elemental composition of a sample. Using EELS, the energy loss of electrons passing through the samples is measured, from which the core electron and phonon excitations in the sample can be determined. From this, a wide array of atomic and chemical properties can be derived. It is also possible to map the thickness of a material using EELS. Since the intensity of inelastically scattered electrons is statistically related to the thickness of the material, the thickness can be easily estimated by comparing the total intensity to the zero-loss intensity, where the zero-loss intensity is the intensity of electrons that were not scattered inelastically. EDS is generally easier to use than EELS, and is most often used to determine the atomic composition and concentration of elements in a sample. With EELS, also electronic properties can be determined at a high resolution. However, EELS becomes more difficult for heavier elements where the excitation edges

are less well defined.

2.1.6. In-Situ Heating

A very powerful technique that can be applied in TEM is the possibility of changing the environment of the sample while it is in the TEM, which is called *in-situ* TEM. Some examples of *in-situ* TEM include the introduction of gaseous or liquid environments, adding mechanical strain, electrical biasing, illumination, and heating.[40] These external stimuli are applied through specialized sample holders that are often supplied by specialized companies. In this thesis, *in-situ* heating was performed. The sample holder and heating chips that are used for this project were from DENSsolutions.

The tip of the heating holder and the heating chip are shown in Fig. 2.4. The heating chip has four electrodes that are connected to the holder when inserted, which is in turn connected to the heating control unit. The temperature can be controlled with the python-based Impulse program from DENSsolutions, which also records the measured temperature over time. The heating chip uses 4-point probe heating, which can reach temperatures up to 1300 °C and provides a temperature homogeneity of 99.5% [41].

The heating chip has circular and rod-shaped viewing windows that are covered by an amorphous silicon nitride (SiN_x) film on which the sample rests, see Fig. 2.4. Because the SiN_x film provides a background signal, it can in some cases be difficult to obtain sharp high-resolution TEM images. When imaging materials with a low atomic number, the film can even entirely eliminate the ability to do high-resolution imaging. Therefore, holes were made in the SiN_x windows of the heating chips used in this thesis using a focused ion beam (FIB), resulting in heating chips that could effectively support the samples but allow for imaging without background.

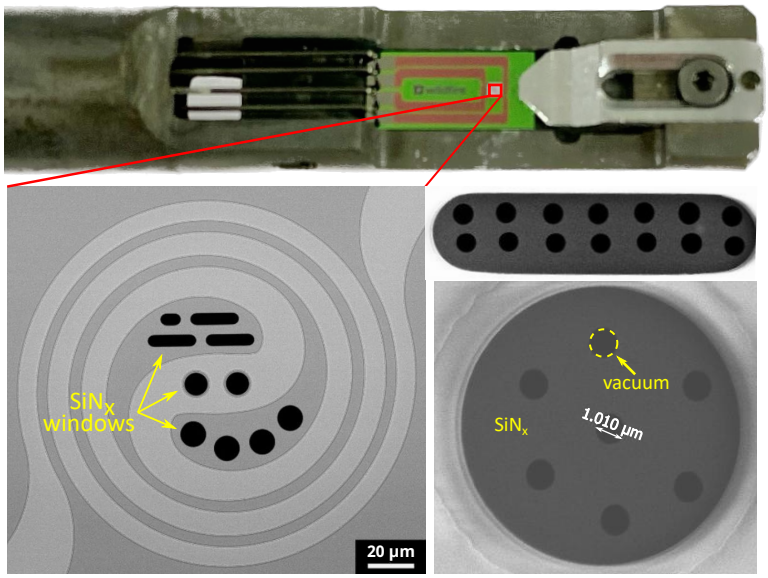

Figure 2.4: DENSsolutions 'Wildfire' heating holder with heating chip. SEM images show the magnified chip with viewing windows covered by SiN_x with (right) or without (left) holes. Parts of this figure were obtained from ref. [42].

2.1.7. Electron Tomography

The images that can be obtained with TEM are 2D projections of a 3D material. It is not possible to fully interpret the 3D structure from a single TEM image. For instance, from a single image, it is not possible to determine whether a pore is located at the center of the material or at the surface, and a pore might appear spherical but could actually be cylindrical. However, by tilting the sample, images can be obtained from different angles. By observing the sample from different angles, it is possible to

derive fundamental morphological features of the sample. For example, it is possible to deduce whether a particle is cubic or plate-like. Furthermore, it is also possible to obtain a full 3D model of a material using tomography. Tomography is a method in which computer algorithms are used to obtain a 3D reconstruction from a 2D tilt series recorded with TEM.

The two main reconstruction algorithms are weighted back projection (WBP)[43] and the simultaneous iterative reconstruction technique (SIRT)[44]. The basis for both algorithms is back projection, in which the tilt series of the sample is "back projected" in the orientation in which it was measured. This is usually done with the help of the Fourier transform. The 3D reconstruction is obtained by taking the inverse Fourier transform of the combined Fourier transforms of the single images at their respective angles. However, this Fourier method overestimates the low frequencies, which leads to a blurry reconstruction. This can be overcome by introducing a weighting function, which forms the basis of the WBP method. The weighting function reduces the low-frequency contributions, thereby creating a more realistic 3D reconstruction. Using the SIRT method, a simple back-projection of the data is first created. New simulated 2D projections at different angles are then derived from this back-projection. The new 2D projections are compared with the original dataset and corrected accordingly. The corrected projections are then back projected again, from which slightly improved projections are derived. This process is repeated until the projections from the back projection are in good agreement with the original tilt series. Both methods have their advantages and disadvantages. WBP is generally fast but can result in a less accurate 3D reconstruction. SIRT is computationally heavy and takes much longer than WBP but generally provides a better 3D reconstruction. However, SIRT also results in a different intensity profile compared to WBP, which sometimes causes problems with segmentation.

Theoretically, highly accurate 3D models can be obtained by electron tomography. It is the number of images and the quality of the acquired tilt-series that limits the 3D reconstruction. Because of the sample holder, it is not possible to obtain images at every tilt angle. The tilt range is typically limited to approximately $\pm 70°$. This implies that information from a certain tilt range is missing, which is called the missing wedge effect. Another limitation is the alignment of the images. It is essential to ensure that only the tilt angle causes a difference in the two images. Any movement of the sample during acquisition must be corrected before starting the reconstruction. To improve the alignment, the TEM grid can be decorated with fiducial markers, which act as reference points during the alignment. Gold nanoparticles are often used for this purpose, which give distinct high-contrast spots in the images that can be tracked by the software and precisely aligned throughout the tilt series.

2.2. Physisorption

Physisorption is an important technique often used to characterize porous materials. Physisorption relies on the adsorption of molecules (adsorbate) by the material of interest (adsorbent). In contrast to chemisorption, in which probing molecules are bonded to the material of interest, physisorption relies on non-bonding interactions between the adsorbate and adsorbent. During physisorption measurements, a gas of adsorbate is slowly added to the adsorbent, causing the adsorption of adsorbate molecules on the surface of the adsorbent. The amount of gas adsorbed by the material can be determined by measuring the amount of gas removed from the gas phase. The adsorption of molecules is not linear with the amount of gas that is added. By investigating the amount of gas adsorbed as a function of the amount of gas added, much can be discovered about the sample. Such curves are called physisorption isotherms [1] and are the main results of the physisorption measurements. In contrast to adsorption, desorption isotherms can be measured by removing the gas, leading to desorption of the adsorbate from the adsorbent. The

[1] The term isotherm is used because the curves are measured at constant temperature (77 K in the case of nitrogen physisorption).

desorption of gas can occur differently from adsorption depending on the structure of the adsorbent. When the adsorption and desorption curves do not overlap, hysteresis occurs, from which information regarding the porous structure of the material can be derived. The guidelines and definitions of physisorption have been reported by the IUPAC and are now accepted by the scientific community as the standard. According to IUPAC, there are three pore classes:

1. micropores are pores that are not more than 2 nm in size,
2. mesopores are pores that are between 2 and 50 nm in size,
3. macropores are pores that exceed 50 nm in size.

There is also the more general term nanopore, which is used to describe pores that are no larger than 100 nm in size. The IUPAC also has standardized types for hysteresis loops which are characteristic for different pore shapes. [45]

However, physisorption isotherms alone do not provide all the desired information about a sample. Other methods are required to obtain the surface area, pore volume, and pore size distribution of the material. To obtain the surface area of the adsorbent, the Brunauer-Emmett-Teller (BET) method [46] is most often used. The basic theory of molecular adsorption is given by the Langmuir theory, which assumes monolayer adsorption. BET theory extends the Langmuir model to include multilayer adsorption. This results in the BET equation describing the theoretical adsorption as a function of pressure. This equation can be plotted as a straight line using the experimental data, which is called the BET plot. By fitting this line, the slope and intersection with the y axis can be determined, from which the surface area of the material can be calculated. The pore volume is most often determined using the t-plot proposed by de Boer *et al.* [47], in which the volume of the adsorbate is plotted against the statistical layer thickness t of a nonporous reference material. The micropore volume can be calculated from the intercept of the extrapolated t-plot with the y axis. The pore size distribution of the material is calculated using the Barrett-Joyner-Halenda (BJH) method [48]. This method uses the Kelvin equation to describe the filling of pores, and assumes multilayer adsorption.

3. Manganese Oxides

In this section, the results for the manganese oxides synthesized using the salt-templating method are described. The aim was to observe the predicted heating induced square to trigonal lattice transformation in MnO nanosheets. By varying the precursor, it was possible to synthesize eiher nanoparticles or nanosheets. Using *in-situ* TEM, the transformations in the synthesized manganese oxides upon heating were explored. The figures and results in this section rely heavily on two programs. The VESTA program [49] was used for the visualization of atomic configurations, and CrysTBox [50] was used for the analysis of experimental diffraction patterns and HRTEM images, and for the simulation of theoretical diffraction patterns from certain crystal planes.

3.1. Theory

3.1.1. Manganese Oxides

Owing to the different possible oxidation states of manganese, there is a wide range of manganese oxides. The lowest possible oxidation state of manganese is 2+, which gives the compound MnO. MnO can exist in various phases. The most common phase, which is usually found at ambient conditions, is the cubic phase as shown in Fig. 3.1. The unit cell parameters of this phase are listed in Table 3.1. In this phase, both the anions and cations are octahedrally coordinated. At high temperatures and pressures, MnO can restructure into the orthorhombic phase. It was predicted that there is also the possibility of a hexagonal (wurtzite) MnO phase,[51] which was experimentally realized for the first time by Nam *et al.*[52] A mix of oxidation states 2+ and 3+ results in Mn_3O_4, which is usually found in the tetragonal phase as shown in Fig. 3.1. The lattice parameters of this structure are listen in Table 3.1. Here, the Mn^{2+} ions occupy the tetrahedral sites whereas the Mn^{3+} ions occupy the octahedral sites. When all manganese atoms have an oxidation state of 3+, the resulting oxide is Mn_2O_3. Finally, an oxidation state of 4+ is also possible, resulting in MnO_2. The experimentally determined formation enthalpy of each compound is listed in Table 3.2.[53] These energies suggest that Mn_3O_4 is the most stable manganese oxide, closely followed by MnO and Mn_2O_3.

The MnO monolayer lattices previously investigated using DFT are the square and hexagonal lattices. However, during relaxation of the hexagonal lattice, which has p3m1 symmetry, the lattice relaxed to a distorted hexagonal lattice with reduced p31m symmetry called the trigonal lattice. The configurations of the lattices are shown in Fig. 3.1. The trigonal lattice of MnO is unique in the sense that the lattice parameters a and b are not identical, whereas all other investigated trigonal lattices have $a = b$.[6] The t-MnO lattice also has a lower formation enthalpy than h-MnO and sq-MnO (see Table 3.2), implying that it is theoretically the most thermodynamically favorable configuration. According to Table 3.2, the bulk phases are lower in energy than the monolayer phases. This indicates that the monolayer phases are not stable and would rather restructure into their bulk counterparts. However, the aforementioned bulk phases are experimental, whereas the monolayer phases are computational, meaning that they cannot be compared directly. Moreover, even though the bulk phases might be lower in energy, there could be a high energy barrier associated with the restructuring process. This means that the monolayer phases are metastable and can still exist as freestanding nanosheets.

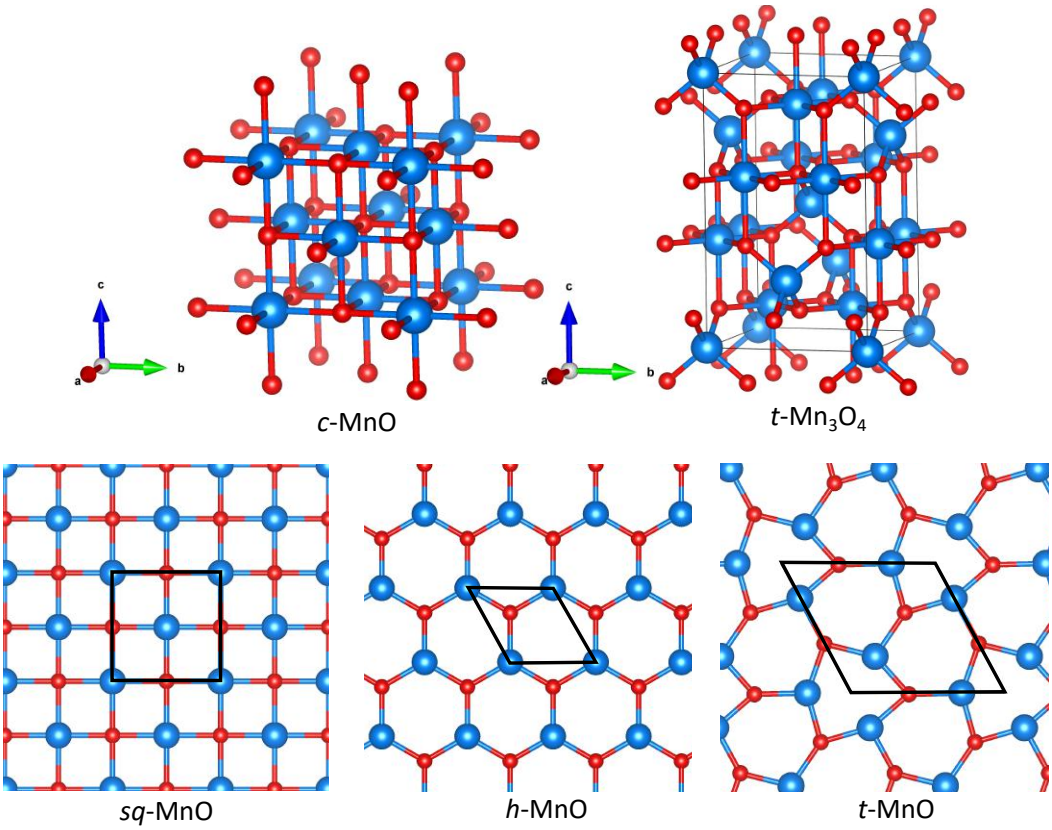

Figure 3.1: Configurations of selected manganese oxides. See Table 3.1 for the unit cell parameters.

Table 3.1: Unit cell parameters for selected bulk [54, 55] and monolayer (ML)[6] manganese oxides.

Material	a (Å)	b (Å)	c (Å)	angle (°)
c-MnO	4.446	4.446	4.446	$\alpha = \beta = \gamma = 90.0$
t-Mn_3O_4	5.762	5.762	9.439	$\alpha = \beta = \gamma = 90.0$
sq-MnO (ML)	4.059	4.059	-	$\theta = 90.0$
h-MnO (ML)	3.282	3.282	-	$\theta = 64.2$
t-MnO (ML)	5.710	5.447	-	$\theta = 118.5$

Table 3.2: Formation enthalpies for the bulk (at 298.15 K)[53] and monolayer (ML) (at 0K) [6] manganese oxides.

Material	Formation enthalpy (eV/atom)
MnO	-1.996
Mn_3O_4	-2.055
Mn_2O_3	-1.988
MnO_2	-1.796
sq-MnO (ML)	-1.098
h-MnO (ML)	-1.137
t-MnO (ML)	-1.208

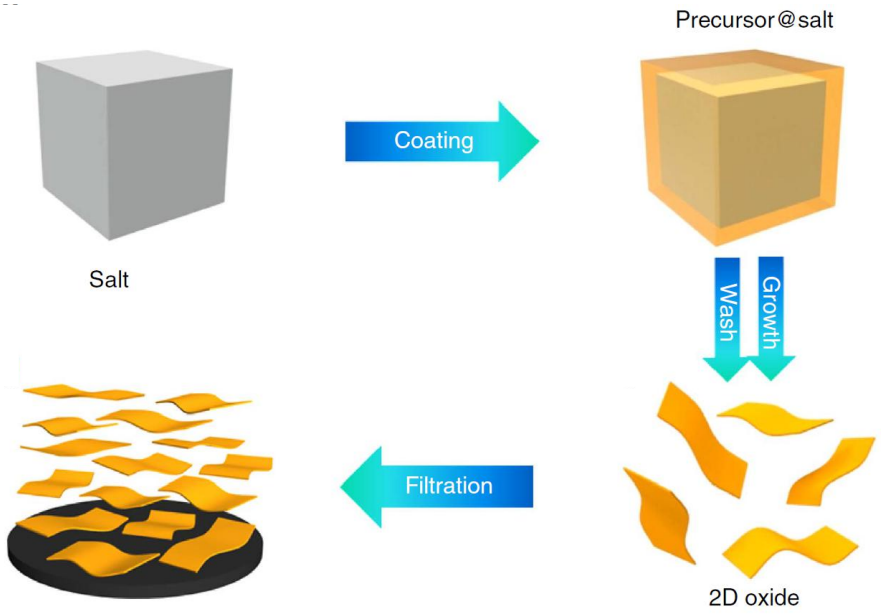

Figure 3.2: Schematic representation of the method used to obtain MnO nanosheets. First, the salt is coated with an Mn precursor, which is then heated followed by dissolving of the salt templates to obtain the nanosheets. Obtained from ref. [15].

3.1.2. Salt-Templated Synthesis

The salt-templating method first described by Xiao *et al.*[15] was used for the synthesis of MnO nanosheets. In this method, a metal precursor is diluted in ethanol and added to a large amount of salt. The salt lattice acts as a template on which MnO can grow. By using an easily dissolvable salt, the salt can be washed away with water, and after filtering, only the MnO nanosheets remain. A schematic of the synthesis process is presented in Fig. 3.2. For this method to yield nanosheets, it is important that the salt lattice matches very closely with the MnO lattice to promote Frank-van der Merwe growth. If there is a large lattice mismatch, the lattice strain causes island growth rather than film growth.[56]

According to the Xiao *et al.*[15], the cubic lattice of MnO has a lattice constant of 0.4442 nm. KCl has a cubic lattice with a lattice constant of 0.3138 nm. However, by rotating the KCl crystal plane by 45°, the lattice constant increases by a factor of $\sqrt{2}$, yielding an effective lattice constant of 0.4437 nm. The difference between the rotated KCl lattice and the MnO lattice is now only 0.11%, which should be small enough to promote Frank-van der Merwe growth.

After mixing the manganese precursor with the salt template, the ethanol is evaporated and the salt mixture is heated to form MnO. According to a previous study on the decomposition of manganese acetate tetrahydrate ($Mn(CH_3COO)_2 \cdot 4H_2O$), dehydration of the Mn-salt occurs first, after which the intermediate acetyl manganese acetate ($Mn(CH_3COO)_2COCH_3$) is formed. Around 150 °C the formation of the second intermediate manganese acetate hydroxide ($Mn(CH_3COO)_2 \cdot OH$) is observed, which is followed by its decomposition resulting in the formation of MnO at about 290 °C under N_2 and H_2 atmospheres.[57]

3.2. MnO Nanoparticle Arrays

3.2.1. Experimental

The manganese oxides reported in this section were synthesized using the method reported by Xiao *et al.*[15] All chemicals were used as received without further treatment unless mentioned otherwise. In a typical synthesis, 50 g of KCl ($\geq$ 99.0%, Sigma-Aldrich no. P3911) was weighed. Then 62.5 mg

manganese(II) acetate tetrahydrate ($Mn(CH_3COO)_2 \cdot 4H_2O$, 99.99%, Sigma-Aldrich no. 229776) was dissolved in 5 mL of absolute ethanol. The solution was magnetically stirred for approximately 5 min at 200 rpm. After the manganese acetate was fully dissolved, it was added to the KCl while stirring. After the salt was completely wetted by the manganese solution, it was heated on a 70 °C hotplate for 20 min to evaporate the ethanol, after which it was completely dry again. The salt was then transferred to a ceramic heating boat and heated in a 400 °C tube oven under either N_2 or Ar atmosphere for 1 h with a ramping rate of 2 °C/min. Photographs of the Mn coated salt before and after heating can be seen in Fig. A.1. After heating, the salt was allowed to cool to room temperature naturally while still inside the oven under inert atmosphere. It was then dissolved in water to yield a brown/orange solution. The solution was then vacuum-filtered and the residue was dispersed in approximately 7 mL of absolute ethanol, see Fig. A.1. In general, the dispersion was directly dropcasted on a lacey TEM grid for imaging.

The TEM imaging was performed using a TFS Talos F200X microscope operating at 200 kV. SEM images were obtained using a Phenom ProX desktop SEM operating at 10 kV. HAADF-STEM imaging was performed in a TFS Spectra 300 operated at 300 kV. The heating experiments were carried out using the DENSsolutions wildfire *in-situ* holder in the TFS Talos F200X TEM. For the heating experiments, the MnO_x dispersion was dropcasted on the DENSsolutions MEMS heating chip, containing a silicon nitride (SiN_x) film in which holes were made using the TFS Helios G3 FIB-SEM.

3.2.2. Synthesis Characterization

Before the heating step in the reported salt-templating synthesis was carried out in a tube oven under inert atmosphere, it was first attempted in a box oven in air. This resulted in Mn_2O_3 nanoplatelets of several hundred nanometers in size. The manganese was further oxidized because of the oxidizing properties of air. To achieve better control over oxidation, the synthesis must be carried out under inert atmospheres, such as N_2 and Ar.

When heated under N_2 atmosphere in a tube oven, the first time aggregated Mn_3O_4 nanoparticles that were tens of nanometers in size were obtained, as shown in Fig. A.3. This could have been caused by the improper sealing of the tube oven. However, it was also suspected that the quality of the KCl templates was insufficient to promote the growth of MnO on its surface. Therefore, the KCl grains were investigated using SEM, as shown in Fig. 3.3a. The SEM images revealed that the KCl crystals did not have smooth surfaces on which MnO could grow, which was probably caused by long-term exposure to a humid environment. Two options were considered, which were recrystallizing the salt and using a new bottle. Recrystallization was carried out by making a saturated solution of KCl in water, after which a large amount of absolute ethanol was added to promote recrystallization. The resulting white powder was vacuum-filtered and dried on a 40 °C hotplate for an hour. Both the recrystallized KCl and KCl from the new bottle were investigated using SEM, as shown in Fig. 3.3b and c. Although both KCl samples presented relatively smooth surfaces, the recrystallized salt had a crystallite size approximately 10 times smaller than the one from the newly purchased bottle. This ultimately means that the surface area per weight of KCl was much higher in the recrystallized KCl. This meant that a larger amount of manganese acetate had to be used to coat the salt, and consequently also a larger amount of ethanol had to be used to dissolve this amount of manganese acetate. Because the KCl salt might also partially dissolve in ethanol when an increased amount is used, the larger crystallites from the new KCl bottle are a better option to use in the synthesis.

Both salts were used in a synthesis. The recrystallized KCl yielded MnO particles that appeared spherical and were tens of nanometers in size, see Fig. 3.4a. The phase was MnO and not a higher oxide, as indicated by the diffraction pattern in Fig. 3.4a'. However, these were nanoparticles and not sheets. The new KCl crystals also yielded similar spherical-looking MnO nanoparticles with sizes in the range of tens of nanometers, as shown in Fig. 3.4b and b'. The thickness of the sample was investigated using EELS, as shown in Fig. 3.5. A particle with a size of 40 nm had a thickness of 19 nm, indicating that

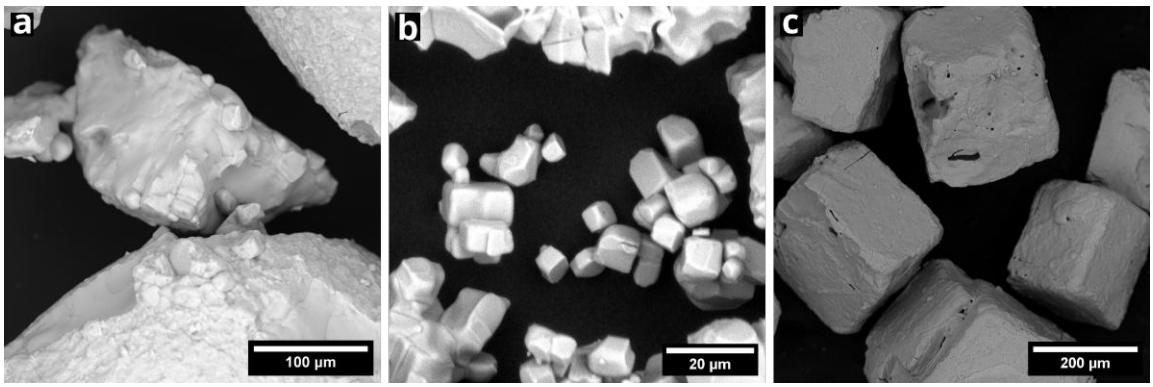

Figure 3.3: SEM images of KCl crystals originating from an old stock (a), recrystallized from old stock (b), and from new stock (c).

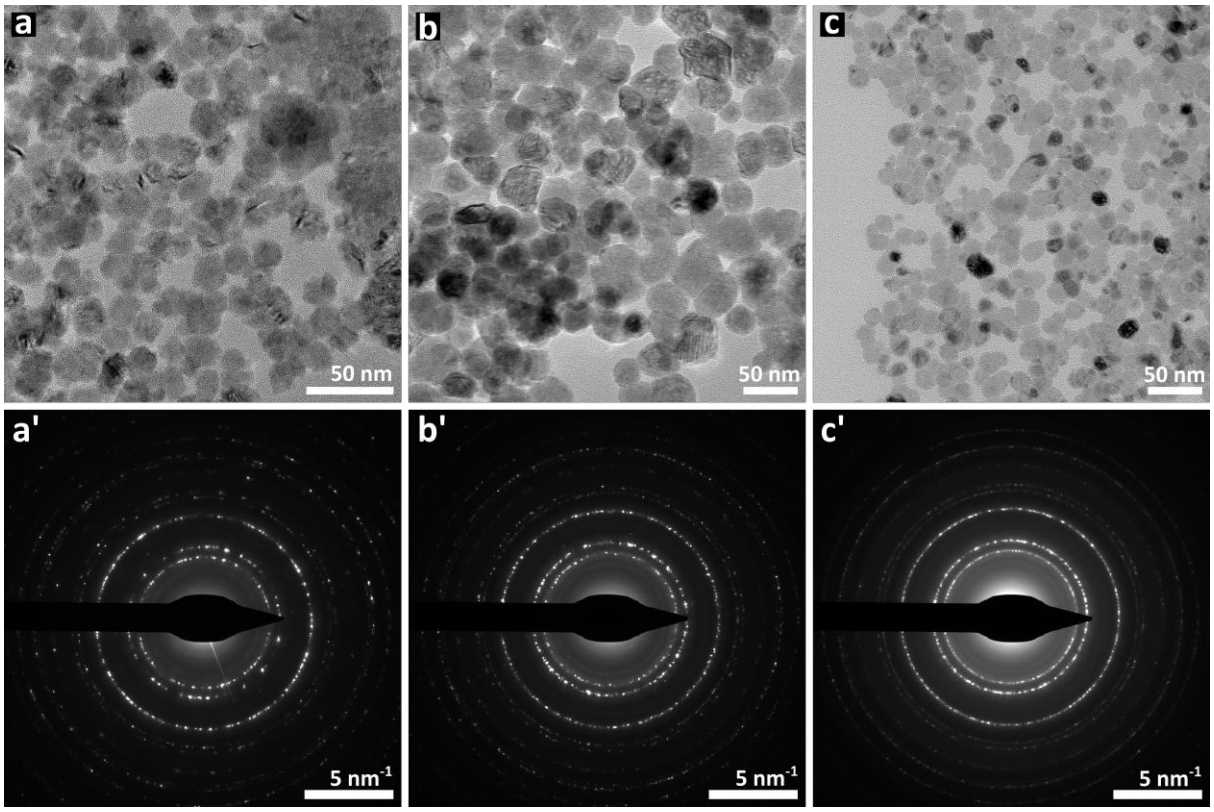

Figure 3.4: MnO particles resulting from the synthesis with recrystallized KCl heated under N_2 atmosphere (a), new KCl heated under N_2 atmosphere (b), and new KCl heated under Ar atmosphere (c), with respective diffraction patterns (') indicating a *c*-MnO phase.

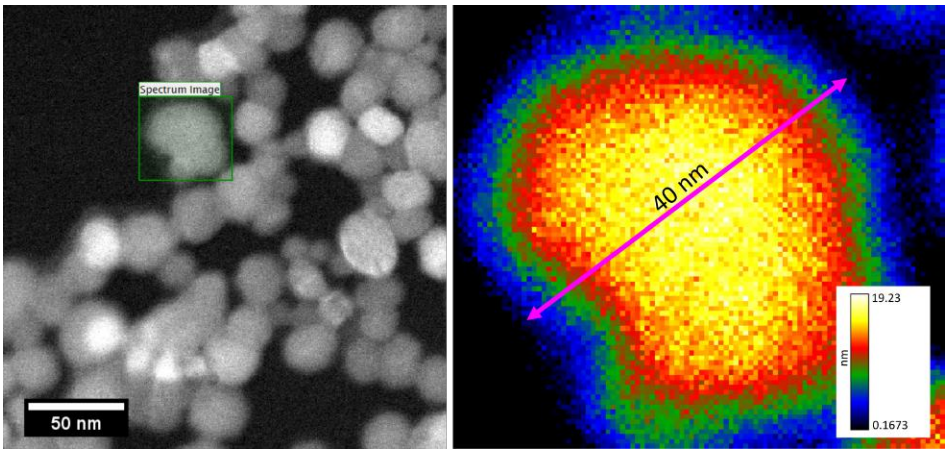

Figure 3.5: EELS thickness mapping of a MnO particle showing a thickness of 19 nm.

the nanoparticles were not small sheets but 3D structures. The same synthesis was repeated with lower heating temperatures of 300 and 350 °C for 1h, which also resulted in small particles. A higher initial Mn concentration (500 mg $Mn(CH_3COO)_2 \cdot 4H_2O$) and a higher ramping rate (10 °C/min) were also tested, but resulted in particles instead of sheets, see Fig. A.4.

Finally, the synthesis was attempted in a tube oven under Ar atmosphere, and the resulting particles are shown in Fig. 3.4c. Although this procedure in Ar atmophere is also described in the work of Xiao *et al.*,[15] it was not of easy access and in principle should not differ significantly from the properties of the N_2 atmosphere. Indeed, the particles from the synthesis in the Ar oven were very similar to those heated under N_2 atmosphere. They appeared to be spherical MnO nanoparticles with tens of nanometers in size, see Fig. 3.4c.

3.2.3. MnO-N_2 Heating

The MnO nanoparticles obtained by calcinating the Mn-precursor@KCl under N_2 atmosphere were heated *in-situ*. The 10 day old MnO particles were dropcasted on a DENSsolutions heating chip (without holes) and heated *in-situ* with 100 °C increments up to 600 °C, waiting 10 min at every temperature before imaging. The area followed during the heating is shown in Fig. 3.6a. The image shows that the particles are surrounded by a thin amorphous carbon layer.

Fig. 3.6b shows the intensity profiles of the diffraction patterns shown in Fig. 3.6c-h taken before and during the heating experiment. The nanoparticles were cubic MnO right after the synthesis, as is also shown in Fig. 3.4. However, the observed lattice of the cubic MnO particles is slightly larger than in the reference bulk structure. The three most intense peaks in the reference bulk MnO are located at 2.57 Å, 2.22 Å, and 1.57 Å, whereas the respective peaks in these particles are located at 2.66 Å, 2.32 Å, and 1.63 Å. This is probably related to the MnO being on the nanoscale, where the equilibrium lattice can differ from the respective bulk lattice due to the increased surface-to-volume ratio.

Already at room temperature, a change could be observed in the particles imaged 10 days after the synthesis. The diffraction pattern shown in Fig. 3.6d is completely different from the diffraction pattern taken 1 day after the synthesis, and is now indicating the Mn_3O_4 phase. Although there are some very faint rings present at high d-spacings in the diffraction pattern of the 1 day old particles that could indicate a minor Mn_3O_4 phase, see Fig. 3.6c, the intense rings clearly correspond to the MnO phase. In the 10 day old particles however, the 2.66 Å and 2.32 Å peaks are completely absent, indicating a full transformation to Mn_3O_4 without the presence of a minor MnO phase.

The sample was first heated to 100 °C, where it was severely contaminated during the imaging. This was probably caused by the residual organics present in the sample, which are more reactive at this increased temperature. No further imaging was conducted at this temperature to prevent the complete

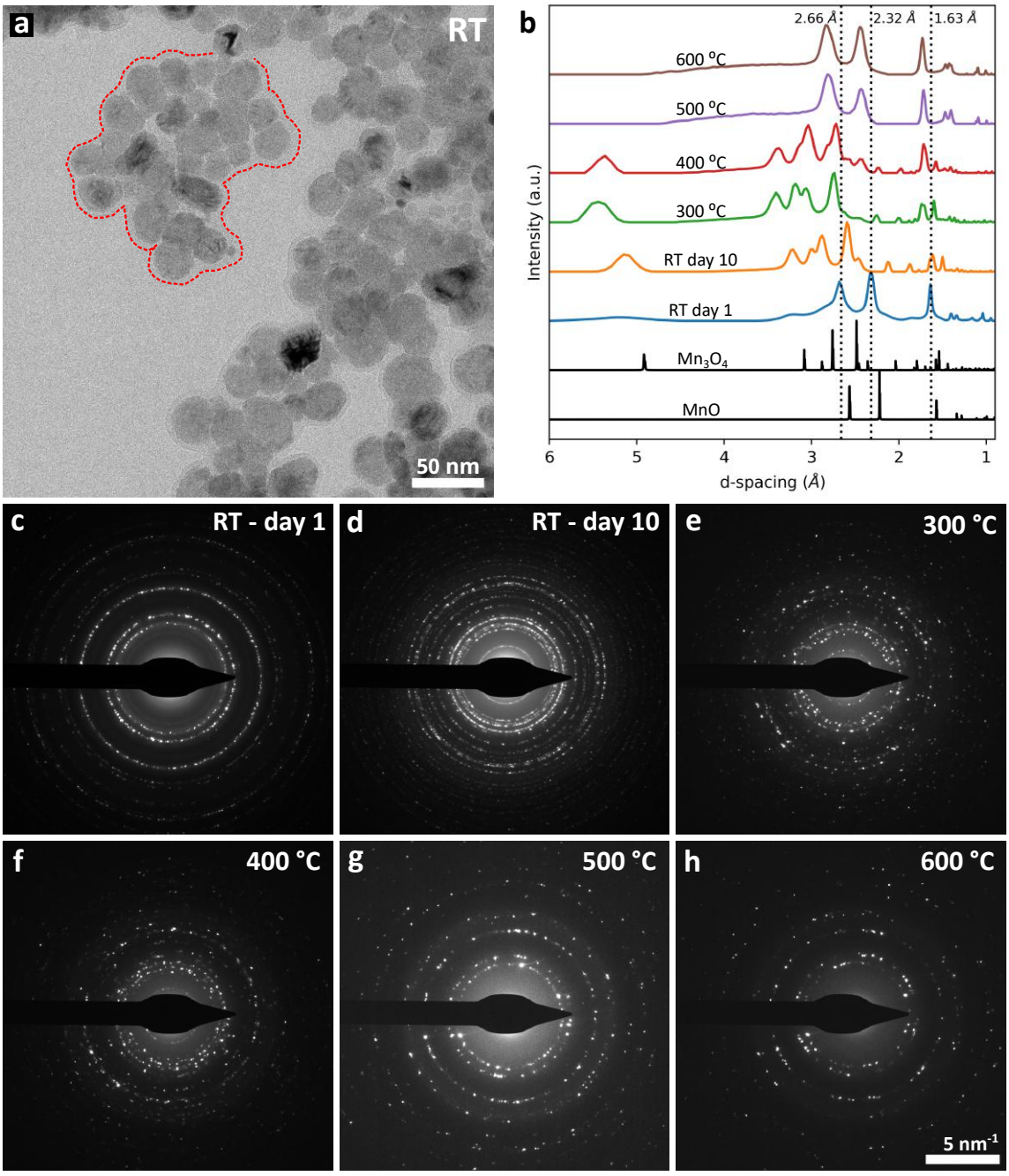

Figure 3.6: TEM image of the sample area followed during the *in-situ* heating to 600 °C, with the red dashed line indicating the presence of an amorphous layer (a). Diffraction profiles (b) and corresponding diffraction patterns (c-h) taken during the heating indicate a transformation from Mn_3O_4 to MnO. The scalebar is the same for all diffraction patterns. Reference patterns are from MnO ($Fm\bar{3}m$)[54] and Mn_3O_4 (I41/amd:1)[55].

contamination of the sample. The sample was further heated to 600 °C with increments of 100 °C. At every temperature from 300 °C, an electron diffraction pattern was acquired from the same region, as shown in Fig. 3.6. As mentioned before, the diffraction pattern at room temperature changed in the time between the synthesis and the heating experiment. At 300 °C and 400 °C, the rings from the room temperature diffraction indicating the Mn_3O_4 phase remained. However, a decrease in the number of reflections indicates that the polycrystallinity of the sample decreased. This is not surprising, as the increased temperature enables restructuring to an energetically favorable composition, which reduces the number of lattice orientations. However, at 500 °C and 600 °C, the diffraction pattern changed again and was similar to the pattern obtained directly after the synthesis, indicating a cubic MnO morphology. This suggests that, somewhere between 400 °C and 500 °C, the particles reduced back from Mn_3O_4 to MnO.

Because of the SiN_x film, some features of the MnO_x particles could not be imaged. Therefore, the sample was also heated with a heating chip in which holes were etched with a focused ion beam, as shown in Fig. 3.7a. This time, the sample was heated to 500 °C in a single step. The particles were a mix of MnO and Mn_3O_4 at room temperature, as indicated by diffraction (see Fig. 3.7c). At 500 °C, the diffraction pattern shows that the particles were still a mix of MnO and Mn_3O_4 phases, whereas they were already reduced to MnO at this temperature in the previous heating experiment. The temperature was further increased to 700 °C, where the diffraction pattern indicates that the particles reduced to MnO. It was also observed that the particles become more edged during the heating, see Fig. 3.7h. At room temperature, the particles look semi-spherical without defined edges. The images at higher temperatures show that the particles become faceted. This indicates that certain lattice planes are energetically favored. When the sample was cooled, the edges immediately disappeared again, see Fig. 3.7i, but the MnO phase remains, see Fig. 3.7g.

Eleven days after the heating experiment, the particles were investigated using HAADF-STEM imaging. Fig. 3.8 shows some of the MnO_x particles that were observed. Both *c*-MnO (Fig. 3.8a and b) and *t*-Mn_3O_4 particles (Fig. 3.8c and d) were identified, confirming that there is a mix of MnO and Mn_3O_4 phases present and thus that the Mn_3O_4 to MnO reduction is reversible. Moreover, the d-spacings observed in the MnO particles correspond to the observed increased d-spacing compared to the bulk *c*-MnO observed in the previous diffraction patterns (Figs. 3.6b and 3.7).

Since it was found that the particles spontaneously oxidized to Mn_3O_4 under ambient conditions, a closer look was taken at aged unheated particles. A HAADF-STEM image from a MnO_x particle is shown in Fig. 3.9a, with the corresponding fast Fourier transform (FFT) of the marked area shown in Fig. 3.9b. The reflections that are found in the FFT of the particle indicate the presence of both the MnO and Mn_3O_4 phases. There are high intensity spots at a d-spacing of 2.62 and 2.58 Å, which correspond to the (111) reflection of MnO, and a high intensity spot at a d-spacing of 2.23 Å corresponding to the (200) reflection of MnO. However, there are also reflections at a d-spacing of 4.93 Å and 4.90 Å, corresponding (101) of Mn_3O_4, and at 2.79 and 2.78 Å originating from the (103) plane in Mn_3O_4. These cannot originate from the MnO lattice, indicating phase coexistence between the two phases in this particle. The reflections indicate the zone-axis is [110] for the MnO and [100] for the Mn_3O_4 phase. Therefore, there must be lattice matching between these two planes. Fig. A.5 shows the configurations and theoretical diffraction patterns of these planes, indicating that the (002) MnO reflection matches with the (004) Mn_3O_4 reflection, and the (111) MnO reflections match with the (022) Mn_3O_4 reflections. The theoretical diffraction patterns also show that the FFT in Fig. 3.9b cannot originate from a distorted Mn_3O_4 lattice since the relative intensity of the (022) spots is much lower than observed, thereby indicating that it is likely a contribution from both the (111) MnO and (022) Mn_3O_4 reflections. The lattice mismatch is 4.3% between the (111)MnO/(022)Mn_3O_4 planes, and 6.3% between the $(002)_{MnO}/(004)_{Mn3O4}$ planes.

The FFT shown in Fig. 3.9b is taken from the center of the particle. At the surface, however, it is clear that the phase is Mn_3O_4 since the atoms are clearly configured according to the (100) plane of Mn_3O_4 (also shown in Fig. 3.8c). Therefore, it can be concluded that the oxidation of the MnO particles

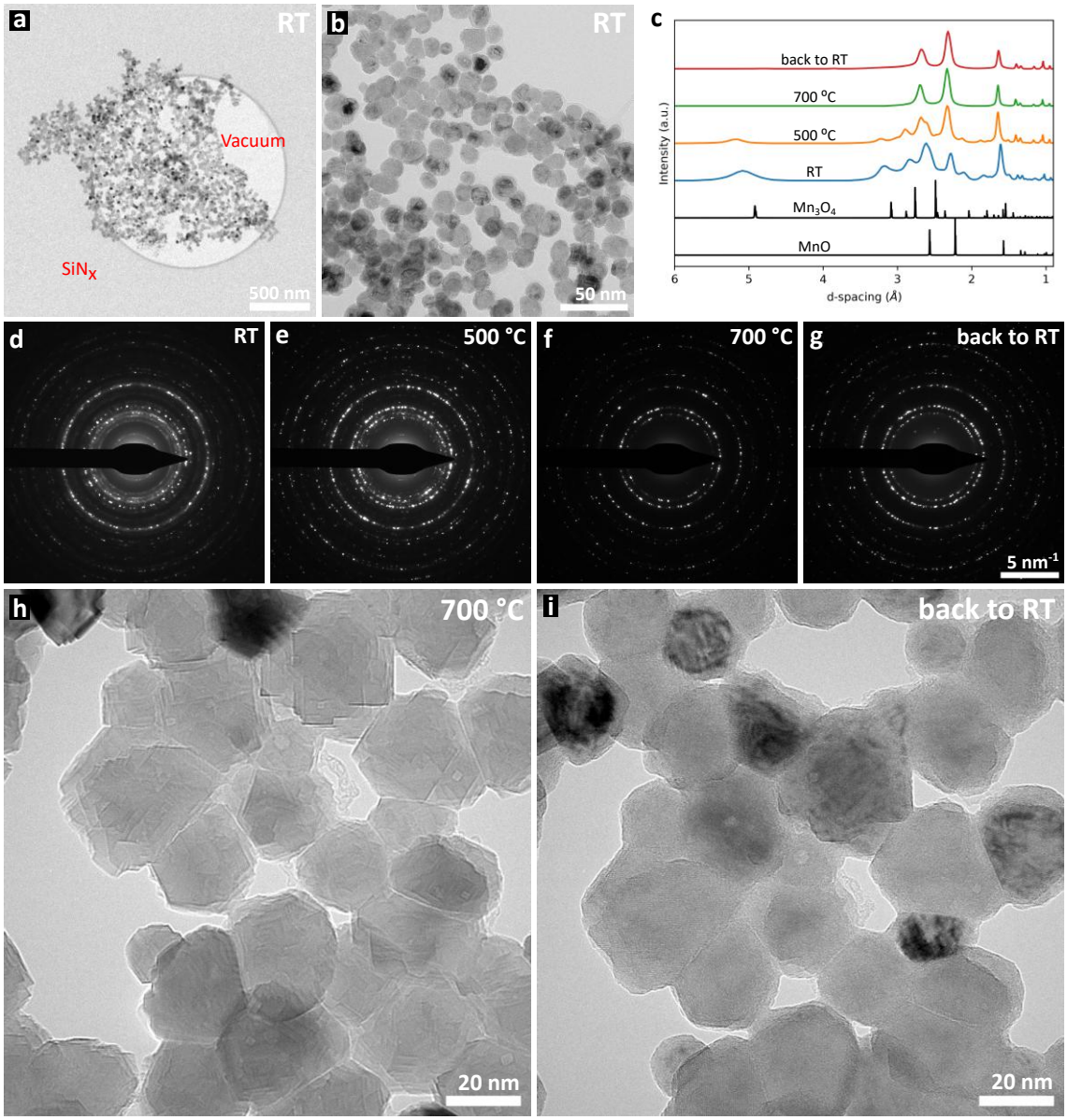

Figure 3.7: MnO_x particles heated *in-situ* to 700 °C. Holes were etched in the SiN_x window of the heating chip (a). The area that was followed is shown in (a) and (b), and the diffraction profiles (c) of the diffraction patterns (d-g) indicate a transformation from Mn_3O_4 to MnO. The particles are more edged at high temperatures (h), which is lost when the material is cooled again (i). The scalebar is the same for all diffraction patterns. Reference patterns are from MnO ($Fm\bar{3}m$)[54] and Mn_3O_4 (I41/amd:1)[55].

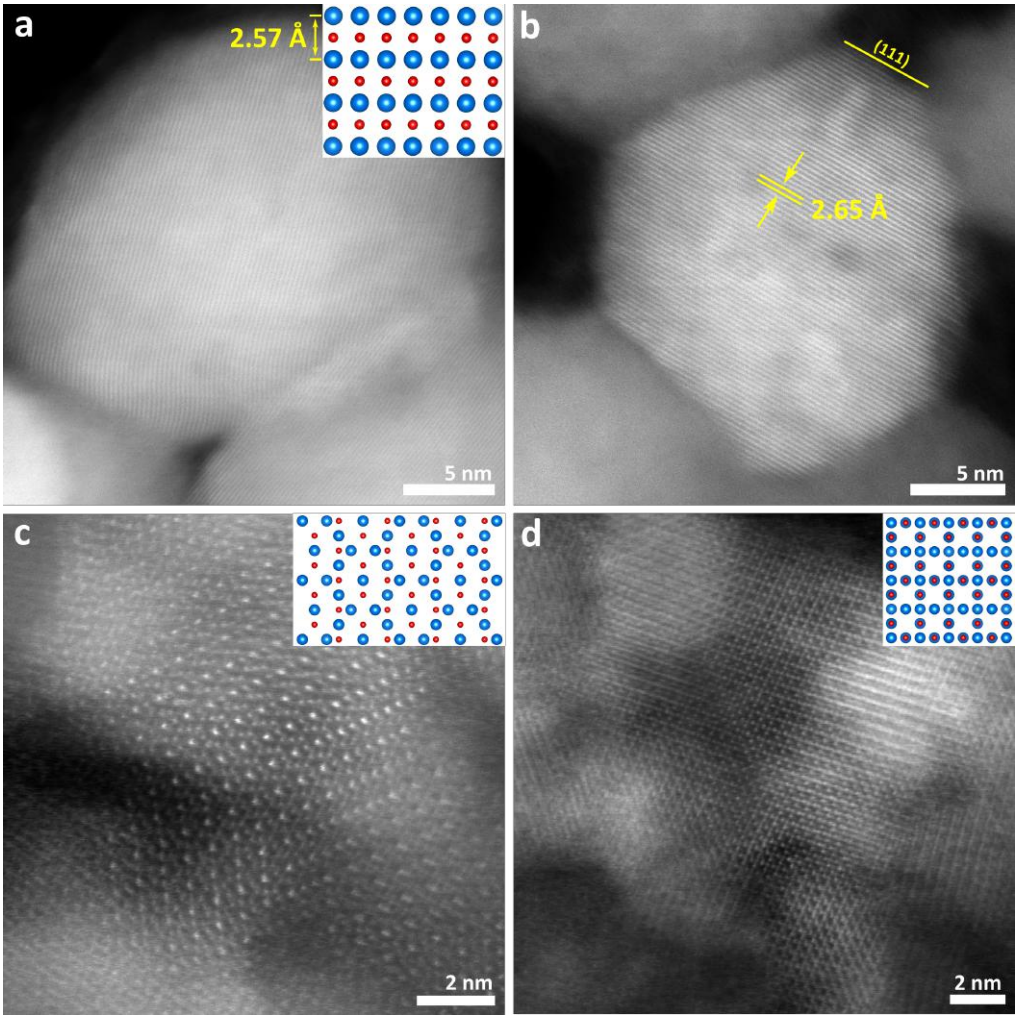

Figure 3.8: MnO_x particles after heating to 700 °C imaged with HAADF-STEM. (a) and (b) show MnO particles, with the inset showing the (121) plane of *c*-MnO. (c) and (d) show Mn_3O_4 particles, with the insets showing the (010) plane (c) and (001) plane (d) of *t*-Mn_3O_4.

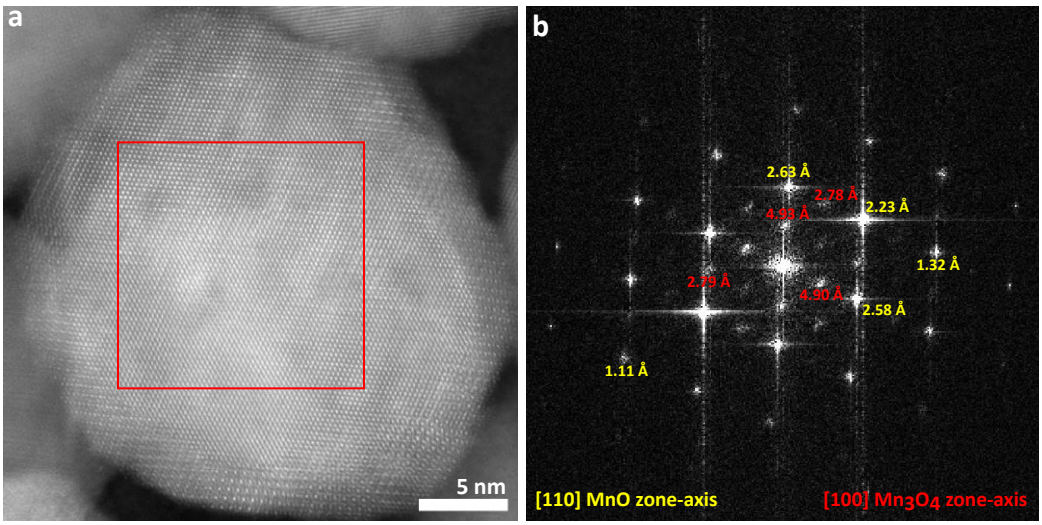

Figure 3.9: HAADF-STEM image of a MnO_x particle (a) and FFT (f) of the indicated area showing coexistence of the MnO (yellow) and Mn_3O_4 (red) phases.

progresses from the surface to the center of the particle.

In summary, we observed a reversible transformation of *c*-MnO to *t*-Mn_3O_4. The synthesized particles are MnO directly after the synthesis but naturally oxidize to Mn_3O_4 over time. This is probably caused by the lower energy of the Mn_3O_4 configuration, making it thermodynamically more favorable. When heated *in-situ*, the particles transform back to MnO, which oxidizes to Mn_3O_4 again at room temperature. The ease by which the transformation occurs indicates that the transformation from MnO to Mn_3O_4 in these nanoparticles does not have a high energy barrier. This could be interesting for reactions in which Mn_3O_4 can act as an oxidizing agent, because the used Mn_3O_4 can be easily recovered by aging under ambient conditions.

3.2.4. MnO-Ar Heating

The MnO particles that were calcinated under Ar atmosphere were also heated *in-situ*. The dispersion of MnO particles in ethanol was dropcasted on a DENSsolutions heating chip in which holes were etched with a focused ion beam. Three areas were followed during the heating of the MnO particles, which are shown in Fig. 3.10ace, and each area displayed different features.

In the first area, MnO particles were embedded in a relatively thick amorphous carbon layer. As can be seen in Fig. 3.10a, it is hard to see the edges of the particles and there are no lattice fringes visible. The carbon layer covered the entire hole in the SiN_x film, and no vacuum could be seen. The phase evolution of the particles in this first area can be seen from the diffraction profiles in Fig 3.10b. This time, the phase of the MnO particles did not change between the synthesis and the heating experiment. The particles were MnO immediately after the synthesis (see Fig. 3.4) and remained stable. The observed slightly increased lattice spacing compared with that of the MnO reference is also consistent with the previous experiments. The phase of the particles did not change during the heating and remained MnO. Note that the diffraction pattern at 100 °C was obtained with a different camera lens (410 mm instead of 660 mm) and therefore has a differently sized beam-stopper causing the high d-spacing information to be lost. The image was scaled such that all images (see Fig. A.6) have the same scale bar. The reason for the particles to remain stable in this area is probably the thick carbon layer, which protects the MnO particles from external influences that could oxidize them.

The second area that was followed during heating is shown in Fig. 3.10c. In this area, there was still some amorphous carbon around the particles, but it was much less than in the first area. The carbon layer does not cover the entire hole in the SiN_x window of the heating chip, and a clear distinction between the particles, carbon, and vacuum can be made. Moreover, lattice fringes can be easily observed in the HRTEM images. The diffraction profiles at each temperature are shown in Fig. 3.10d. The particles started as a mixture of MnO and Mn_3O_4 phases. The three main peaks of MnO are present at their usual positions, but there are also diffuse peaks at higher d-spacings that correspond to Mn_3O_4, which can be seen more clearly in the diffraction pattern in Fig. A.7. When the sample is heated, the Mn_3O_4 phase starts to dominate, which can be concluded from the appearance of small distinct peaks at d-spacings above 2.66 Å, and in between 1.63 and 2.32 Å, which cannot originate from the MnO structure. A peak also appears at a d-spacing above 5 Å, which can be seen even better in the diffraction patterns in Fig. A.7, and is a clear feature of the Mn_3O_4 structure. Only at 800 °C are the particles reduced back to MnO. Interestingly, when cooling back to room temperature, the structure changes immediately and appears to display features of the Mn_3O_4 structure, indicating that the particles are again a mixture of MnO and Mn_3O_4. From this, we can infer that two things are happening during the heating of the MnO_x particles. At elevated temperatures, the atoms obtain more translational energy and can therefore move to a more favorable position. Because Mn_3O_4 is lower in energy than MnO, it is thermodynamically favorable for the particles to transform into the Mn_3O_4 phase. However, the increased temperature in combination with the vacuum conditions and perhaps the reducing properties of the electron beam also cause the particles to reduce to MnO. The interplay among temperature, vacuum, and electron beam causes the

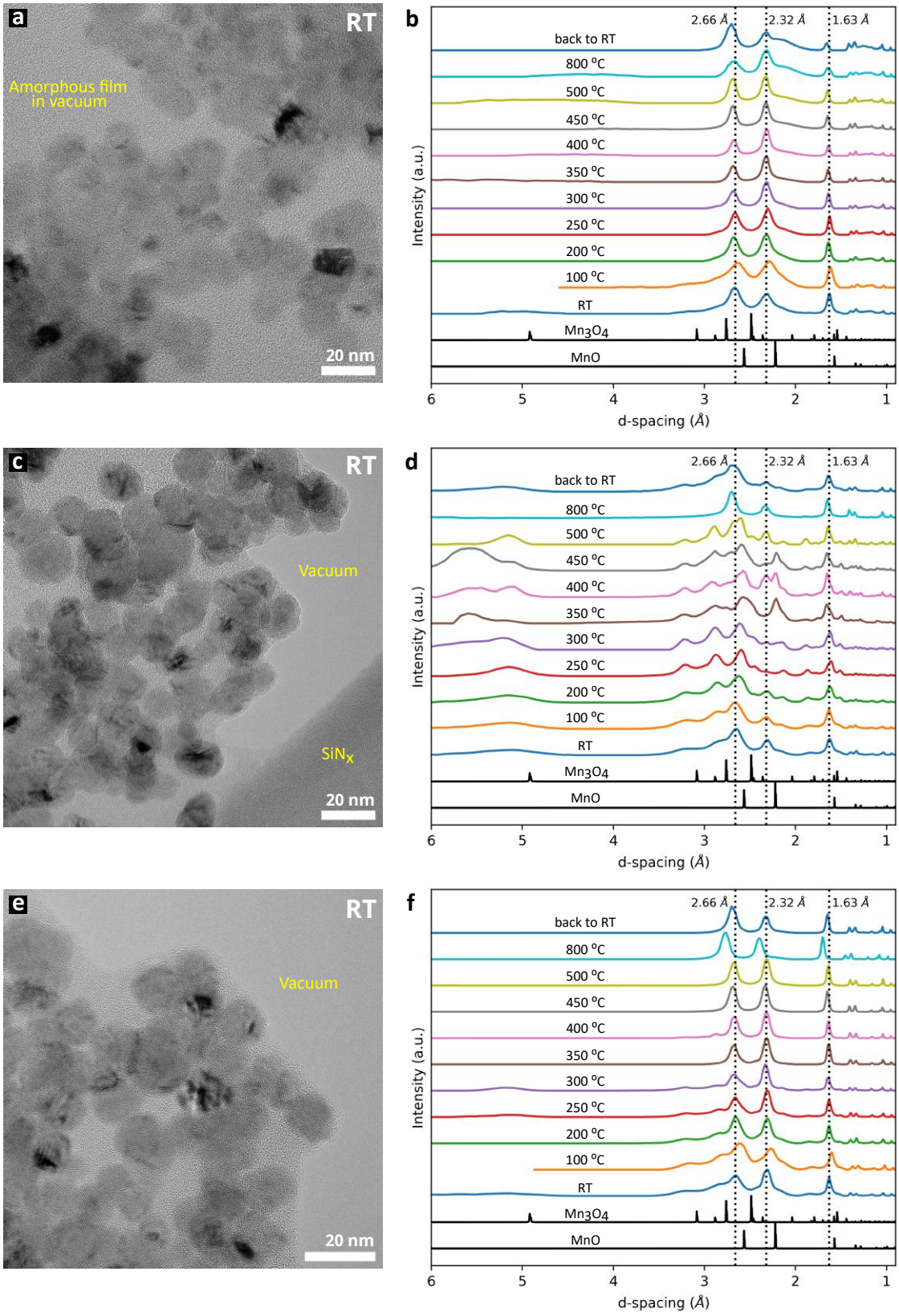

Figure 3.10: Different areas followed during the heating of MnO particles annealed in Ar atmosphere. Areas are numbered 1 to 3 and TEM images taken at room temperature are displayed in (a), (c), and (e) respectively. Diffraction intensities as a function of d-spacing at each temperature for area 1 to 3 is displayed in (b), (d), and (f) respectively. The respective ring diffraction patterns can be seen in Figs A.6-A.8. Reference patterns are from MnO ($Fm\bar{3}m$)[54] and Mn_3O_4 (I41/amd:1)[55].

particles to transform from mixed MnO/Mn_3O_4 to Mn_3O_4 and then back to MnO. The question that remains is where the oxygen originates from in the transition from MnO to Mn_3O_4. Unlike the transition from MnO to Mn_3O_4 under ambient conditions, there is little to no available oxygen in the vacuum of the TEM that can oxidize the MnO particles. A study investigating the reversible MnO/Mn_3O_4 transition induced by electron beam interactions also observed the MnO to Mn_3O_4 transition in vacuum.[58] They claim that the MnO to Mn_3O_4 transition can be caused by the interaction of molecular oxygen with the electron beam by the following reaction: $O_2 + e^- \rightarrow O^- + O$, in which the O^- are adsorbed oxygen anions. Basically, the electron beam accelerates the uptake of oxygen from the TEM column by the lattice. This has also been verified by Kwon *et al.*[59], who found that Cu wires were stable in the high-vacuum of the TEM for at least 36h, but oxidized in a matter of minutes when the beam was turned on. Another possible mechanism is the formation of Mn vacancies via the knock-on effect, which causes the atomic percentage of Mn to decrease. Because the energy threshold for displacing Mn is approximately four times lower than that for O [58], it is possible that the ratio changes to such an extent that the MnO to Mn_3O_4 transition can occur. At elevated temperatures, the atoms already have a higher translational energy, causing the required knockout energy to be lower, thereby easing the transition of MnO to Mn_3O_4 under the electron beam. Because the MnO to Mn_3O_4 transition in vacuum was only observed in one area that was exposed to the electron beam, beam effects cannot be excluded. Further experiments are required to elucidate the exact underlying mechanisms.

In the third area, there was again a carbon layer (see Fig. 3.10e), which is probably somewhere between the first and second area in thickness. Fig. 3.10f shows the diffraction profiles of the particles during the heating. The particles start as a mix between MnO and Mn_3O_4 again but are fully transformed to MnO at 450 °C already. The particles also gradually changed to MnO and did not transform into Mn_3O_4 first before becoming MnO. The diffraction patterns are shown in Fig. A.8.

In summary, in addition to the reversible MnO to Mn_3O_4 transformation that was observed in the heating of the MnO particles synthesized under N_2 atmosphere, we observed that the transformation to Mn_3O_4 depends on the thickness of the amorphous layer on which the particles reside. The amorphous layer acts as a stabilizing agent, probably protecting the MnO particles from external influences that cause them to oxidize. This stability is thickness-dependent, meaning that the time it takes to oxidize the MnO particles can be controlled by the thickness of the amorphous layer and even prevent oxidation completely when the thickness is sufficient.

3.2.5. Manganese(II) Acetate Precursor Heating

To study the formation of MnO during the calcination of manganese(II) acetate tetrahydrate, the precursor solution was heated *in-situ* in the TEM. For this experiment, 2 μL of a 10 mM solution of $Mn(CH_3COO)_2 \cdot 4H_2O$ in ethanol was dropcasted on a DENSsolutions heating chip. The ethanol was allowed to evaporate before the heating holder containing the heating chip was inserted into the TEM. When the holder was inserted, the temperature was immediately increased to 100 °C to remove any organic impurities that might be present. The temperature was then further increased in increments of 50 °C, and left for 10 min at each temperature before imaging.

During heating, electron diffraction patterns were recorded at each temperature to follow the crystallization of the material, as shown in Fig. 3.11. At 100 °C, the diffuse rings indicate that the material was still amorphous. Starting from 250 °C, the rings became more defined and can be indexed as the *c*-MnO phase. Until 400 °C, the rings never become sharp, which can be attributed to the thickness of the material layer. The sample was further annealed at 400 °C for about 1h, after which the diffraction pattern of a different area shows sharp rings corresponding to *c*-MnO. Therefore, we can conclude that the manganese acetate precursor decomposes to form MnO in vacuum.

TEM images of an area that was followed during the heating can be seen in Fig. 3.12. At 150 °C, this area did not show much texture. However, at 200 °C, dark spots started to appear, which are

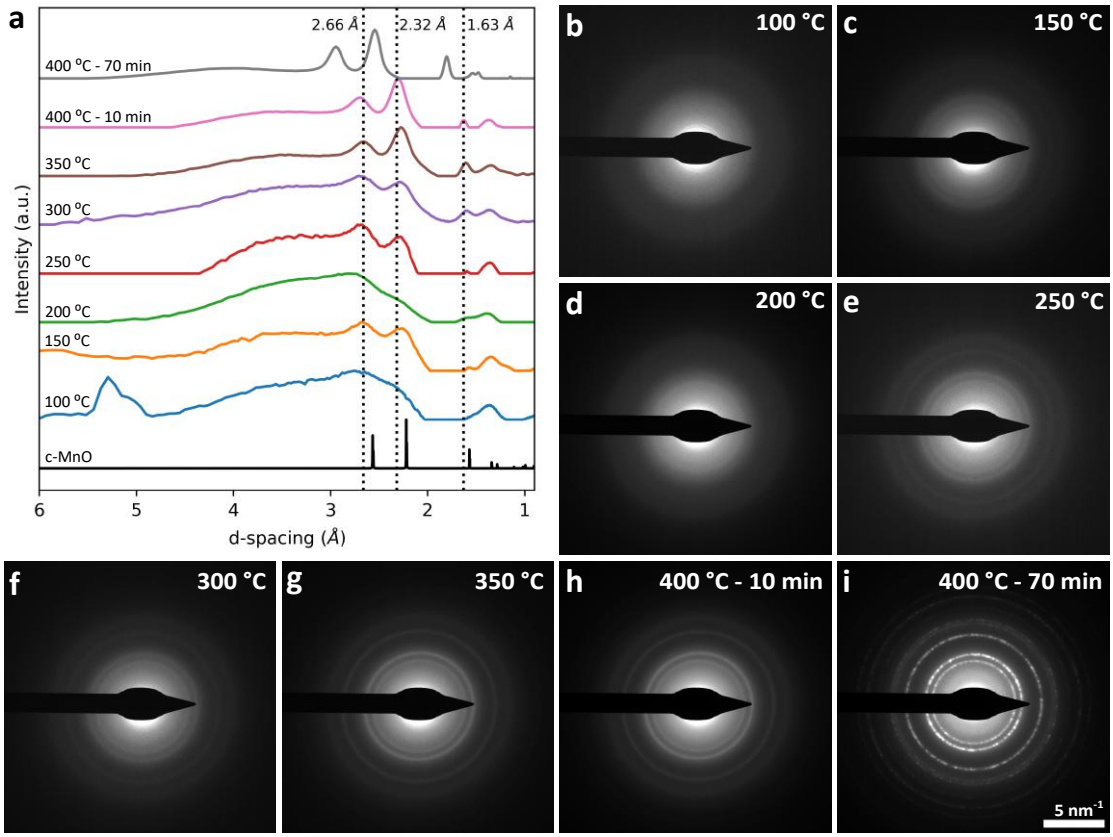

Figure 3.11: Electron diffraction profiles (a) and corresponding diffraction patterns (b-i) of the manganese(II) acetate precursor at different temperatures. The sample starts out amorphous. From 250 °C, the rings become more defined and the *c*-MnO phase can be confirmed. Note that the diffraction pattern taken after 70 minutes at 400 °C is from a different area than the rest of diffraction patterns. The scalebar is the same for all diffraction patterns. Reference patterns are from MnO ($Fm\bar{3}m$)[54] and Mn_3O_4 (I41/amd:1)[55].

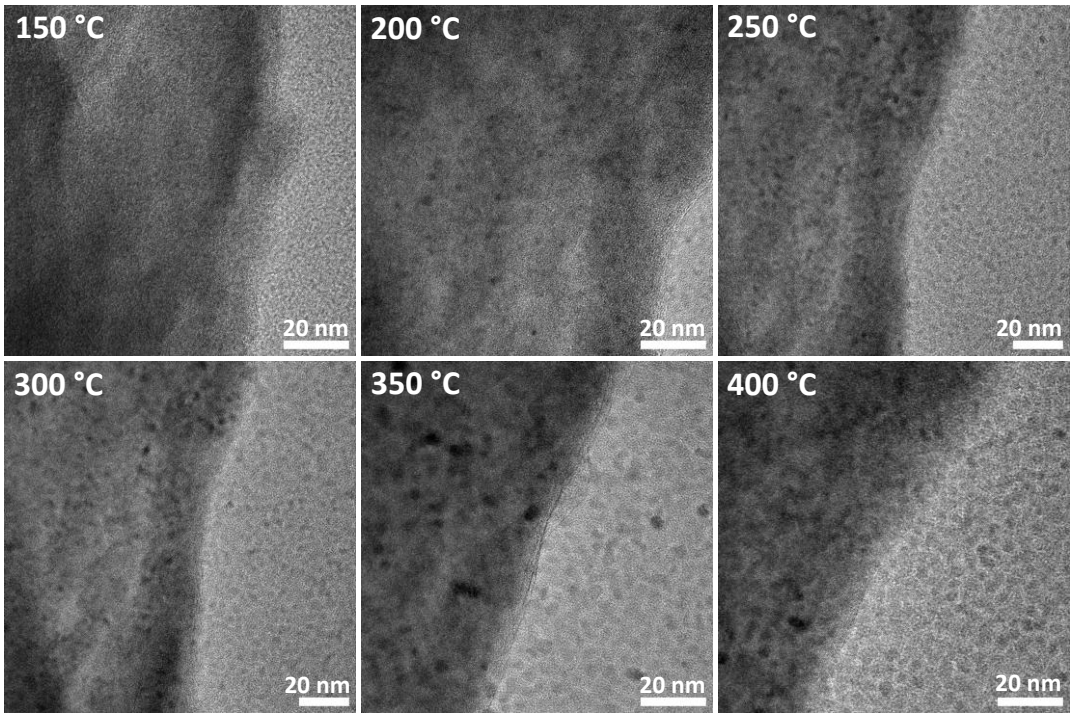

Figure 3.12: Area followed during the heating of the manganese(II) acetate precursor showing the onset of crystallization at 200 °C and the formation of nanoparticles that do not combine into a single film.

crystallization sites. These spots grew in number and size during further heating of the precursor to 400 °C. However, it can be seen that the crystallites never combine into one layer. At 400 °C, the crystals are still small in size, similar to nanoparticles, and they do not attach. This is similar to the nanoparticle arrays synthesized using the salt-templating method, both for annealing under N_2 and Ar atmospheres. Instead of a single-crystal nanosheet, many nanoparticles were formed, which lay on an amorphous carbon layer. Because the precursor also forms particles instead of layers, it is hypothesized that there is also an amorphous carbon layer around the MnO particles formed during the decomposition of the pure precursor, causing them to remain isolated and keeping them from combining into a single film. The amorphous carbon layer might have originated from the acetate ions of the precursor. From these results, we can infer that it is simply not possible to obtain nanosheets when manganese acetate is used as the precursor.

3.2.6. On the Formation of Nanocrystal Arrays Instead of Nanosheets

Instead of the desired MnO nanosheets, arrays of MnO nanoparticles on amorphous carbon were obtained. In this section, possible causes for this are discussed.

The first question is where the amorphous carbon layer originates from. There are two sources of carbon in the synthesis: acetate ions in the manganese(II) acetate precursor and the ethanol in which it is dissolved. In principle, the ethanol is evaporated before calcination of the precursor. Therefore, it is unlikely that ethanol is the source of carbon, especially because amorphous carbon is found in considerable amounts, which cannot originate from a small amount of ethanol that might not have evaporated before calcination. Therefore, the only source of carbon can be the acetate ions. A similar material was obtained by Wang *et al.*[60] by calcinating manganese oleate with the help of NaCl templates to obtain MnO/C nanosheets, in which the oleate is also the only carbon source. However, another research paper that obtained MnO/C nanosheets did add another source of carbon and obtained pure MnO when calcinating manganese acetate when carbon was not added.[14] Therefore, it is still uncertain if the acetate ions could cause the carbon layer to form.

The second question is whether the amorphous carbon is the cause of the formation of nanoparticle arrays, or if the KCl templates that are used are somehow not suitable for guiding the growth of MnO nanosheets. As mentioned in the theory, the proposed mechanism for the growth of MnO nanosheets is the close lattice matching of the rotated KCl lattice. If the quality of the KCl crystals is not sufficient to facilitate this lattice directing, then MnO sheets might not be able to form. Different KCl crystals were investigated with SEM, and at least the recrystallized KCl displayed sufficient quality to facilitate lattice directing. However, even using the recrystallized KCl resulted in nanoparticle arrays. Moreover, Xiao *et al.*[61] also synthesized Mn_2N_3 nanosheets (for which MnO nanosheets were synthesized as an intermediate) using the KCl templating method, and their KCl templates, as displayed in their supplementary information, look very similar to the KCl crystals from the new stock that was used in the syntheses to obtain MnO nanoparticles, as displayed in Fig. 3.3c. Therefore, it is unlikely that the quality of the KCl template prevented the formation of MnO nanosheets. Another reason could be that the KCl lattice is not matching sufficiently with the cubic MnO lattice, causing other growth mechanisms rather than Frank-van der Merwe film growth.[56] It was observed that the cubic MnO lattice was slightly larger than the bulk MnO lattice. According to the experimental data, the lattice of the MnO nanoparticles has a lattice constant of 4.64 rather than 4.44 Å, which is a 4.5 % increase. The lattice mismatch with KCl is then 4.58 % rather than 0.11 %, which is significantly larger and falls in the Stranksi-Krastanow growth regime enabling island growth.[56] However, this increased lattice parameter of MnO should, in principle, have also been present in the synthesis by Xiao *et al.*. The formation of particles rather than sheets must therefore be caused primarily by the amorphous carbon layer.

3.3. MnO nanosheets

3.3.1. Experimental

It is apparent from the previous section that it is not possible to synthesize MnO nanosheets using manganese(II) acetate as the precursor. Therefore, the synthesis procedure reported by Xiao *et al.*[15] has been modified.

In a typical synthesis, 50 g of KCl ($\geq$ 99.0%, Sigma-Aldrich no. P3911) was used. Then, 50 mg of manganese(II) chloride tetrahydrate ($MnCl_2 \cdot Cl_2$, $\geq$ 98.0%, Sigma-Aldrich no. M8054) was weighed and dissolved in 5 mL of absolute ethanol by magnetic stirring at 200 rpm for 5 min. After the manganese chloride was fully dissolved, it was added to the KCl and stirred. After the salt was completely wetted by the manganese solution, it was heated on a 70 °C hotplate for 20 minutes to evaporate the ethanol, after which it was completely dry again. The salt was then transferred to a ceramic heating boat and heated in a 400 °C tube oven under N_2 atmosphere for 3 h, with prior ramping of 2 °C/min. The MnO@KCl was allowed to cool to room temperature naturally before being removed from the oven and dissolved in water, resulting in an orange solution. The MnO nanosheets were removed from the solution by vacuum filtering and the powder was dispersed in 3 mL of absolute ethanol. Fig. A.2 shows the Mn coated salt before and after heating, and the MnO nanosheet dispersion obtained after removal of the KCl templates. Comparing with the synthesis using manganese(II) acetate as shown in Fig. A.1, the heated salt is more orange and lighter in color. The MnO nanosheet dispersion is also much lighter in color than the MnO_x nanoparticle arrays. However, it was more difficult to remove the MnO nanosheets from the filter paper after vacuum filtration, so the lighter color is probably partly due to a lower concentration.

TEM imaging was performed using a TFS Talos F200X microscope operating at 200 kV. The EELS thickness maps were obtained using the TFS Spectra 300 operating in STEM mode at 300 kV. The heating experiments were carried out using the DENSsolutions wildfire *in-situ* holder in the TFS Talos F200X TEM. For the heating experiments, the MnO_x dispersion was dropcasted on the DENSsolutions MEMS heating chip, containing a silicon nitride (SiN_x) film in which holes were made using the TFS Helios G3 FIB-SEM.

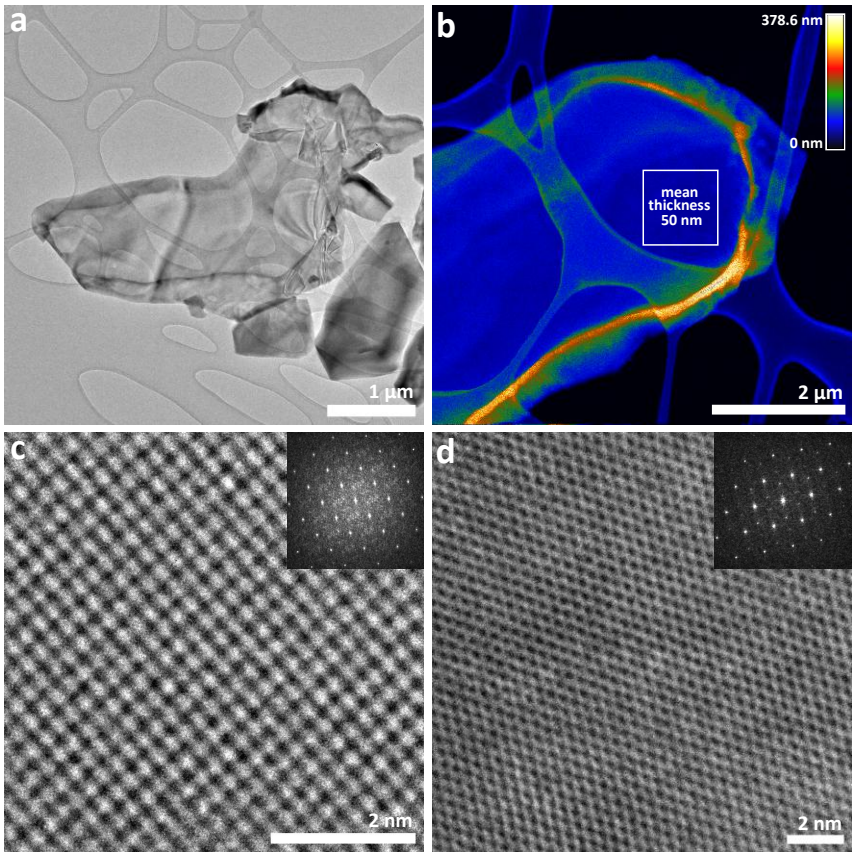

Figure 3.13: MnO nanosheets at room-temperature. TEM image of nanosheet (a), EELS thickness map of nanosheet indicating a thickness of 50 nm (b), and HRTEM images of observed square (c) and trigonal (d) lattices.

3.3.2. Nanosheet Characterization

The nanosheets obtained using the above experimental procedure were generally several micrometers in size. Fig. 3.13a shows a nanosheet as imaged by TEM. It can be seen that the nanosheet had some folds and wrinkles. Sometimes, particles and thicker crystals were present around the nanosheets. The thickness of the nanosheets was obtained from EELS mapping. A representative EELS thickness map is shown in Fig. 3.13b, where the mean thickness in the square area was 50 nm. This means that the nanosheets are not as thin as those from the method paper, which were 1 nm thick, as measured by atomic force microscopy (AFM).[15] Using less manganese chloride precursor (7 mg per 50 g of KCl) resulted in smaller but not thinner sheets. The observed sheets had both square (Fig. 3.13c) and trigonal (Fig. 3.13d) lattices. However, the observed square lattice had lattice spacings of 2.46 Å and 3.05 Å in the two directions, whereas the expected lattice spacing derived from the c-MnO bulk phase is 2.22 Å in both directions. It is hypothesized that the lattice is square immediately after synthesis, owing to the use of the KCl template, but transforms to a trigonal lattice when the template is removed. The observed lattice spacings of the square lattice indicate that the lattice is already restructuring. The full HRTEM image of which part is shown in Fig. 3.13d is shown in Fig. A.9, where it can be seen from the lattice fringes that the sheet is not lying flat but is slightly wavy. Further analysis of this lattice is shown in Fig. 3.14.

Fig. 3.14 shows the FFT (b) and diffraction pattern (c) of a trigonal looking sheet of which the HRTEM image is shown in 3.14a. Fig. 3.14d shows the theoretical diffraction pattern of the t-MnO phase as described by the lattice parameters listed in Table 3.1. The annotated FFT and diffraction pattern are shown in Fig. 3.14e and f respectively. The FFT pattern is similar to the theoretical

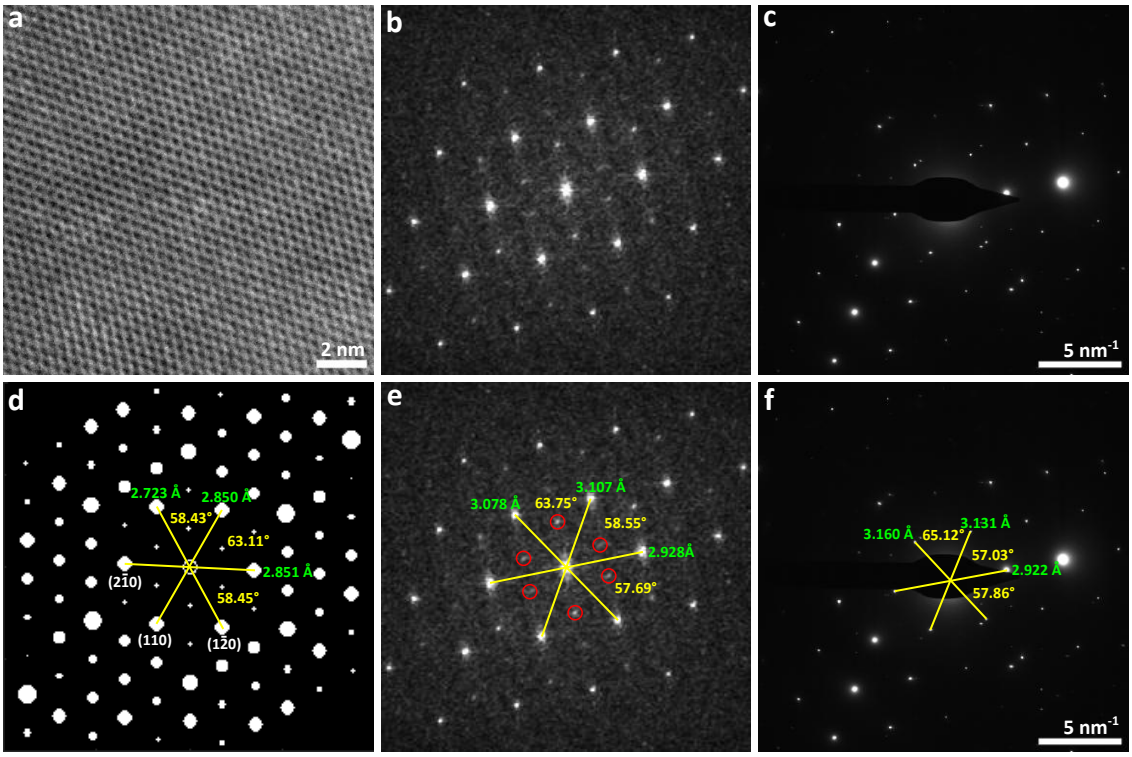

Figure 3.14: HRTEM image of t-MnO lattice (a) with corresponding FFT (b) and SAED pattern (c) taken from the same region. The angles and spot pattern match with the theoretical diffraction pattern (d).

diffraction pattern of t-MnO. The spots match in intensity and position, and the angles between the reflections are also close. However, the d-spacings of the experimental FFT and diffraction pattern are slightly larger than those of the theoretical diffraction pattern of the t-MnO phase. The d-spacings for the FFT and diffraction pattern were determined using a random sample consensus (RANSAC) algorithm featured in the CrysTBox software.[50] This algorithm fits the lattice parameters to all spots in the FFT or diffraction pattern and is therefore more accurate than determining the d-spacing of single spots. The unit cell parameters can be calculated from the $(1\bar{2}0)$ and $(2\bar{1}0)$ reflections in the FFT, using the following equation:

$$\frac{1}{d^2} = \frac{h}{a^2 \sin^2(\theta)} + \frac{k}{b^2 \sin^2(\theta)} - \frac{2hk\cos(\theta)}{ab\sin^2(\theta)}, \tag{3.1}$$

where d is the d-spacing of the reflection, a and b are the unit cell parameters, and θ is the angle between a and b. Assuming the angle between a and b is 118.5° as predicted,[6] solving the equations yields $a = 6.23$ Å and $b = 5.86$ Å, which is a 9.1% and 7.6% increase compared to the predicted unit cell parameters (see Table 3.1).

As is shown in Fig. 3.15, the theoretical diffraction patterns for h-MnO and Mn_3O_4 from certain zone-axes are similar to the theoretical diffraction pattern for t-MnO (see Fig. 3.14d). Most notable are the angles between the reflections, which are nearly identical for all three diffraction patterns. However, the t-MnO diffraction pattern has three different d-spacing values in the three directions, whereas the h-MnO and Mn_3O_4 diffraction patterns have two identical and one smaller d-spacing. The FFT and diffraction pattern of the nanosheets also have three different d-spacings, but the difference is small and can be attributed to experimental errors. The d-spacings shown in Fig. 3.14 are larger than the theoretical reflections of the t-MnO phase of which the lattice parameters are described in Table 3.1. However, the unit cell was calculated by DFT at 0 K, which is known for its underestimation of lattice parameters. Therefore, it is likely that the lattice parameters are not representative for the experimental

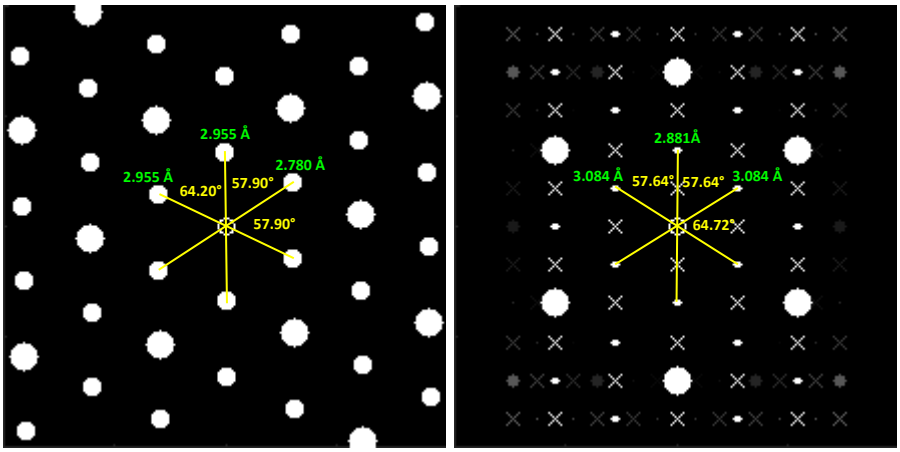

Figure 3.15: Theoretical diffraction patterns of h-MnO in the [001] zone-axis (left) and t-Mn_3O_4 in the $[10\frac{1}{2}]$ zone-axis (right). Crosses indicate forbidden reflections.

Table 3.3: d-spacings and angles for the diffraction patterns in Fig. 3.16.

DP	a (Å)	b (Å)	c (Å)	angle 1 (°)	angle 2 (°)	angle 3 (°)
P1 RT	4.89	5.04	5.05	58.88	58.97	62.15
P1 400 °C	4.91	5.12	5.14	58.34	58.66	63.00
P2 RT	2.57	2.81	3.20	49.48	59.83	70.69
P2 400 °C	2.57	2.81	3.20	49.35	59.76	70.90
P3 RT	2.52	2.83	3.20	48.88	58.16	72.96
P3 400 °C	2.57	2.89	3.24	49.25	58.11	72.64
P4 RT	2.51	2.55	3.02	49.46	64.29	66.26
P4 400 °C	2.51	2.57	3.02	49.57	63.68	66.74

lattice parameters. The most convincing reason for the nanosheet being t-MnO is the pattern of the diffraction spots. There are low-intensity spots at higher d-spacings in the t-MnO diffraction pattern, which are also present in the FFT of the nanosheet (see the red circles in Fig. 3.14e). These low-intensity reflections at high d-spacings are not present in the diffraction patterns of h-MnO and Mn_3O_4. Therefore, the FFT cannot be from the h-MnO or Mn_3O_4 phases, and must be from the t-MnO phase.

3.3.3. Nanosheet Heating

The as-synthesized MnO nanosheets were heated *in-situ* using the DENSsolutions heating holder in the TEM. The chip was prepared by dropcasting 2 μL of the nanosheet dispersion on a heating chip with holes. The material was heated to 400 °C in steps of 50 °C, and left for 10 min at every temperature before imaging.

At room temperature, the diffraction patterns from the four different areas indicated that the nanosheets had a hexagonal lattice (see Fig. 3.16). This was confirmed with HRTEM imaging except for the presence of one piece with a square lattice. The diffraction patterns did not change during the heating of the nanosheets, see Table 3.3. A lattice transformation did occur in the square piece, as shown in Fig. 3.17. The square lattice had lattice spacings of 2.51 Å and 2.76 Å in the two directions, which is, as before, not perfectly square and is not equivalent to the expected spacing of 2.22 Å derived from the c-MnO phase. This indicates that this lattice is restructuring as well. The FFTs (Fig. 3.17e-h) of the HRTEM images taken during the heating (Fig. 3.17a-d) of the square lattice show that that the angles between the reflections are no longer 90° from 350 °C. At 350 °C, both the reflections for the square and hexagonal lattices are present. The transformation is also clearly visible in the HRTEM images in

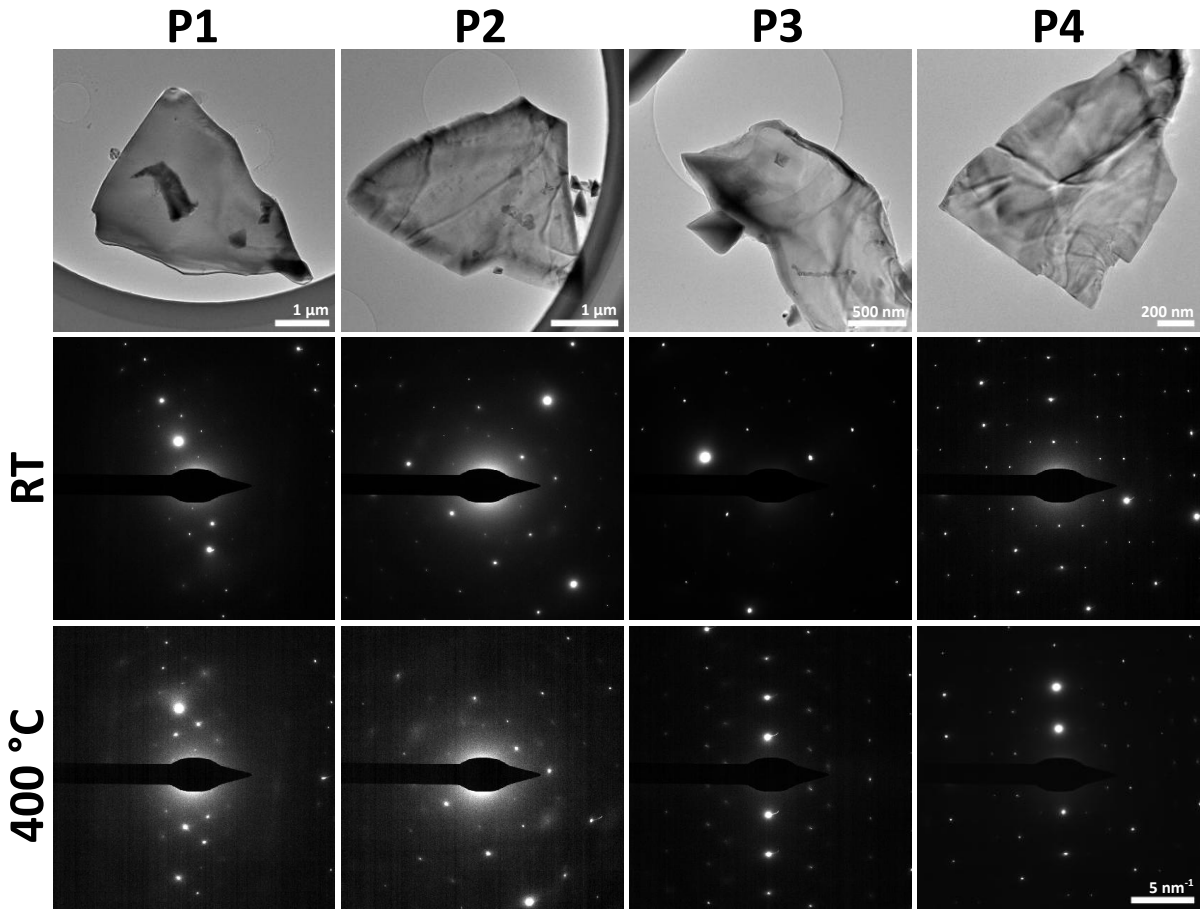

Figure 3.16: Sheets and corresponding SAED patterns taken at room temperature (RT) and 400 °C. The corresponding d-spacings are listen in Table 3.3.

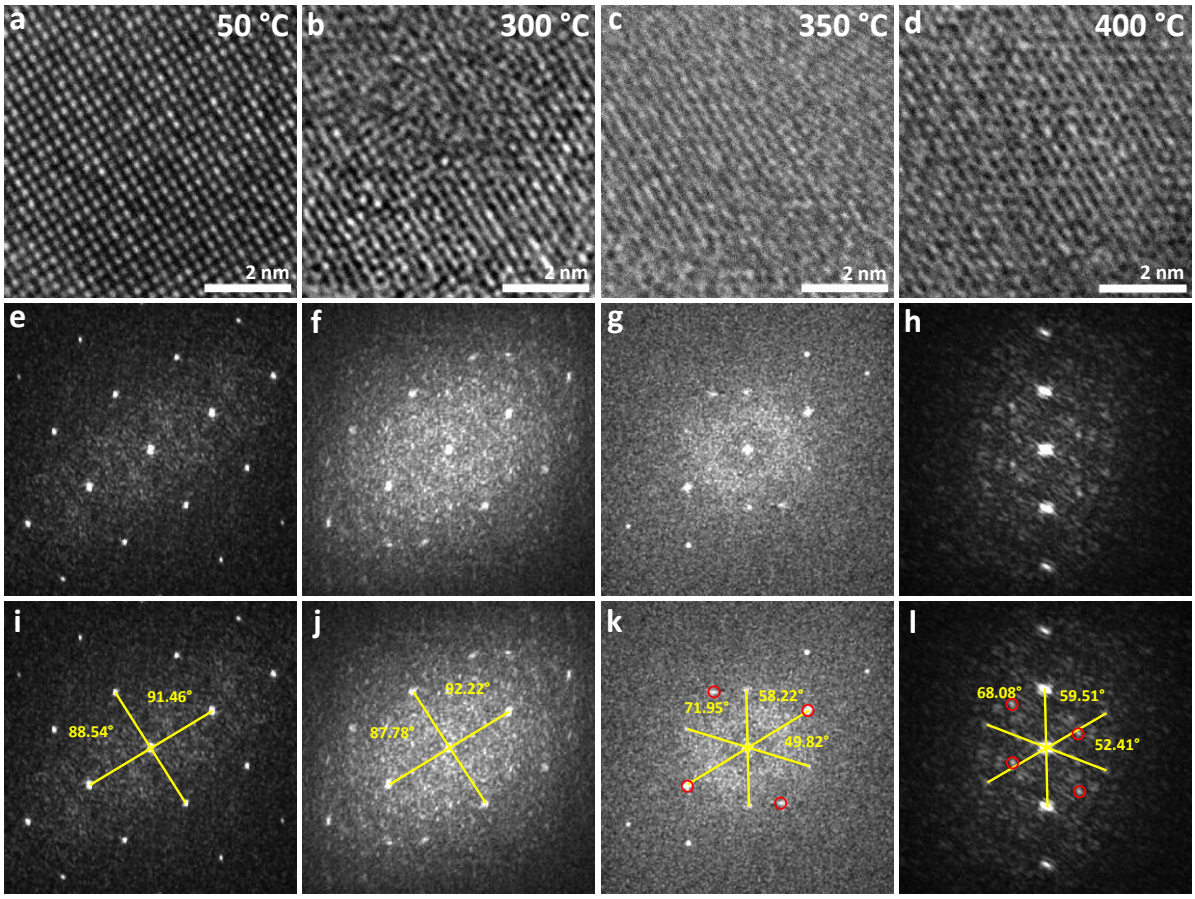

Figure 3.17: HRTEM (a-d) and respective FFT (e-l) images taken during the heating of MnO nanosheets indicating that a transformation from the square to a hexagonal lattice took place.

Fig. 3.17a-d, where it can be seen that there are already defects forming at 300 °C. At 350 °C, it was difficult to obtain lattice fringes, indicating less order in the lattice. At 400 °C, a hexagonal lattice can be observed in the HRTEM image (Fig. 3.17d). However, from both the HRTEM and FFT images, it is clear that the transformation was not yet complete and required more time or heat to fully transform into the hexagonal or trigonal lattice.

Because the diffraction patterns indicate that the nanosheets already had a hexagonal lattice at room temperature, the MnO transformed from a square lattice to a hexagonal lattice by itself in the time between the synthesis and the heating experiment, as was also argued in the previous section. Therefore, the square area studied during the heating experiment might have been different from the rest of the nanosheets in terms of thickness or stability and might therefore not be representative for the study of lattice transformations in the MnO nanosheets.

3.4. Conclusions

In conclusion, different types of manganese oxides were synthesized using a salt-templating method. When manganese(II) acetate was used as the precursor, the resulting material consisted of MnO nanoparticles embedded in amorphous carbon. Depending on the thickness of the amorphous carbon layer, the initial *c*-MnO nanoparticles oxidized spontaneously to *t*-Mn_3O_4 at room temperature. When heated *in-situ* in the TEM, the mix of MnO and Mn_3O_4 particles is reduced back to MnO. In one case, the mixture of phases was first fully oxidized to Mn_3O_4 before being reduced back to MnO, even though the heating was performed in vacuum. This is attributed to electron beam effects, which can accelerate the uptake of oxygen by the lattice or knockout Mn atoms, thereby changing the Mn to O ratio.

When manganese(II) chloride was used as the precursor, MnO sheets were synthesized. The thickness was determined with EELS and was found to be approximately 50 nm. The sheets exhibited square (*sq*) and trigonal (*t*) lattices at room temperature. Because the salt template is lattice directing, the sheets must be *sq*-MnO immediately after the synthesis. The presence of *t*-MnO at room temperature suggests that this lattice is energetically favored, resulting in a spontaneous transformation from a *sq* lattice to a *t* lattice. A heating experiment was also conducted on the MnO nanosheets. The diffraction patterns indicate that the sheets already had an *h* or *t* lattice, supporting the hypothesis that the *sq* lattice is energetically less favored. One area that was still *sq* transformed during heating to 400 °C.

Overall, this section demonstrates the interesting behavior of manganese oxides. It has already been established that manganese oxides can be applied in battery technology for the improvement of Li-ion batteries. For this application, it is important to understand the stability and morphological changes of manganese oxides, as described in this study. Moreover, the trigonal lattice, as predicted by DFT calculations [6] was experimentally verified for the first time. This opens opportunities for further research on TMOs and their lattices. Specifically related to MnO are the interesting spin configurations predicted in hexagonal MnO lattices, which could open a playground for fundamental physics research and should be investigated in more detail for the trigonal lattice as well.

4. Gadolinium Oxide Nanocrystals

In this section, the results for the gadolinium oxide nanofoams are described. The aim of this project was to characterize the porosity of the gadolinium oxide nanofoam, and to study the formation process of the material during combustion synthesis. First, the bulk synthesized material is characterized by TEM, physisorption, and electron tomography. Then the heating experiments on the gadolinium gel and gadolinium precursor are described, and their properties are compared to the bulk material.

4.1. Combustion Synthesis Theory

For the synthesis of gadolinium oxide nanocrystals, combustion synthesis is used. Combustion synthesis is a synthesis method in which a metal compound and a fuel are combined and heated. At relatively low temperatures (compared to for instance solid state synthesis), the mixture will ignite and a highly exothermic reaction takes place in which a metal oxide and a large amount of gas are formed. Due to the gas formation during the reaction, the final product will be very porous and can be classified as a metal foam.

The type of reaction that happens during combustion synthesis is a redox reaction. It is therefore convenient if the metal compound itself is an oxidizer. During the combustion synthesis process, the fuel that is present is oxidized (burned) which causes the temperature to rise considerably. For the metal compound, frequently metal nitrate hydrates ($Me^v(NO_3)_v \cdot nH_2O$) are used. The most used fuels are glycine ($C_2H_5NO_2$) and urea (CH_4N_2O). [16]

For the production of gadolinium oxide, gadolinium nitrate hexahydrate ($Gd(NO_3)_3 \cdot 6H_2O$) is used as the oxidizing metal compound and glycine is added as the fuel. The components are dissolved in water and slightly heated to obtain a gel-type medium. This particular kind of combustion synthesis is called sol-gel combustion synthesis. An advantage of the gelling is that the solution becomes more viscous, which allows for the impregnation of the solution into various supports, which can be beneficial for catalytic applications. The gel is then heated in a muffle furnace. The proposed reaction equation is [34] [1]:

$$6Gd(NO_3)_3 \cdot 6H_2O + 10C_2H_5NO_2 \rightarrow 3Gd_2O_3 + 14N_2 + 20CO_2 + 27H_2O. \tag{4.1}$$

An important factor to consider in combustion synthesis is the cooling rate. The cooling rate determines whether the obtained product will be the equilibrium product or a metastable phase. Since the cooling rate is generally very fast for combustion synthesis, interesting structures are often observed. For slow cooling rates, the product will be at a higher temperature for a longer time which gives it the chance to relax to the equilibrium structure. When the cooling rate is fast and the product has not enough time to equilibrate, the product can be frozen in a nonequilibrium phase. [62, 63]

Another factor that influences the reaction is the amount of fuel that is added. For high fuel-to-oxidizer ratios, the amount of gas products is higher causing more porous structures to appear. Also the combustion temperature changes with the ratio of fuel to oxidizer, which could also influence the particle size that is obtained. Moreover, the amount of water also influences the combustion temperature. An example of the dependence of the combustion temperature on the fuel-to-oxidizer ratio and the amount of water can be seen in figure 4.1, where the combustion synthesis of iron nitrate and glycine was studied [64].

The main advantage of combustion synthesis over other synthesis methods is that it is self-propagating, meaning that there is less energy consumption. It also has a short reaction time. Moreover, the resulting

[1] Recent unpublished work by the authors actually indicates that the formed gases are all kinds of combinations of C, O, and N. This is probably due to the high temperature, which enables non-equilibrium products to form. This reaction indicates the thermodynamic most likely reaction route, but note that it is apparently not representative for the actual experiment.

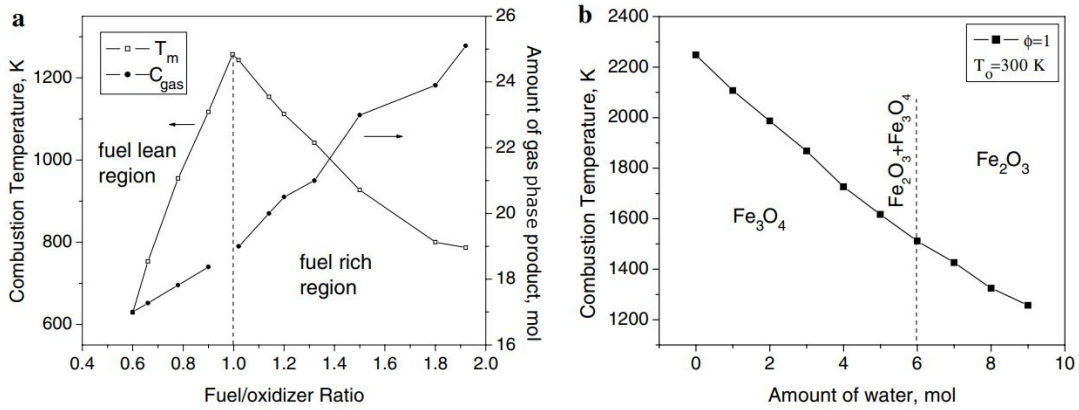

Figure 4.1: (a) Dependence of combustion temperature and amount of gas product on the fuel to oxidizer ratio. (b) Dependence of combustion temperature on the amount of water. Obtained from ref. [64].

material is highly porous due to the release of gaseous products, which is obtained without the need for a template. However, the downside of combustion synthesis is that the reaction is hard to control and highly dependent on reaction parameters due to its non-equilibrium nature.

In comparison to the combustion synthesis method, we can look at the thermal decomposition of gadolinium nitrate, which has been studied by Fukuda *et al.* [65]. They found that the thermal decomposition of gadolinium nitrate happens in a 3 step reaction. After dehydration of the salt, $GdO(NO_3)$ is formed in the first step, which occurs around 400 °C. The second step involves the formation of a gadolinium compound which could not be identified with x-ray diffraction (XRD) but is probably $Gd_4O_5(NO_3)_3$. Finally, Gd_2O_3 is formed in the third step at around 600 °C. From the decomposition of gadolinium nitrate, it can be concluded that the high temperatures that are achieved in the combustion synthesis are not necessary for the formation of crystalline gadolinium oxide.

4.2. Experimental

Combustion synthesis: A gel containing $Gd(NO_3)_3{\cdot}6H_2O$ (99.9%, Acros Organics) and glycine (analytical grade, Penta s.r.o.) in a 1:1 molar ratio was prepared by dissolving the components in water and drying the solution at 120 °C. Some of the gel was then calcinated in an oven heated to 600 °C with a ramping rate of 20 °C/min for 1 h, after which a white powder was obtained.

Physisorption: The specific surface area (S_{BET}) and pore size distribution of the sample were determined by N_2 physisorption at 77 K using a Micromeritics TriStar II Plus. Prior to measuring, the sample was dried for at least 12 hours at 300 °C under N_2 flow. The S_{BET} was determined using the Brunauer, Emmett, and Teller (BET) method [66], and the pore size distribution was determined using the Barrett-Joyner-Halenda (BJH) method [67].

In-situ TEM: All TEM investigations were carried out using a TFS Talos F200X electron microscope. For the heating experiments, the gadolinium precursor gel was carefully applied to a DENSsolutions MEMS heating chip, making sure to deposit only a thin layer of gel. In some cases, the gel was diluted with water to make it less viscous. The chip was then inserted in the DENSsolutions heating holder. For the *in-situ* experiment, the gel was inserted into the TEM and heated with 100 °C increments, where it was imaged at every temperature. For the *ex-situ* experiment where the gel was heated to 600 °C, also 100 °C increments were used to compare with the *in-situ* experiment. For the *ex-situ* experiment where the gel was heated up to 900 °C, a ramping rate of 20 °C/min was used in accordance with the bulk gel-combustion synthesis.

Electron tomography: The tilt series were recorded on the same microscope using a tomography holder, where the sample was tilted with 1° increments. The grids were decorated with gold nanoparticles to

serve as markers, which later turned out to be unnecessary due to the high contrast of the heavy gadolinium. The tomographic reconstructions were made with Tomviz (`www.tomviz.org`). The 2048x2048 pixel images were first binned to 512x512 pixel images. The images were then aligned by cross-correlation, and the tilt axis was aligned by first applying an automatic rotation alignment and then an automatic shift alignment. After aligning the images, the images were cropped to contain only the region of interest. Finally, the reconstruction was made using the weighted back projection (WBP) algorithm [43], where the Fourier weighting filter was set to ramp and the projection interpolation method to cubic. After reconstruction, the material was segmented by applying a threshold. The surface was smoothed by applying Gaussian blurring with a sigma value of 2.0 and the volume was sliced to make a cross-section. The final visualizations include both the volume and the contours of the segmented areas.

4.3. Results and Discussion

The initial transparent precursor solution composed of $Gd(NO_3)_3{\cdot}6H_2O$ and glycine is shown in Fig. 4.2a. After the gel-combustion synthesis, the resulting material is a fine, white powder presented in Fig. 4.2b. Detailed TEM investigations were conducted to obtain more information about the textural features of the Gd_2O_3 nanofoam. Fig. 4.2c shows a single cylindrical piece of the nanofoam, showing a highly porous texture consisting of spherical pores with a wide size distribution. It can also be seen that the texture is presented as one whole and not composed of agglomerated particles as is often seen in combustion synthesis, and it is in apparent contradiction to previous findings on that particular material. This could be caused by the relatively low temperature that is observed when glycine is used as fuel. A higher combustion temperature generally leads to a higher degree of agglomeration [68], which can be obtained with different fuels [16]. The inset of Fig. 4.2c shows a typical diffraction pattern (DP) of the material that can be indexed as cubic Gd_2O_3 as shown in Fig. B.1. The very sharp rings also show that the material is crystalline. Inspection at larger magnification shows that the pores are bounded by nanocrystalline walls as shown in Fig. 4.2d and vary in thickness from 4 to 10 nm. The entirety of the nanofoam is crystalline as is clear from the DP in Figure 1c and the high-resolution TEM images presented in Fig. 4.2e and correspond to the cubic phase of Gd_2O_3. The prepared Gd_2O_3 nanofoam is composed of different morphologies that vary from cylindrical and spherical (Fig. B.2a and b), to irregular (Fig. B.2c) textures as can be seen in Appendix B. The energy dispersive X-ray spectroscopy (EDS) mapping of the material presented in Figure S3 shows the presence of Gd and O, and the absence of N, indicating the successful conversion of the $Gd(NO_3)_3$. The combustion synthesis of the gadolinium gel, therefore, yields highly crystalline but porous Gd_2O_3.

The Gd_2O_3 sample was analyzed using N_2 physisorption. The isotherm and pore size distribution can be seen in Fig. 4.3. The surface area S_{BET} was determined to be 67 m^2/g for this sample, which is high compared to other combustion synthesized nanofoams of similar composition using glycine as fuel (e. g. 10 – 34 m^2/g in CeO_2, up to 7 m^2/g in Gd_2O_3-Y_2O_3:Ce, 5 – 25 m^2/g in Lu_2O_3:Eu^{3+})[69–72]. With the value for the surface area, we can calculate the Sauter diameter of the particles according to:

$$d_{BET} = 6\rho \cdot S_{BET}, \tag{4.2}$$

where ρ is the density of Gd_2O_3, which is $7.41 \cdot 10^6$ g/m^3 [73]. This gives a value of 12 nm for the Sauter diameter, which corresponds well with the 10 nm crystallite size that was determined with the Scherrer formula from x-ray diffraction (XRD) measurements in previous work on this material [34]. The ratio between the particle sizes derived from the S_{BET} and the XRD measurements gives an indication of the degree of agglomeration of the particles. The low ratio of 1.2, in this case, supports the TEM observation that the material in fact does not consist of agglomerated particles. The BJH analysis shows that there is a narrow distribution of pores around 2 nm, a distribution of mesopores around 10 nm, and a wide distribution of macropores. The total volume of the 2 nm large pores is small (blue line in Figure 2), but the total pore area of these pores is actually high (red line in Fig. 4.3), which means that there is a large

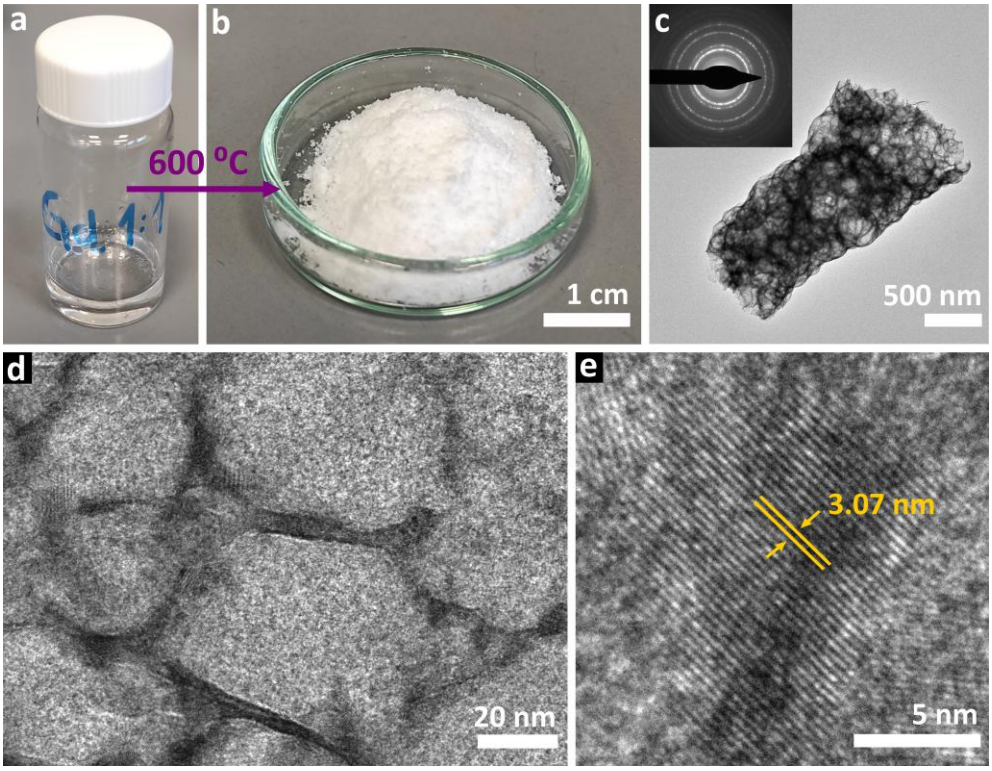

Figure 4.2: (a,b) Photographs showing the precursor Gd gel (a) and the resulting Gd_2O_3 powder after heating (b). (c-e) Transmission electron microscopy (TEM) images at different magnifications; (c) Bright-field TEM image of a grain of material from (b); the inset shows the corresponding electron diffraction pattern, indicating that the material is crystalline. d) Higher magnification TEM image showing the pore walls. (e) High-resolution TEM image where atomic lattice fringes also show the high crystallinity of the material.

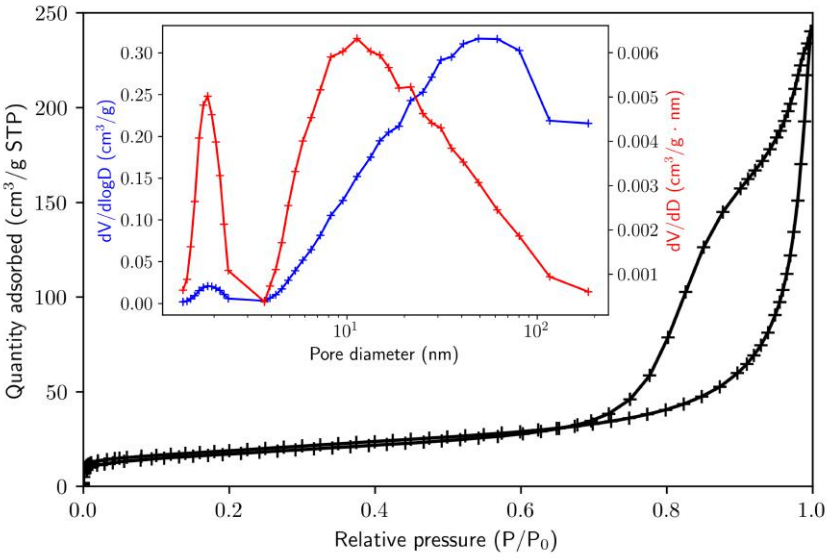

Figure 4.3: N_2 physisorption isotherms of the Gd_2O_3 with Barrett-Joyner-Halenda (BJH) pore size distributions derived from the adsorption branch shown in the inset.

number of these smaller pores.

A tilt series of a typical larger piece of the Gd_2O_3 material was recorded with regular bright-field TEM and with high-angle annular dark field scanning TEM (HAADF-STEM), see Fig. 4.4a and 4.4b respectively. Experimental details can be found in the Methods section. From these tilt series, a 3D model of the material was reconstructed using tomography, see Fig. 4.4c. The tomographic reconstruction was made using the WBP algorithm since the simultaneous iterative reconstruction technique (SIRT)[44] was found to result in a worse reconstruction. The TEM and STEM recorded tilt series result in nearly identical 3D reconstructions. The 3D reconstructions shown in Figs. 4.4 and 4.5 are all derived from the STEM tilt series.

The surface of the 3D reconstruction (Fig. 4.4c) shows pores on the surface of the material most probably formed during the emission of waste gases from the inside of the structure during the material-forming reactions. Fig. 4.4c also shows the cross-section of the 3D reconstruction, where the complex inner pore structure of the material can be seen. The pores are mainly spherical, further suggesting their generation during the reaction, interconnected, and have a wide size distribution. Due to the low magnification that was used to image this larger piece of Gd_2O_3, fewer details can be distinguished in the reconstruction. Therefore, a smaller piece was also analyzed, which was obtained after gently grinding the Gd_2O_3 powder. Fig. 4.5 shows HAADF-STEM images and the tomographic reconstruction of the smaller Gd_2O_3 grain. The surface of the reconstructed volume shows pores in the wall of the material indicated by red arrows in Fig. 4.5d. Because of the higher magnification, it is now also possible to see smaller pores with sizes as small as 2 or 3 nm. Fig. 4.5c highlights dark areas in the HAADF-STEM image that likely correspond to interconnections of pores within pore walls. The reconstructed cross-section of the area enclosed by the blue dashed lines is shown in Fig. 4.5f, showing interconnecting pores depicted by the yellow arrows. From these results, we can infer that the Gd_2O_3 material made with combustion synthesis has an intricate network of interconnected pores with a wide size distribution.

In order investigate the mechanism of the gel-combustion reaction more precisely, heating experiments were performed on the gel, where a small amount of gel was applied on a TEM heating chip and heated *in-situ* as well as *ex-situ* (in ambient air) for comparison. An overview of typical TEM observations seen during the heating experiments and the corresponding electron DPs can be seen in Fig. 4.6.

The gel was first heated *in-situ* to 600 °C with 100 °C increments. An overview of one of the windows

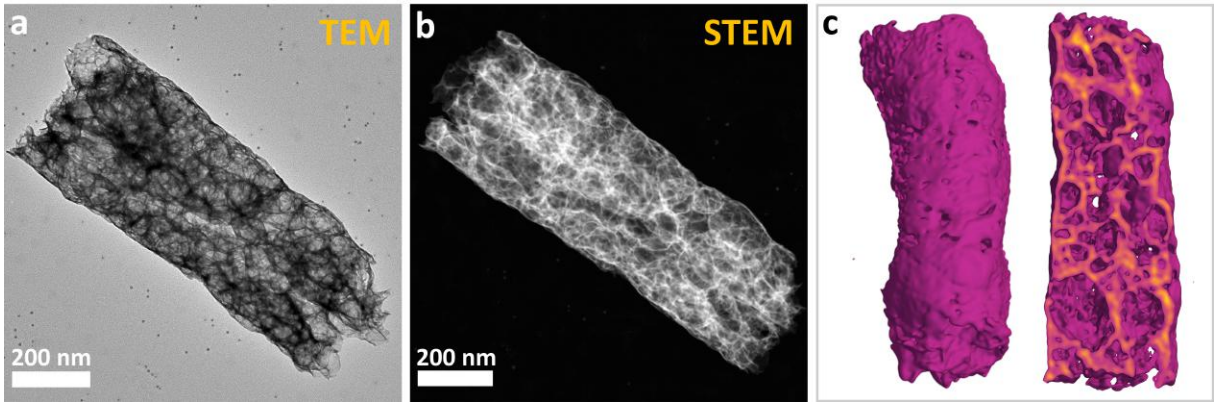

Figure 4.4: TEM (a) and HAADF-STEM (b) image of porous Gd_2O_3 obtained by combustion synthesis. The dots in the TEM image are gold nanoparticles, which are hardly visible in the STEM image because of the high contrast of the gadolinium. The surface and a cross-section of the corresponding 3D model reconstructed with tomography is shown in (c), showing surface pores and spherical inner pores.

on the heating chip (the windows are thin SiN_x membranes onto which the gel was applied) with a corresponding DP is shown in Fig. 4.6a. The most prominent feature that stands out is the large-scale porosity of the material. However, the DP (indexed in Fig. B.4) indicates that here cubic GdO (space group $F\bar{4}3m$) has been formed and not the expected Gd_2O_3. From the images taken during the heating of the gel, it becomes apparent that the structures start to become porous from 100 °C onward, see Fig. B.5. Besides the large-scale porosity that can be seen in the overview of the window, the higher magnification images reveal that there is also small-scale porosity in the structure. From the high-resolution TEM (HRTEM) image in 4.7a, it can be seen that there are small pores with a size of around 2-3 nm, and bigger pores with a size of around 10-15 nm. This corresponds well with the pore size distribution that was obtained from N_2 physisorption on the bulk combustion sample. The high crystallinity of the material can also be seen from the lattice fringes that are present in the HRTEM image of Fig. 4.6e. However, it was also observed that the electron beam could induce crystallization of the material. The HRTEM images may, therefore, not be representative for the rest of the material. From this *in-situ* heating experiment, we can conclude that the material develops its porosity at low temperatures and that the crystallization likely develops at higher temperatures or even during annealing after the combustion is complete. The formation of GdO instead of Gd_2O_3 could be caused by the lower temperature that is reached on this small-scale (exothermic heat from the reaction escapes more easily from the sample). Apart from less efficient annealing in the vacuum conditions of the microscope limiting the accessibility of atmospheric oxygen for the reaction can explain the lower oxidation degree of the resulting material. The sample was imaged again after 6 weeks and was found to have transformed into an amorphous state, and the porosity of the sample was lost, see Fig. B.6. In this post-inspection experiment, the electron beam had a large effect on the amorphous sample, where short electron irradiation caused the structure to become porous again.

Since it was hypothesized that the vacuum conditions in the TEM might prevent the oxidation of the gadolinium precursor to Gd_2O_3, the gel was also heated *ex-situ* under atmospheric conditions. In the first *ex-situ* experiment, the gel was heated to 600 °C like in the *in-situ* experiment. However, this resulted in an amorphous structure as can be seen in Fig. 4.6b'. As such, the gel was heated to 900 °C in a second *ex-situ* experiment. There the successful oxidation to Gd_2O_3 was indeed observed (Fig. 4.6c'). Notably, this time the characteristic large-scale porosity seen in the *in-situ* experiment was not observed. This could be caused by the absence of vacuum in the ex-situ experiments. The smaller scale porosity, however, remained, which can be seen in the HRTEM image in Fig. 4.7b. The crystallinity of the material, which was already indicated by the sharp rings in the DP, is also reflected in the lattice

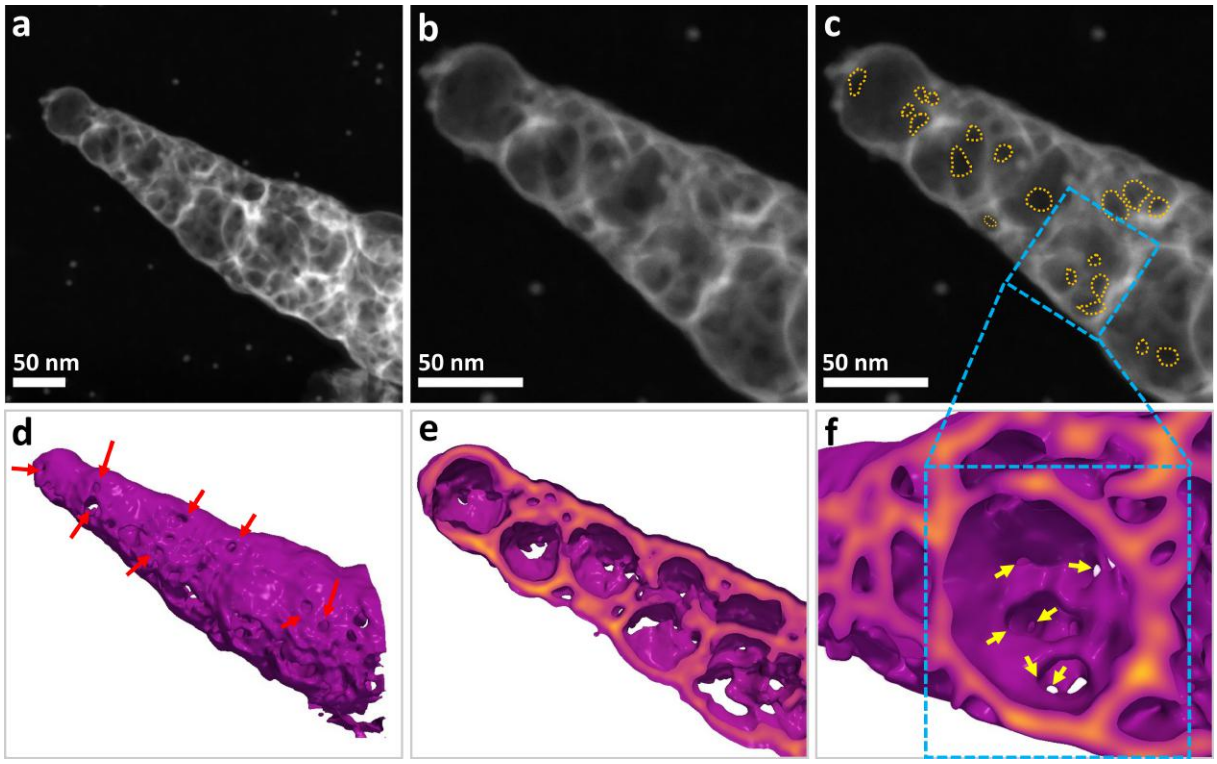

Figure 4.5: HAADF-STEM images of a small piece of porous Gd_2O_3 (a-c) with corresponding tomographic reconstruction (d-f). The area indicated in (a) is enlarged in (b) and dark spots are highlighted in (c). The surface of the particle is shown in (d) with red arrows indicating pores in the wall of the particle. A cross-section of the reconstructed particle is shown in (e) and a magnified pore with smaller interconnecting pores indicated by yellow arrows can be seen in (f).

fringes that can be seen in the HRTEM image in Fig. 4.6f. The samples imaged after 6 and 7 weeks, respectively, can be seen in Fig. B.6. Unlike the sample from the *in-situ* heating experiment, the samples from the *ex-situ* experiments remained stable. The transformation of the *in-situ* sample is therefore likely related to the instability of the oxygen-deficient GdO phase.

In comparison to the bulk synthesis, the small-scale heating experiments require a higher temperature to obtain the same result. This discrepancy can be explained by the overall amount of sample. The large amount of material that is being heated in the bulk combustion synthesis allows the temperature of the material to increase abruptly during the highly exothermic redox reaction. On the small-scale of these heating experiments, the higher dissipation of reaction energy inhibits the temperature increase during the reaction. This leaves the question of whether combustion took place in the small-scale heating experiments, or if the observed phenomena were only mere decomposition of the starting compounds. According to the literature, the expected formation of Gd_2O_3 during the decomposition of $Gd(NO_3)_3{\cdot}6H_2O$ is between 550 °C and 700 °C under He atmosphere [65]. To investigate this further, a 1.4 mM solution of $Gd(NO_3)_3{\cdot}6H_2O$ in ethanol was drop-casted on a heating chip and heated *in-situ* to 900 °C with 100 °C increments. This sample also showed porosity from 100 °C (Fig. B.7), which is attributed to the evaporation of the water that is contained in the gadolinium nitrate. An overview of one of the windows and a corresponding DP can be seen in Fig. 4.6d and 4.6d' respectively. Note that the DP was taken at 900 °C and, therefore, displays a larger lattice than the other DPs taken at room temperature. Although some porosity was present after heating to 900 °C, it is less than seen in the heating experiments of the gel. This becomes clear, especially from the HRTEM images, where the characteristic 2 to 20 nm large pores are absent, see Fig. B.7. Although the absence of glycine in this experiment reduces the amount of gas that is created compared to a possible decomposition of the complete gel, it is more likely that there

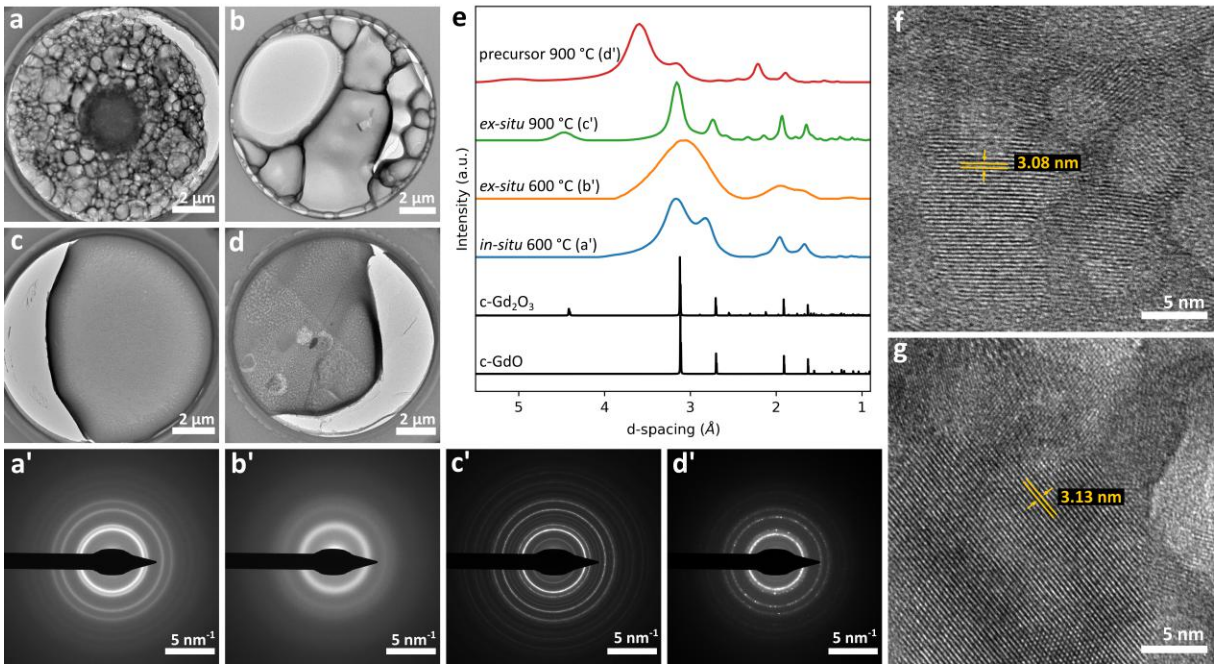

Figure 4.6: Overview of TEM images displaying typical viewing windows with GdO_x specimen on the heating chip recorded after *in-situ* heating of the Gd gel to a temperature of 600 °C (a), *ex-situ* heating of the Gd gel to 600 °C (b), *ex-situ* heating of the Gd gel to 900 °C (c), in-situ heating of the Gd precursor to 900 °C (d) with corresponding diffraction patterns (a‘, b’, c’, d’, respectively), intensity profiles of the diffraction patterns and GdO and Gd_2O_3 phases (e), and high resolution TEM images showing atomic lattices after heating *in-situ* to 600 °C (f) and after heating *ex-situ* to 900 °C (g). Indexed diffraction patterns can be seen in Fig. B.4.

is indeed a small-scale combustion reaction taking place in the heating experiments of the complete gel. This hypothesis is further supported by the fact that this reaction is highly exothermic and therefore more favorable.

4.4. Conclusion

Highly porous crystalline gadolinium oxide was successfully synthesized, without the use of a template, by combustion synthesis of a gel consisting of gadolinium nitrate and glycine. The surface area and pore size distribution of the material were assessed by nitrogen physisorption. The S_{BET} of the material was determined to be 67 m^2/g and the pore size distribution shows the presence of pores in three size ranges. Furthermore, a 3D reconstruction of the nanoporous structure was made using electron tomography employing the weighted back projection algorithm, of which cross-sections reveal the internal nanostructural details of the material. The combustion synthesized Gd_2O_3 has an intricate interconnected pore network consisting of spherical pores with size ranges varying from 2–3 nm to tens of nanometers. The nitrogen physisorption results and the electron tomography results were found to be in good agreement. Also, small-scale heating experiments of the gel were conducted to further investigate the combustion mechanism of pore formation. The small-scale heating experiments showed a different porosity of the material in comparison to that of the bulk combustion material. Moreover, a higher temperature is needed to form Gd_2O_3 in the small-scale heating experiments, which is probably due to the fast cooling of the material on this scale. The decomposition of the gadolinium nitrate precursor indicates that a combustion reaction is happening as well in the small-scale heating experiments, rather than just a decomposition of the gel components. The results indicate that the porosity of the material can be tuned by controlling the experimental conditions during the combustion reaction, such as the scale of the synthesis and the

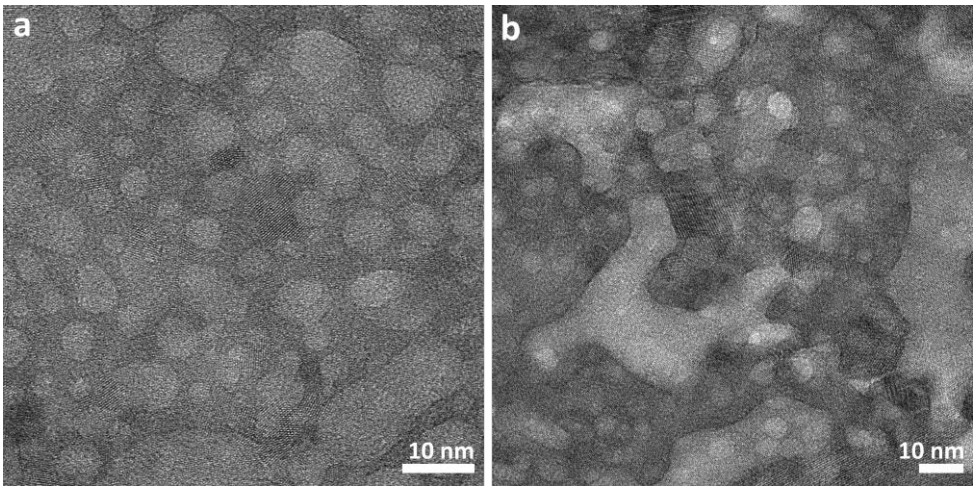

Figure 4.7: HRTEM images of the gadolinium gel when heated *in-situ* to 600 °C (a) and heated *ex-situ* to 900 °C (b), showing small-scale porosity.

atmosphere in which the gel is heated. In conclusion, gel-combustion synthesis has a great potential to yield crystalline gadolinium oxide nanofoams with a wide range of nanoporous structures that still need to be mapped out.

5. Summary & Outlook

In this thesis, two novel nanomaterials were investigated: (1) Manganese oxide nanostructures and (2) Gd_2O_3 nanofoam. Electron microscopy was used to obtain insights into the structural properties of both nanomaterial systems, and *in-situ* TEM was used to study their formation mechanism and thermal stability.

Manganese is an interesting element belonging to the group of transition metals and has a partially filled 3d shell. Manganese oxides can have many different phases and stoichiometries, and can transform from one to the other under ambient conditions after synthesis, or under the influence of an electron beam or by heating, as shown in this work. This work aimed to confirm the theoretical prediction that square MnO nanosheets transform to trigonal nanosheets when heated. To prove this, first square MnO nanosheets had to be synthesized, which had only been achieved before by using a salt-templating method. However, following the described method resulted in MnO_x nanoparticles on amorphous carbon layers, which were nonetheless interesting. The particles were cubic MnO directly after the synthesis but partly transformed to trigonal Mn_3O_4 over time. When this MnO/Mn_3O_4 was heated *in-situ* in the TEM, it was fully reduced to MnO, but transformed back to Mn_3O_4 when aged at ambient temperature. Moreover, it was shown that, besides the reversible MnO to Mn_3O_4 transition, the oxidation of the sample was dependent on the thickness of the amorphous carbon layer around the particles. When the carbon layer is sufficiently thick, it can fully prevent oxidation, thereby stabilizing the MnO phase. It was also observed that the MnO could oxidize to Mn_3O_4 in the vacuum of the TEM. This is probably due to electron beam effects, but the exact mechanisms should be investigated in more detail in future experiments. By heating the manganese(II) acetate precursor that was used for the salt-templating synthesis, it was shown that the growth of the amorphous layer around the MnO particles is inherent to the presence of the organic precursor and prevents the formation of MnO films, explaining why sheets could not be obtained in this synthesis.

The MnO nanoparticle arrays studied in this thesis can be applied in battery technology. Moreover, the reversible Mn_3O_4 to MnO reduction indicates that Mn_3O_4 might be used as a reusable oxidizer, which can be recovered by simply letting the reduced Mn_3O_4 take up oxygen from the atmosphere at ambient conditions.

When manganese(II) chloride was used as the precursor instead of manganese(II) acetate, and heated for 3h instead of 1h, MnO sheets could be obtained. The sheets were found to have both square and trigonal lattices at room temperature. Since the KCl template that was used is a lattice directing agent for *sq*-MnO, the MnO lattice is likely square right after synthesis. Therefore, the square lattice must have transformed into a trigonal lattice already at room temperature. A lattice transformation has been observed during the *in-situ* heating of a *sq*-MnO nanosheet, but the majority of the MnO nanosheets already had a hexagonal lattice at room temperature. It has also been argued that the experimentally found phase is indeed the t-MnO phase as described by van Gog *et al.* [6], thereby confirming its existence and stability.

This research has opened up opportunities for further research in the field of TMOs. Besides *t*-MnO, the existence of *t*-CrO and *t*-VO was also predicted. An obvious continuation of this research would be to experimentally find these phases as well. Moreover, the wide spectrum of fundamental physics that was predicted for the hexagonal MnO lattice (see Section 1) should be investigated.

In the second part of this thesis, the synthesis of gadolinium oxide by gel-combustion synthesis was investigated, and the bulk-synthesized material was characterized by TEM, physisorption, and tomography. The physisorption indicated that the material has a surface area of 67 m^2/g, which is high compared to similar materials synthesized with combustion synthesis. With electron tomography, a 3D model of the Gd_2O_3 structure was obtained, revealing the intricate pore network of the material. With *in-situ* TEM heating, the formation of Gd_2O_3 from the gel has been investigated. From the heating experiments, it becomes apparent that the morphology of the material is dependent on the experimental conditions,

which gives the possibility to tune the pore size of the material.

This research shows the potential of gel-combustion synthesis for the formation of porous metal oxides. The *in-situ* heating experiments showed that the morphology of the material is dependent on the experimental conditions, which should be mapped out in future investigations. For instance, the bulk synthesis can be carried out under inert atmospheres to compare with the heating experiments, different fuels and fuel-to-metal nitrate ratios can be used to change the obtained temperature, and different amounts of gel can be combusted to study the effects of the cooling rate of the material. Moreover, gadolinium oxide can be used in catalytic and water purification applications. The catalytic activity of the gel-combustion synthesized Gd_2O_3 can be investigated in future research, and the water purification capabilities of the produced nanofoam should be investigated by, for instance, studying the degradation of common water pollutants in porous Gd_2O_3. Finally, other metal oxides can be synthesized with the gel-combustion method, and the properties of the resulting materials can be compared with the product from other synthesis methods to further reveal the potential of this method.

Overall, this work shows the capability and versatility of electron microscopy. It can be used to image nanomaterials on scales ranging from micrometers to Ångströms, where individual atoms can be images. The many detectors allow for spectroscopic analysis, and combined with computer algorithms, electron microscopy images can even be used to make 3D models of the material under investigation. In addition, heating inside the TEM is made possible by a specialized heating holder, allowing for real-time viewing of thermal influences on the sample. This thesis only shows a small part of the possibilities of the TEM. Many more *in-situ* holders and additions are available to make it even more powerful. Even though TEM is a relatively old technique, it is constantly being improved and will likely continue to push the boundaries of physics and chemistry.

Bibliography

[1] K. S. Novoselov, A. K. Geim, S. V. Morozov, D. Jiang, Y. Zhang, S. V. Dubonos, I. V. Grigorieva, and A. A. Firsov, "Electric field in atomically thin carbon films", Science **306**, 666–669 (2004).

[2] H. Q. Ta, R. G. Mendes, Y. Liu, X. Yang, J. Luo, A. Bachmatiuk, T. Gemming, M. Zeng, L. Fu, L. Liu, and M. H. Rümmeli, "In situ fabrication of freestanding single-atom-thick 2d metal/metallene and 2d metal/ metallene oxide membranes: recent developments", Advanced Science **8**, 2100619 (2021).

[3] P. Ares and K. S. Novoselov, "Recent advances in graphene and other 2d materials", Nano Materials Science **4**, 3–9 (2022).

[4] D. Geng, H. Y. Yang, D. C. Geng, and Y. Yang, "Recent advances in growth of novel 2d materials: beyond graphene and transition metal dichalcogenides", Advanced Materials **30**, 1800865 (2018).

[5] X. Chen, S. N. Hosseini, and M. A. V. Huis, "Heating-induced transformation of anatase tio 2 nanorods into rock-salt tio nanoparticles: implications for photocatalytic and gas-sensing applications", ACS Applied Nano Materials **5**, 1600–1606 (2022).

[6] H. van Gog, W. F. Li, C. Fang, R. S. Koster, M. Dijkstra, and M. van Huis, "Thermal stability and electronic and magnetic properties of atomically thin 2D transition metal oxides", npj 2D Materials and Applications **3**, 1–12 (2019).

[7] E. Kan, M. Li, S. Hu, C. Xiao, H. Xiang, and K. Deng, "Two-dimensional hexagonal transition-metal oxide for spintronics", Journal of Physical Chemistry Letters **4**, 1120–1125 (2013).

[8] B. Y. Zhang, K. Xu, Q. Yao, A. Jannat, G. Ren, M. R. Field, X. Wen, C. Zhou, A. Zavabeti, and J. Z. Ou, "Hexagonal metal oxide monolayers derived from the metal–gas interface", Nature Materials **20**, 1073–1078 (2021).

[9] X. L. Wang, "Dirac spin-gapless semiconductors: promising platforms for massless and dissipationless spintronics and new (quantum) anomalous spin Hall effects", National Science Review **4**, 252–257 (2017).

[10] S. Vishveshwara, "A glimpse of quantum phenomena in optical lattices", Philosophical Transactions of the Royal Society A: Mathematical, Physical and Engineering Sciences **370**, 2916–2929 (2012).

[11] X. Q. Yu, Y. He, J. P. Sun, K. Tang, H. Li, L. Q. Chen, and X. J. Huang, "Nanocrystalline MnO thin film anode for lithium ion batteries with low overpotential", Electrochemistry Communications **11**, 791–794 (2009).

[12] L. Chen, X. Guo, W. Lu, M. Chen, Q. Li, H. Xue, and H. Pang, *Manganese monoxide-based materials for advanced batteries*, Aug. 2018.

[13] Y. Zou, W. Zhang, N. Chen, S. Chen, W. Xu, R. Cai, C. L. Brown, D. Yang, and X. Yao, "Generating oxygen vacancies in MnO hexagonal sheets for ultralong life lithium storage with high capacity", ACS Nano **13**, 2062–2071 (2019).

[14] Y. Xiao and M. Cao, "Carbon-Anchored MnO Nanosheets as an Anode for High-Rate and Long-Life Lithium-Ion Batteries", ACS Applied Materials and Interfaces **7**, 12840–12849 (2015).

[15] X. Xiao, H. Song, S. Lin, Y. Zhou, X. Zhan, Z. Hu, Q. Zhang, J. Sun, B. Yang, T. Li, L. Jiao, J. Zhou, J. Tang, and Y. Gogotsi, "Scalable salt-templated synthesis of two-dimensional transition metal oxides", Nature Communications **7**, 1–8 (2016).

[16] A. Varma, A. S. Mukasyan, A. S. Rogachev, and K. V. Manukyan, "Solution Combustion Synthesis of Nanoscale Materials", Chemical Reviews **116**, 14493–14586 (2016).

[17] B. C. Tappan, S. A. Steiner Iii, E. P. Luther, B. C. Tappan, S. A. S. Iii, and E. P. Luther, "Nanoporous Metal Foams", Angewandte Chemie International Edition **49**, 4544–4565 (2010).

[18] P. Caravan, J. J. Ellison, T. J. McMurry, and R. B. Lauffer, "Gadolinium(III) chelates as MRI contrast agents: Structure, dynamics, and applications", Chemical Reviews **99**, 2293–2352 (1999).

[19] G. D. Stasio, P. Casalbore, R. Pallini, B. Gilbert, F. Sanità, M. T. Ciotti, G. Rosi, A. Festinesi, L. M. Larocca, A. Rinelli, D. Perret, D. W. Mogk, P. Perfetti, M. P. Mehta, and D. Mercanti, "Gadolinium in human glioblastoma cells for gadolinium neutron capture therapy", Cancer Research **61**, 4272–4277 (2001).

[20] E. H. Uguru, S. F. Sani, M. U. Khandaker, M. H. Rabir, and J. A. Karim, "A comparative study on the impact of Gd2O3 burnable neutron absorber in UO2 and (U, Th)O2 fuels", Nuclear Engineering and Technology **52**, 1099–1109 (2020).

[21] M. Zinkevich, "Thermodynamics of rare earth sesquioxides", Progress in Materials Science **52**, 597–647 (2007).

[22] S. Chaudhary, S. Kumar, S. Kumar, G. R. Chaudhary, S. K. Mehta, and A. Umar, "Ethylene glycol functionalized gadolinium oxide nanoparticles as a potential electrochemical sensing platform for hydrazine and p-nitrophenol", Coatings **9**, 633 (2019).

[23] M. M. Abdullah, M. M. Rahman, H. Bouzid, M. Faisal, S. B. Khan, S. A. Al-Sayari, and A. A. Ismail, "Sensitive and fast response ethanol chemical sensor based on as-grown Gd2O3 nanostructures", Journal of Rare Earths **33**, 214–220 (2015).

[24] M. Shi, Y. Yan, Y. Wei, Y. Zou, Q. Deng, J. Wang, R. Yang, Y. Xu, and T. Han, "Fabrication of ultrafine Gd2O3 nanoparticles/carbon aerogel composite as immobilization host for cathode for lithium-sulfur batteries", International Journal of Energy Research **43**, 7614–7626 (2019).

[25] A. Zheng, R. Liang, H. Wu, G. Jiang, M. Fan, J. Xiong, and S. Yuan, "Preparation and Electrochemical Properties of Gadolinium Oxide-doped Carbon Aerogels/Sulfur Composites", Int. J. Electrochem. Sci **17**, 2 (2022).

[26] C. Xu, Y. Chen, W. Zhang, G. Hu, and R. Liu, "Layered Nanoporous α-Gd2O3Prepared by a Gd-Organic Framework Template for U(VI) Adsorption", ACS Applied Nano Materials **4**, 1104–1111 (2021).

[27] Y. W. He, Q. Wang, X. Yan, L. Q. He, G. Q. Zhang, and X. L. Li, "Ultrafast degradation of common organic dyes in presence of gadolinium oxide/graphene oxide in water", Fullerenes Nanotubes and Carbon Nanostructures **27**, 478–481 (2019).

[28] S. Lee, L. P. Lingamdinne, J. K. Yang, Y. Y. Chang, and J. R. Koduru, "Potential electromagnetic column treatment of heavy metal contaminated water using porous Gd2O3-doped graphene oxide nanocomposite: Characterization and surface interaction mechanisms", Journal of Water Process Engineering **41**, 102083 (2021).

[29] R. K. Tamrakar, D. P. Bisen, and N. Brahme, " Comparison of photoluminescence properties of Gd 2 O 3 phosphor synthesized by combustion and solid state reaction method ", Journal of Radiation Research and Applied Sciences **7**, 550–559 (2014).

[30] V. V. Bakovets, L. N. Trushnikova, P. E. Plyusnin, I. V. Korolkov, I. P. Dolgovesova, T. D. Pivovarova, and S. A. Savintseva, "Features of the sol-gel process of formation of nanostructured gadolinium oxide", Russian Journal of General Chemistry **83**, 1808–1814 (2013).

[31] S. I. Niftaliev, I. V. Kuznetsova, I. A. Saranov, T. V. Zhundrikova, L. V. Lygina, V. Y. Tuneekov, I. V. Chislova, and I. A. Zvereva, "Synthesis of Nanosized Gadolinium Oxide", Glass Physics and Chemistry **45**, 232–237 (2019).

[32] S. Hazarika and D. Mohanta, "Oriented attachment (OA) mediated characteristic growth of Gd2O3 nanorods from nanoparticle seeds", Journal of Rare Earths **34**, 158–165 (2016).

[33] J. G. Kang, B. K. Min, and Y. Sohn, "Synthesis and characterization of Gd(OH)3 and Gd2O3 nanorods", Ceramics International **41**, 1243–1248 (2015).

[34] K. Dědková, Kuzníková, L. Pavelek, K. Matějová, J. Kupková, K. Č. Barabaszová, R. Váňa, J. Burda, J. Vlček, D. Cvejn, and J. Kukutschová, "Daylight induced antibacterial activity of gadolinium oxide, samarium oxide and erbium oxide nanoparticles and their aquatic toxicity", Materials Chemistry and Physics **197**, 226–235 (2017).

[35] G. Huszka and M. A. Gijs, "Super-resolution optical imaging: A comparison", Micro and Nano Engineering **2**, 7–28 (2019).

[36] A. L. Robinson, "Electron microscope inventors share nobel physics prize", Science **234**, 821–822 (1986).

[37] B. Fultz and J. Howe, *Transmission Electron Microscopy and Diffractometry of Materials*, 4th ed. (Springer Berlin Heidelberg, 2013).

[38] D. B. Williams and C. B. Carter, *Transmission electron microscopy : a textbook for materials science*, 2nd ed. (Springer New York, NY, 2009).

[39] L. A. Rodríguez, C. Magén, E. Snoeck, C. Gatel, L. Marín, L. Serrano-Ramón, J. L. Prieto, M. Muñoz, P. A. Algarabel, L. Morellon, J. M. De Teresa, and M. R. Ibarra, "Quantitative in situ magnetization reversal studies in Lorentz microscopy and electron holography", Ultramicroscopy **134**, 144–154 (2013).

[40] M. L. Taheri, E. A. Stach, I. Arslan, P. A. Crozier, B. C. Kabius, T. LaGrange, A. M. Minor, S. Takeda, M. Tanase, J. B. Wagner, and R. Sharma, "Current status and future directions for in situ transmission electron microscopy", Ultramicroscopy **170**, 86–95 (2016).

[41] DENSsolutions, *Wildfire Nano-Chip*.

[42] S. Vijayan, R. Wang, Z. Kong, and J. R. Jinschek, "Quantification of extreme thermal gradients during in situ transmission electron microscope heating experiments", Microscopy Research and Technique **85**, 1527–1537 (2022).

[43] M. Radermacher, "Weighted back-projection methods", in *Electron tomography: methods for three-dimensional visualization of structures in the cell*, edited by J. Frank (Springer New York, 2006), pp. 245–273.

[44] P. Gilbert, "Iterative Methods for the Three-dimensional Reconstruction of an Object from Projections", J. theor. Biol **36**, 105–117 (1972).

[45] M. Thommes, K. Kaneko, A. V. Neimark, J. P. Olivier, F. Rodriguez-Reinoso, J. Rouquerol, and K. S. Sing, "Physisorption of gases, with special reference to the evaluation of surface area and pore size distribution (IUPAC Technical Report)", Pure and Applied Chemistry **87**, 1051–1069 (2015).

[46] S. Brunauer, P. H. Emmett, and E. Teller, "Adsorption of Gases in Multimolecular Layers", Journal of the American Chemical Society **60**, 309–319 (1938).

[47] J. H. De Boer, B. C. Lippens, B. G. Linsen, J. C. P. Broekhoff, A. Van Den Heuvel, and T. J. Osinga, "Thet-curve of multimolecular N2-adsorption", Journal of Colloid and Interface Science **21**, 405–414 (1966).

[48] E. P. Barrett, L. G. Joyner, and P. P. Halenda, "The Determination of Pore Volume and Area Distributions in Porous Substances. I. Computations from Nitrogen Isotherms", Journal of the American Chemical Society **73**, 373–380 (1951).

[49] K. Momma and F. Izumi, "Vesta 3 for three-dimensional visualization of crystal, volumetric and morphology data", Journal of applied crystallography **44**, 1272–1276 (2011).

[50] M. Klinger, *CrysTBox - Crystallographic Toolbox* (Institute of Physics of the Czech Academy of Sciences, Prague, 2015).

[51] P. Gopal, N. A. Spaldin, and U. V. Waghmare, "First-principles study of wurtzite-structure MnO", Physical Review B **70**, 205104 (2004).

[52] K. M. Nam, Y. I. Kim, Y. Jo, S. M. Lee, B. G. Kim, R. Choi, S. I. Choi, H. Song, and J. T. Park, "New crystal structure: Synthesis and characterization of hexagonal wurtzite MnO", Journal of the American Chemical Society **134**, 8392–8395 (2012).

[53] R. A. Robie, B. S. Hemingway, and J. Fisher, "Thermodynamic properties of minerals and related substances at 298.15 K and 1 bar (10^5 pascals) pressure and at higher temperatures", U.S. Geol. Surv. Bull. **1452**, `10.3133/B2131` (1978).

[54] C. A. Barrett and E. B. Evans, "Solid solubility and lattice parameter of Ni O - Mn O", Journal of the American Ceramic Society **47**, 533–533 (1964).

[55] D. Jarosch, "Crystal structure refinement and reflectance measurements of hausmannite, Mn3O4", Mineralogy and Petrology 1987 37:1 **37**, 15–23 (1987).

[56] K. A. Lozovoy, A. G. Korotaev, A. P. Kokhanenko, V. V. Dirko, and A. V. Voitsekhovskii, "Kinetics of epitaxial formation of nanostructures by frank-van der merwe, volmer-weber and stranski-krastanow growth modes", Surface and Coatings Technology **384**, 125289 (2020).

[57] M. A. Mohamed and S. A. Halawy, "Kinetic and mechanistic study of the non-isothermal decomposition of manganese(II) acetate tetrahydrate", Thermochimica Acta **242**, 173–186 (1994).

[58] X. San, B. Zhang, J. Wang, B. Wu, and X. Ma, "In situ tracking the reversible spinel-rocksalt structural transformation between Mn3O4 and MnO", Micron **92**, 13–18 (2017).

[59] Y. Kwon, B. S. An, J. Y. Moon, J. H. Lee, H. Yoo, D. Whang, and C. W. Yang, "Control of oxidation behavior in high vacuum transmission electron microscopy", Materials Characterization **172**, 110870 (2021).

[60] J. Wang, H. Yang, L. Kang, Z. H. Liu, G. Zhang, L. Ren, and J. Xu, "Salt-template assisted preparation and electrochemical performance of MnO/C nanosheet composite electrode for lithium-ion battery", Journal of Solid State Chemistry **264**, 134–140 (2018).

[61] X. Xiao, P. Urbankowski, K. Hantanasirisakul, Y. Yang, S. Sasaki, L. Yang, C. Chen, H. Wang, L. Miao, S. H. Tolbert, S. J. Billinge, H. D. Abruña, S. J. May, and Y. Gogotsi, "Scalable Synthesis of Ultrathin Mn3N2 Exhibiting Room-Temperature Antiferromagnetism", Advanced Functional Materials **29**, 1809001 (2019).

[62] A. G. Merzhanov and A. S. Rogachev, "Structural macrokinetics of shs processes", Pure and Applied Chemistry **64**, 941–953 (1992).

[63] Y. Kitamura, N. Okinaka, T. Shibayama, O. O. P. Mahaney, D. Kusano, B. Ohtani, and T. Akiyama, "Combustion synthesis of TiO2 nanoparticles as photocatalyst", Powder Technology **176**, 93–98 (2007).

[64] A. S. Mukasyan, P. Epstein, and P. Dinka, "Solution combustion synthesis of nanomaterials", Proceedings of the Combustion Institute **31**, 1789–1795 (2007).

[65] T. Fukuda, Y. Nakano, and K. Takeshita, "Non-isothermal kinetics of the thermal decomposition of gadolinium nitrate", Journal of Nuclear Science and Technology **55**, 1193–1197 (2018).

[66] S. Brunauer, P. H. Emmett, and E. Teller, "Adsorption of Gases in Multimolecular Layers", Journal of the American Chemical Society **60**, 309–319 (1938).

[67] E. P. Barrett, L. G. Joyner, and P. P. Halenda, "The Determination of Pore Volume and Area Distributions in Porous Substances. I. Computations from Nitrogen Isotherms", Journal of the American Chemical Society **73**, 373–380 (1951).

[68] W. Wen and J. M. Wu, "Nanomaterials via solution combustion synthesis: a step nearer to controllability", RSC Advances **4**, 58090–58100 (2014).

[69] W. Kang, D. O. Ozgur, and A. Varma, "Solution Combustion Synthesis of High Surface Area CeO2 Nanopowders for Catalytic Applications: Reaction Mechanism and Properties", ACS Applied Nano Materials **1**, 675–685 (2018).

[70] H. Ahmadian, F. A. Hessari, and A. M. Arabi, "Preparation and characterization of Luminescent nanostructured Gd2O3-Y2O3:Eu synthesized by the solution combustion process", Ceramics International **45**, 18778–18787 (2019).

[71] S. Patil and H. P. Dasari, "Effect of fuel and solvent on soot oxidation activity of ceria nanoparticles synthesized by solution combustion method", Materials Science for Energy Technologies **2**, 485–489 (2019).

[72] Q. Chen, Y. Shi, J. Chen, and J. Shi, "Photoluminescence of Lu2O3:Eu3+ phosphors obtained by glycine-nitrate combustion synthesis", Journal of Materials Research 2005 20:6 **20**, 1409–1414 (2005).

[73] W. Haynes, D. Lide, and T. Bruno, *CRC Handbook of Chemistry and Physics*, 95th (CRC Press: Boca Raton, FL, USA, 2014), pp. 4–64.

A. Supplementary Figures for Manganese Oxide Nanosheets

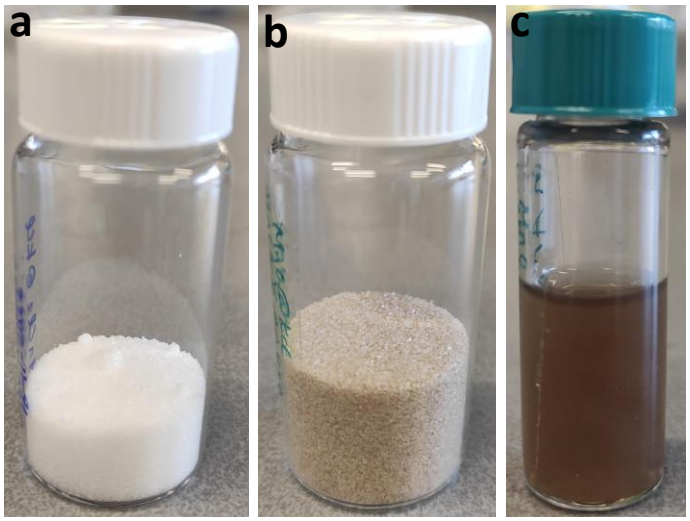

Figure A.1: Photographs of (a) unheated Mn coated salt, (b) Mn coated salt after heating, and (c) dispersion of MnO_x nanoparticle arrays after removal of the KCl templates.

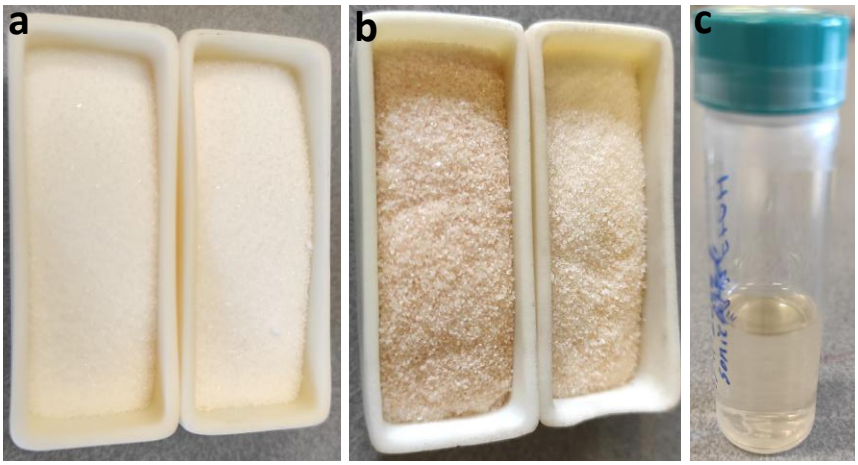

Figure A.2: Photographs of (a) unheated Mn coated salt, (b) Mn coated salt after heating, and (c) dispersion of MnO nanosheets after removal of the KCl templates.

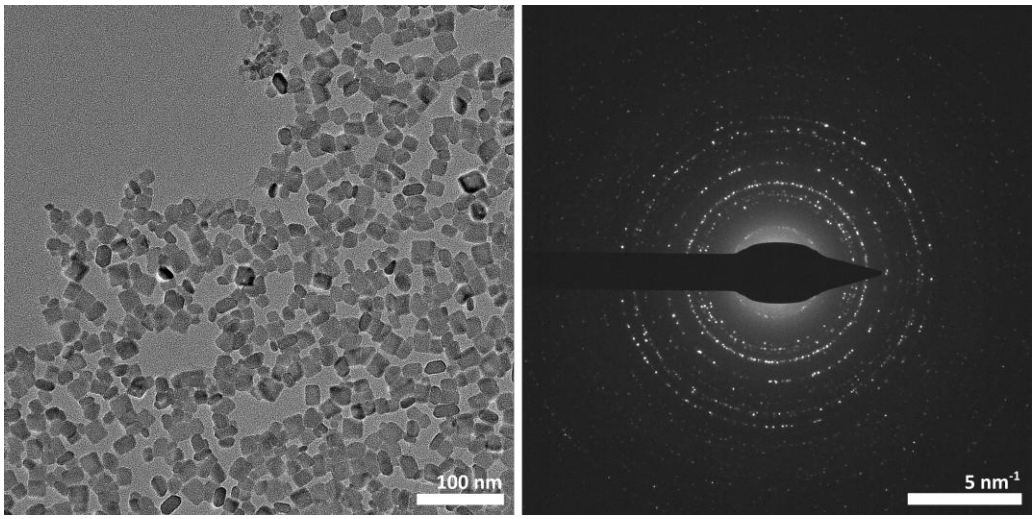

Figure A.3: First synthesis under N_2 atmosphere resulting in Mn_3O_4 particles.

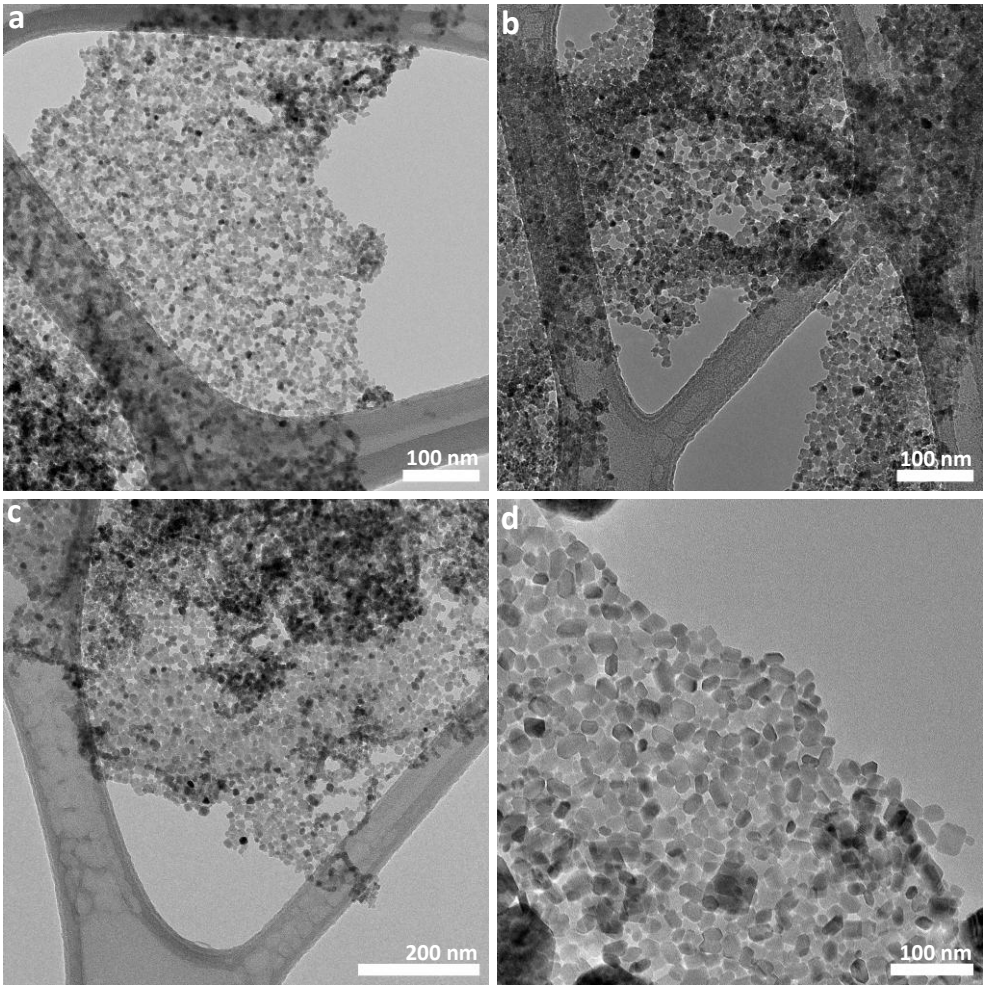

Figure A.4: Particles obtained by (a) heating at 300 °C, (b) heating at 350 °C, (c) using a ramping rate of 10 °C/min, and (d) using 500 mg $MnAc_2$.

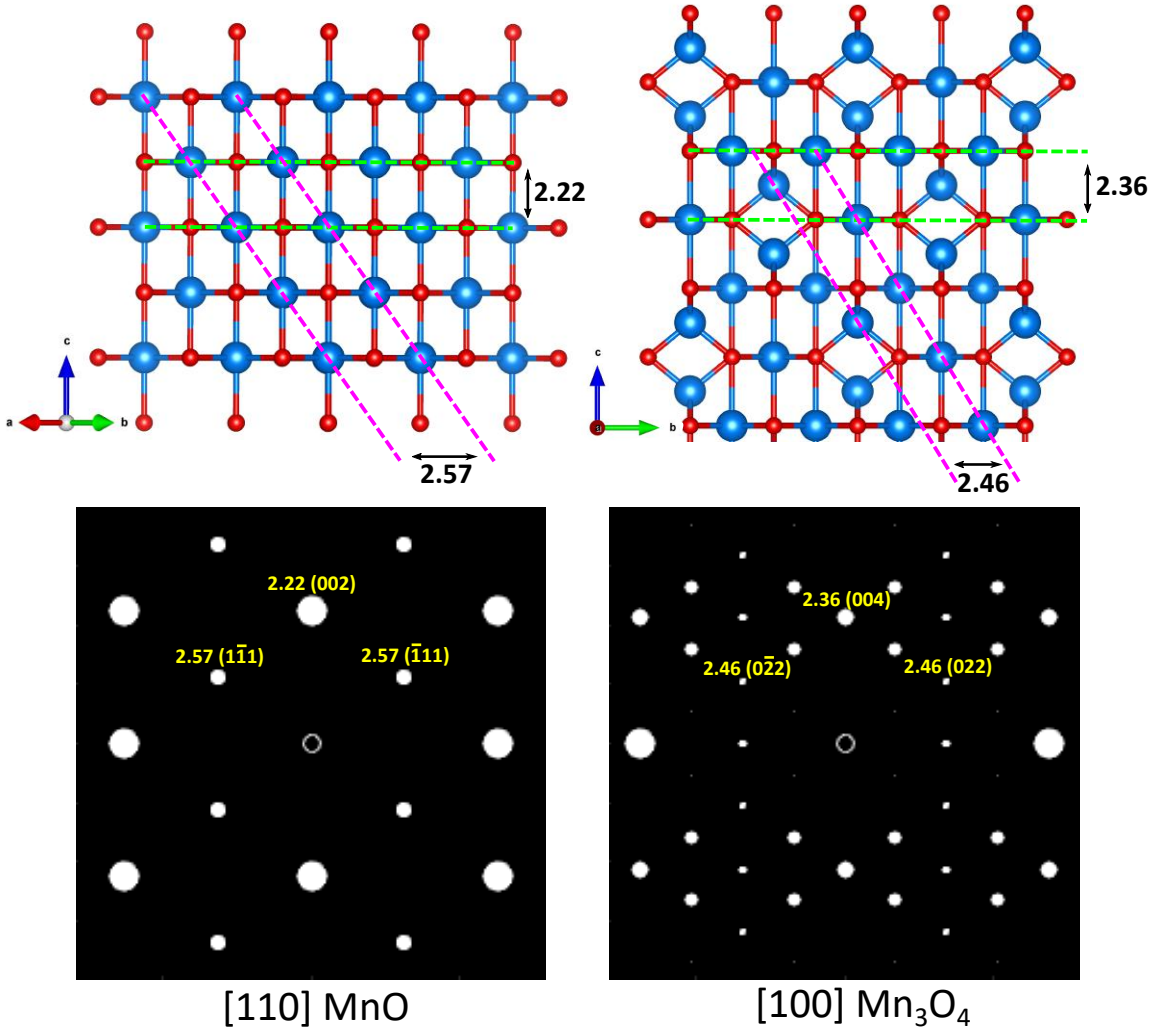

Figure A.5: Atomic configurations and theoretical diffraction patterns of the [110] MnO and [100] Mn_3O_4 planes. All d-spacings are in units of Ångström.

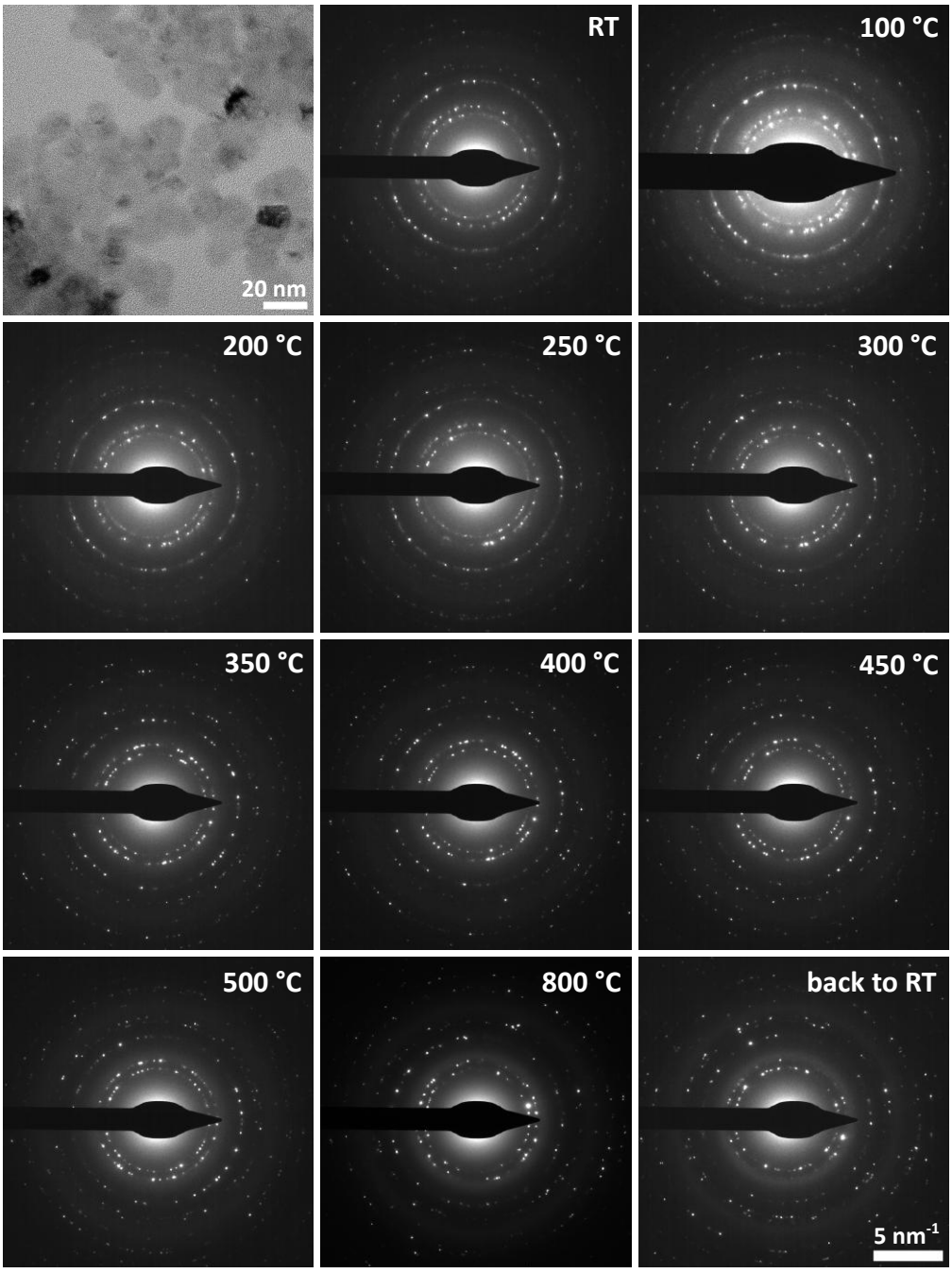

Figure A.6: TEM image of followed area 1 at room-temperature (a) and diffraction patterns at each temperature during the heating of the MnO_x nanoparticles. The scalebar is the same for all diffraction patterns.

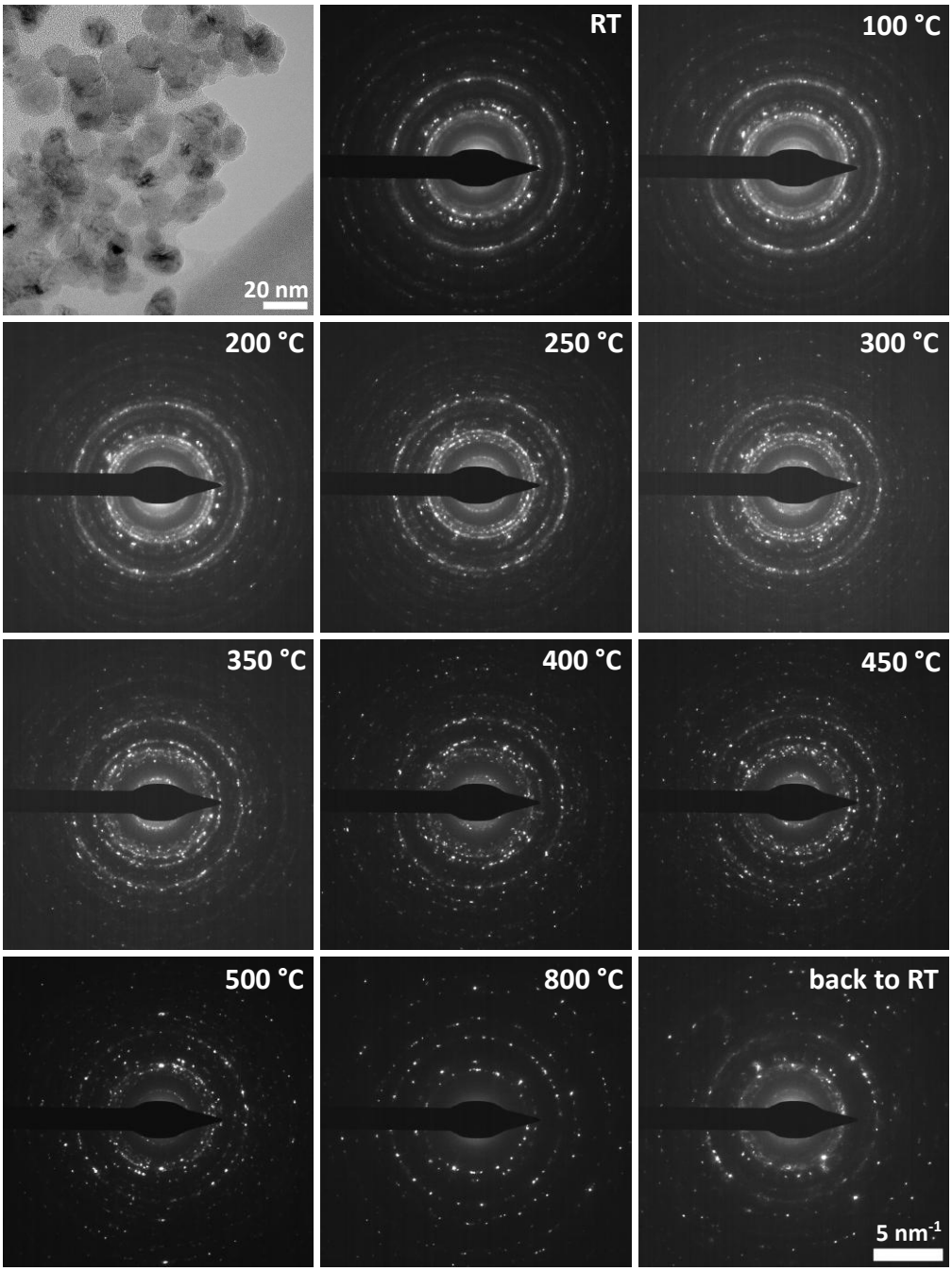

Figure A.7: TEM image of followed area 2 at room-temperature (a) and diffraction patterns at each temperature during the heating of the MnO_x nanoparticles. The scalebar is the same for all diffraction patterns.

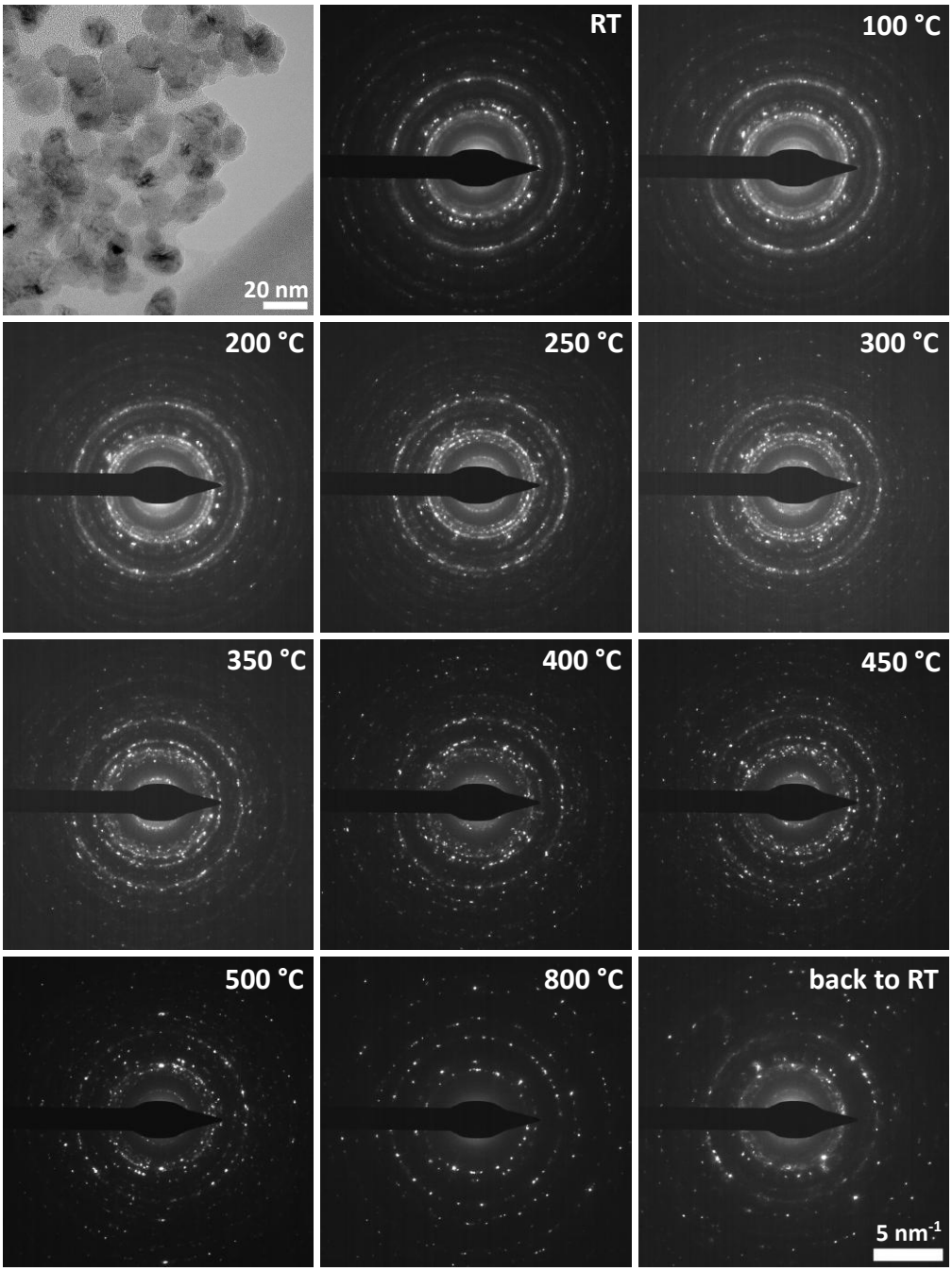

Figure A.8: TEM image of followed area 3 at room-temperature (a) and diffraction patterns at each temperature during the heating of the MnO_x nanoparticles. The scalebar is the same for all diffraction patterns.

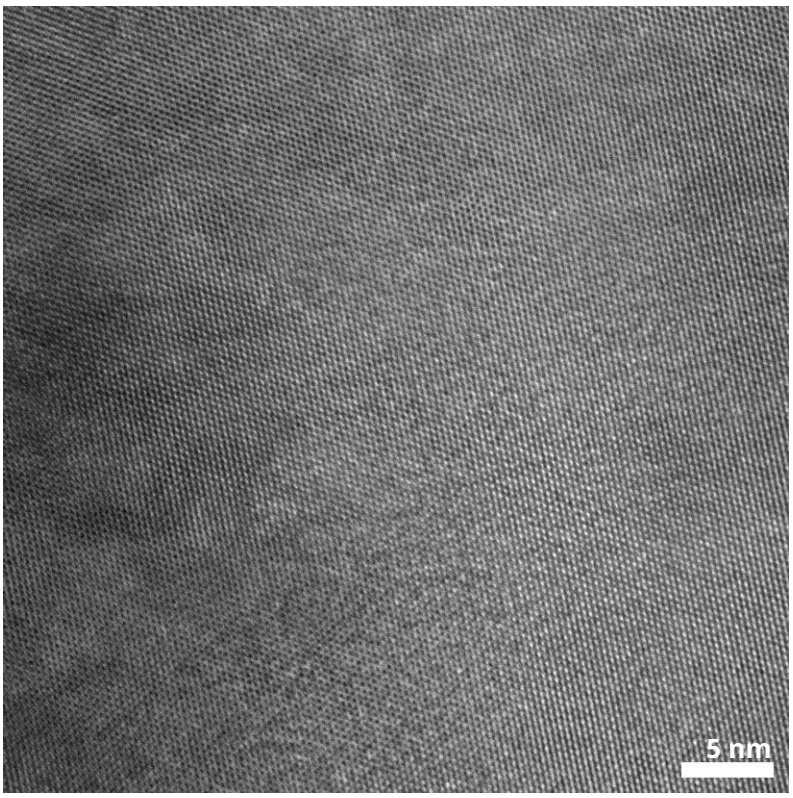

Figure A.9: Full HRTEM image of t-MnO nanosheet.

B. Supplementary Figures for Gadolinium Oxide Nanocrystals

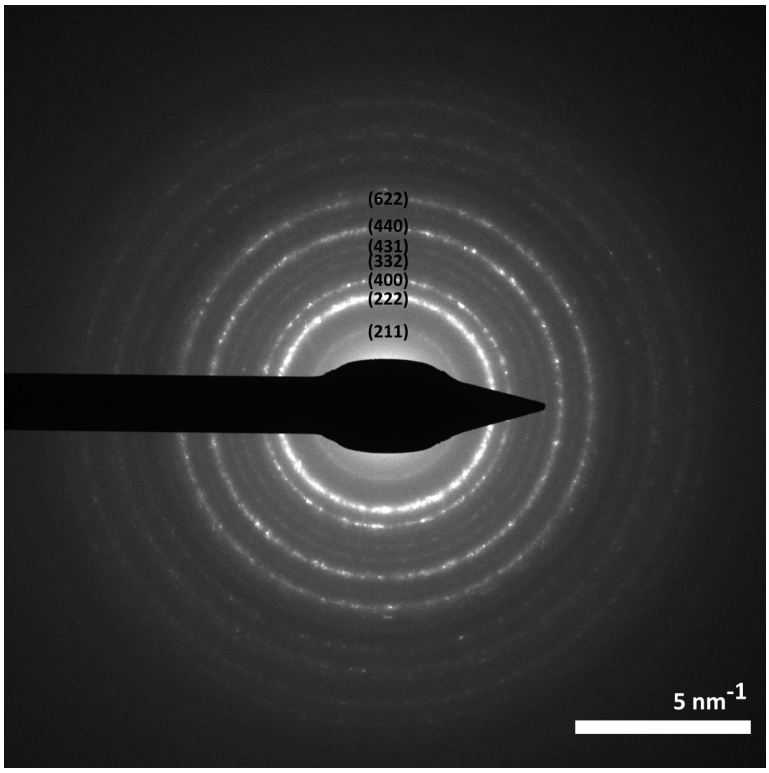

Figure B.1: Indexed electron diffraction pattern indicating the cubic Gd_2O_3 phase.

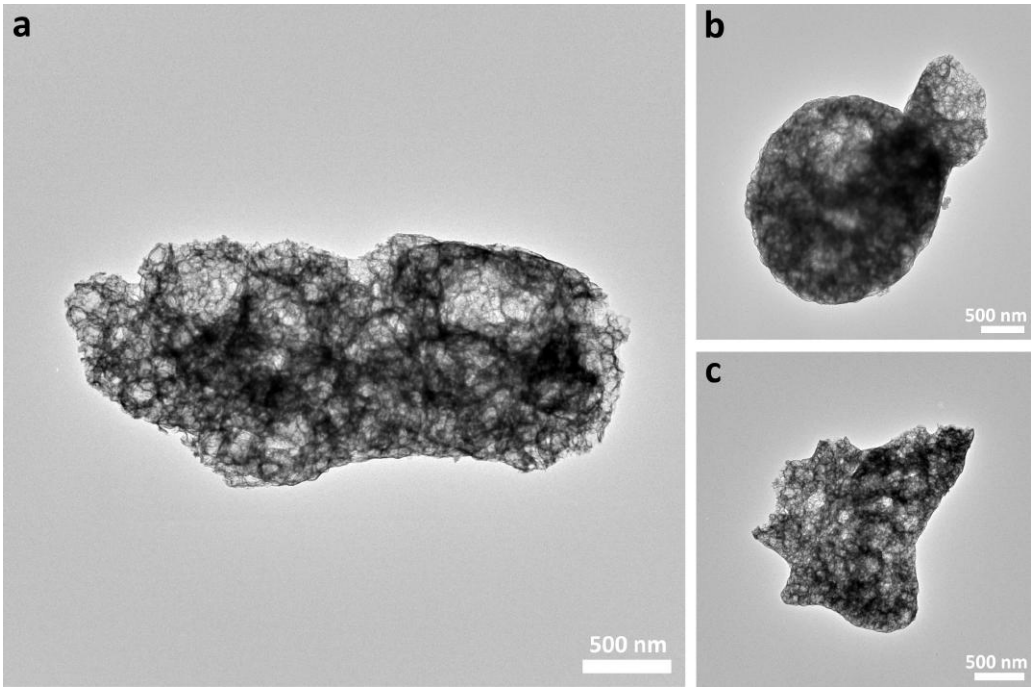

Figure B.2: TEM images of different Gd_2O_3 morphologies showing a cylindrical (a), spherical (b), and irregular structure (c).

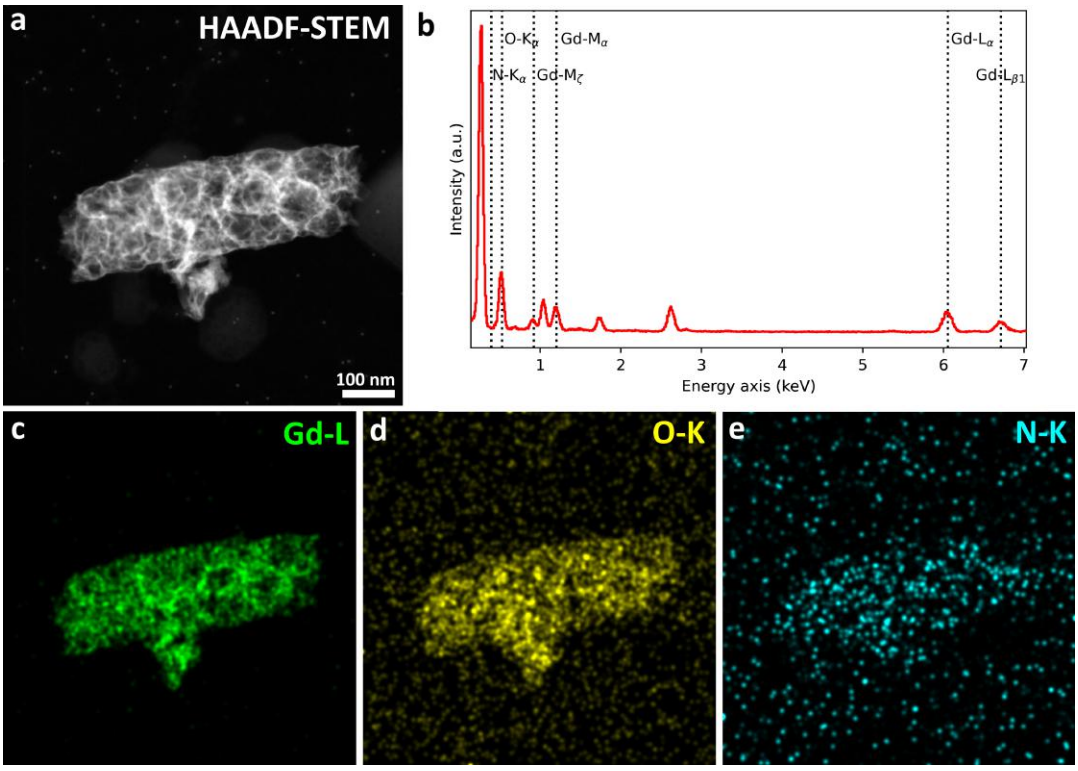

Figure B.3: EDS analysis of the Gd_2O_3 grain shown in the HAADF-STEM image (a). The EDS spectrum in (b) shows peaks corresponding to the elements Gd and O, and the absence of a N peak. Elemental maps shown in (c) and (d) indicate that Gd and O are uniformly presented throughout the particle, whereas (e) shows that the presence of N is negligible.

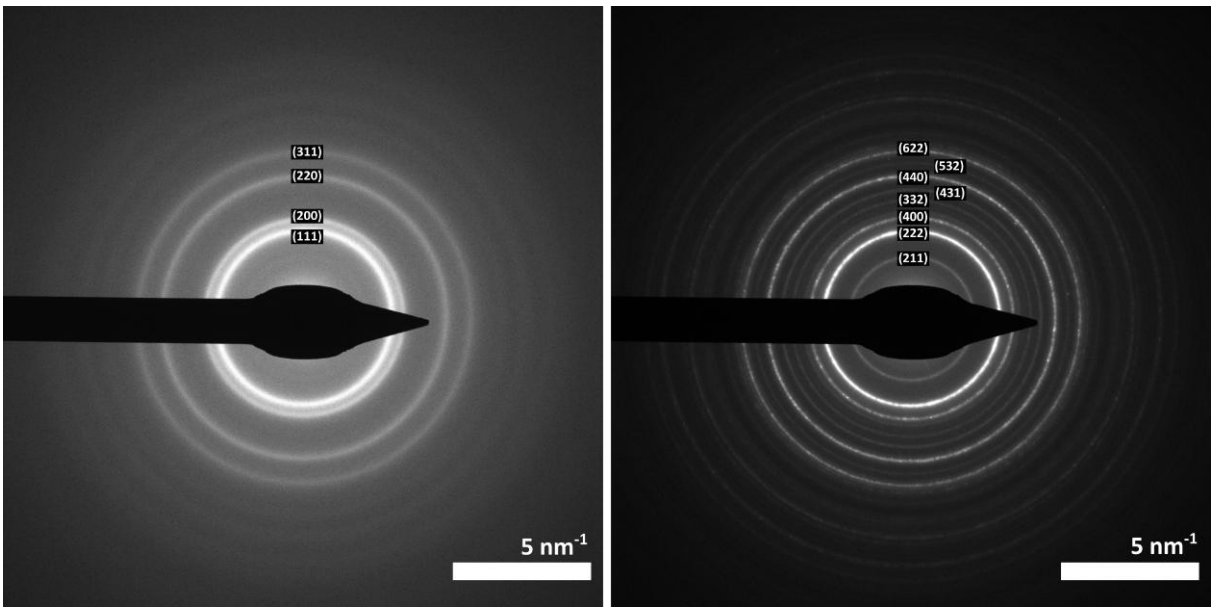

Figure B.4: Indexed diffraction patterns of the *in-situ* heating to 600 °C corresponding to GdO (left) and the ex-situ heating to 900 °C corresponding to Gd_2O_3 (right).

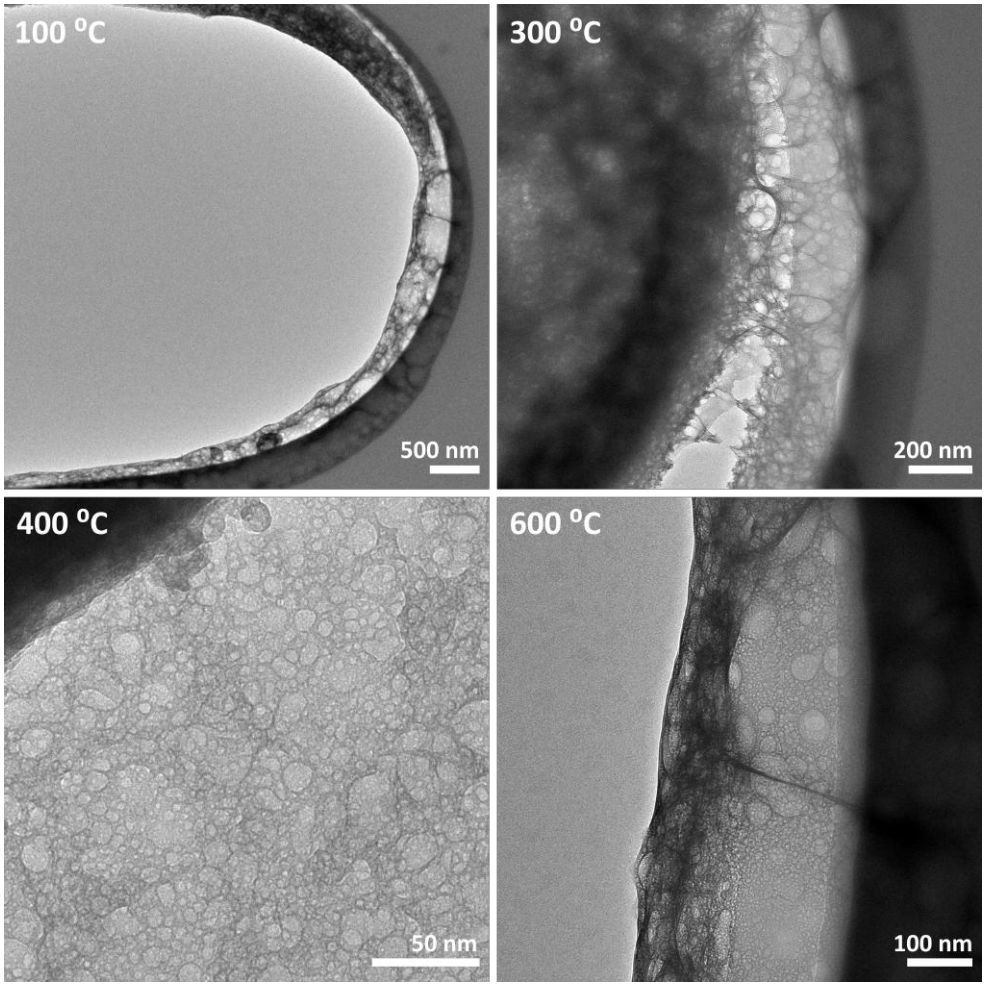

Figure B.5: TEM images of Gd gel during *in-situ* heating to 600 °C.

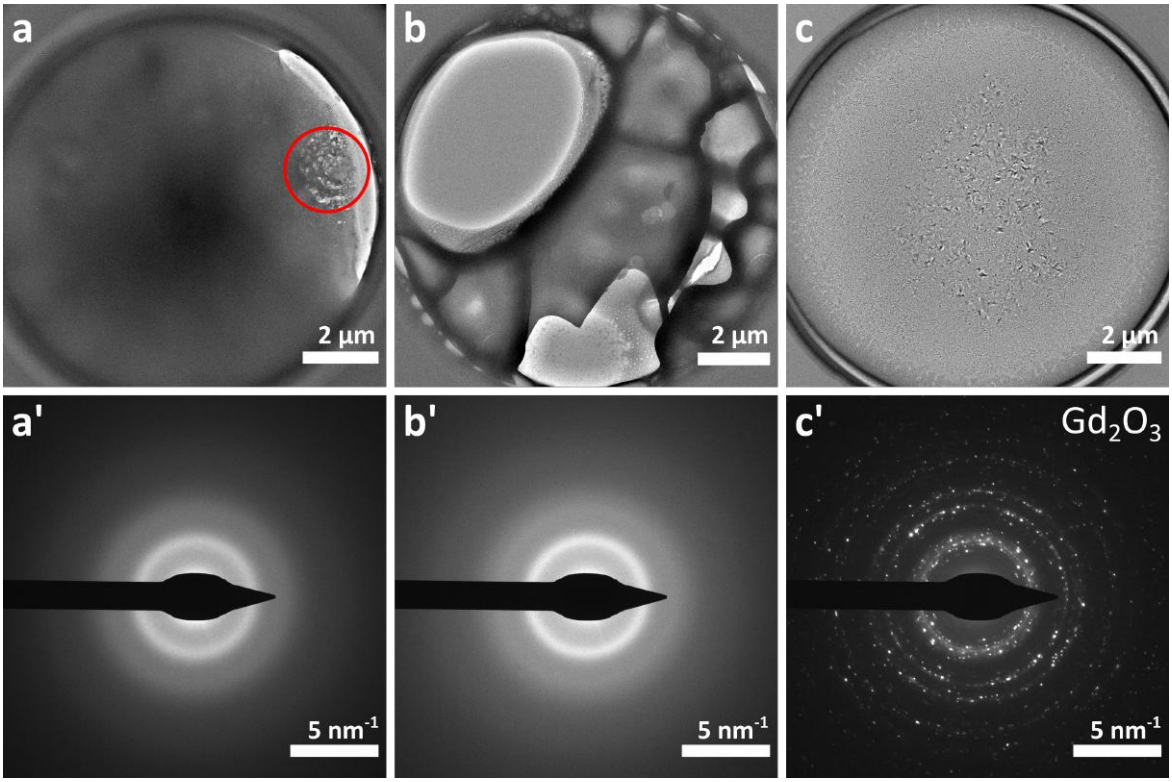

Figure B.6: TEM window overview image of 600 °C *in-situ* sample after 6 weeks (a), 600 °C ex-situ sample after 6 weeks (b), and 900 °C *ex-situ* sample after 7 weeks (c) with corresponding diffraction patterns (’). The red circle indicates the area that abruptly changed when illuminated with the electron beam.

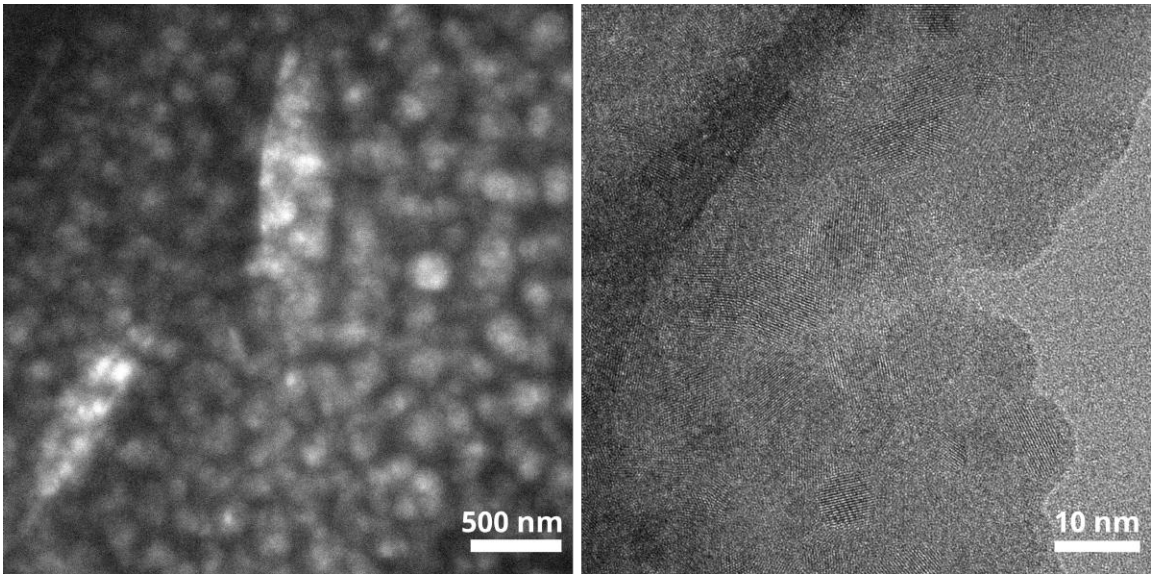

Figure B.7: TEM image of the precursor heated to 100 °C showing large scale porosity (left) and HRTEM image of the precursor heated to 900 °C, which is not showing small scale porosity (right).

Acknowledgements

First of all, I would like to thank my supervisors Marijn and Rafael for making this project possible. Marijn, thank you for involving me in your group and for giving me the freedom to explore my own research project. Your feedback and support have been really valuable, and our meetings have always boosted my motivation. Rafael, thank you for your guidance, for always being available, and for the many microscopy hours we spent together. I admire your enthusiasm for science, and our conversations have sparked my curiosity for 2D materials and their mysteries. I truly hope you will obtain your ERC grant and can pursue your own research interests in academia. Because of both of you, I have enjoyed working on this thesis for the past year.

I would also like to thank all the other people that were involved in this journey. Katerina, thank you for initiating our collaboration on the gadolinium oxide and for visiting us all the way from Czech Republic. It was nice to be able to discuss our research in person and to see the synthesis. Heleen, thank you for starting the DFT calculations on the MnO nanosheets. I am sure that your calculations will complement the experimental results nicely. Thanks Xiaodan for your help with the *in-situ* experiments and for being available even though you were not my supervisor. Thanks Albert for your help with the first synthesis and finding my way around the labs. I would also like to thank the staff of the electron microscopy center, Ali, Chris, and Hans. Ali, thank you for your help with the Spectra, for the training on the baby Talos, and our discussions. Chris, thank you for the training on the Tecnai and Phenom microscopes. I would also like to thank Relinde for the help around the labs, for ordering chemicals and TEM grids, and for brainstorming ways to make a controlled oxygen environment which we sadly could not use after all. Stephan and Peter from CMI are thanked for granting me access to the tube ovens and for providing me with heating boats. Tim Prins is thanked for making it possible to use the Ar tube oven at the ARC-CBBC facility, and Remco Dalebout is thanked for the physisorption measurement on the "fluffy" gadolinium oxide.

Finally, I would like to thank Jesse for listening to my many worries and helping me overcome challenges, for helping me find my way around Ornstein, and for discussing and proofreading this work. I couldn't have done it without you.

List of Publications and Presentations

Publications based on this thesis:

- R.M. de Boer, M.A. van Huis, R.G. Mendes, 'Reversible MnO to Mn_3O_4 Oxidation in Manganese Oxide Nanoparticles'. *In preparation* (Section 3.2)
- R.M. de Boer, H. van Gog, R.G. Mendes, M.A. van Huis, 'Square to Trigonal Lattice Transformation Observed in MnO Thin Films'. *In preparation* (Section 3.3)
- R.M. de Boer, X. Chen, D. Cvejn, K. Peterek Dědková, M.A. van Huis, R.G. Mendes, 'Nanoscale Porosity of High Surface Area Gadolinium Oxide Nanofoam Obtained with Combustion Synthesis', Advanced Materials Interfaces. *Submitted* (Section 4)

Other publications by the author:

- X. Chen, R.M. de Boer, A. Kosari, H. van Gog, M.A. van Huis, 'Heating-Induced Exfoliation and Thermal Reduction of MoO_3 Particles Monitored by In-Situ Transmission Electron Microscopy', Applied Surface Science, Preprint available at SSRN: `https://ssrn.com/abstract=4175997`. *Submitted*

Presentations based on this thesis:

- R.M. de Boer, X. Chen, D. Cvejn, K. Peterek Dědková, M.A. van Huis, R.G. Mendes, 'Nanoscale Porosity of High Surface Area Gadolinium Oxide Nanofoam Obtained with Combustion Synthesis', SCMB poster session, Utrecht University (2022), Utrecht (poster)